THEORETICAL STUDY OF THE MOLECULAR PROCESSES OCCURRING DURING THE GROWTH OF SILICON ON Si(100) AND Si_XGe_{1-X}/Si(100)

LIM CHIANG HUAY, FREDA

NATIONAL UNIVERSITY OF SINGAPORE

2007

THEORETICAL STUDY OF THE MOLECULAR PROCESSES OCCURRING DURING THE GROWTH OF SILICON ON Si(100) AND Si_XGe_{1-X}/Si(100)

LIM CHIANG HUAY, FREDA
(B.Sc. (Hons.) NUS)

A THESIS SUBMITTED FOR THE DEGREE OF DOCTOR OF PHILOSOPHY

DEPARTMENT OF CHEMISTRY

NATIONAL UNIVERSITY OF SINGAPORE

2007

Acknowledgement

I would like to acknowledge and extend my heartfelt gratitude to the following persons and organizations that have made the completion of this thesis possible:

My supervisor and co-supervisor, Assoc. Prof. Kang Hway Chuan and Assoc. Prof. Tok Eng Soon, for their mentorship and time taken to vet through, reprove and approve my thesis.

The Department of Chemistry, NUS, as well as Chartered Semiconductor Manufacturing Ltd., Singapore, for the scholarship and scholarship top-up provided during the course of this work.

My research group mates, Sheau Wei, Shi Jing, Li Qiang and Sofian for their time in discussion and their advice.

My friend, Serene, for the precious time taken to proof read my thesis.

My parents, Mabel and Jack, and auntie Sandy, for their emotional and moral support during the course of this work.

My sibling, Tian Xiang and Vera, for helping me to check through the references made in this work and helping with the printing logistics.

My Husband and family, Chin Ming and Mr. and Mrs. Chong, for their patience and understanding during the times that I needed to focus on the writing of my thesis.

And to the Almighty God, who made all things possible.

Table of Contents

Summary

This thesis summarizes some of the work done in an attempt to elucidate the mechanisms of several surface processes. The focus of this work was on the processes occurring on the surface of pure, strained silicon(100)-2×1 as well as silicon-germanium during the growth of silicon by gas-source molecular beam epitaxy (GSMBE). First-principles calculations were mainly used in this work. The surface processes of interest include the initial decomposition process of the silyl species arising from silane and disilane and the surface diffusion process of the decomposition. An attempt was made to address several puzzles pertaining to the growth of silicon by GSMBE using silane and disilane as precursors.

Our results on the energetics of various species are consistent with those that had been reported in the literature, and we added on to the understanding of this topic by providing justification using kinetics. We had also trace out the path by which these species take on the surfaces of the above mentioned substrate.

List of Tables

List of Figures

1 Introduction

It is the aim of this work to study the atomic-scale processes occurring on the surface of a semiconductor during the molecular beam epitaxial growth of the material. The focus of this work is on the molecular beam epitaxy of silicon using precursors such as silane and disilane on substrates such as silicon(100), germanium-doped silicon and strained silicon.

1.1 Motivation & Research Objectives

Table 1.1: A summary of the Semiconductor Industry Association (SIA) National Technology Roadmap for Semiconductor (NTRS; Adapted from ITRS 2005 update, Overall roadmap technology characteristic.

Year of production From 2005 - 2013	**'05**	**'06**	**'07**	**'08**	**'09**	**'10**	**'11**	**'12**	**'13**
Technology Node (nm)			65			45			32
DRAM ½ Pitch (nm)	80	70	65	57	50	45	40	36	32
MPU physical gate length (nm)	32	28	25	23	20	18	16	14	13

The Semiconductor Industry Association (SIA) roadmap summary shown in Table 1.1 above is a collective view on the future of the microelectronic industry which facilitates the continuation of the evolution of the semiconductor industry along the famous Moore's Law [1]. While the Moore's law is a "linear extrapolation" of industrial trends, the roadmap shows a forecast based on laboratory technology as well as some medium term predictions. Considering the rate at which the dimensions of semiconductor devices are shrinking, a detailed knowledge and understanding of the fundamental growth

processes in epitaxy is desirable, since at such scales, the effects of defects and reconstructions on the fabrication and performance of microelectronic devices will become increasingly important.

Furthermore, as the semiconductor devices continue to shrink to meet the demands of Moore's Law, atomic level interactions are bringing the anticipated performance enhancement to the limits of the material in use. The main material, silicon will eventually have to be replaced by materials such as strained silicon or silicon-germanium in-order to continue enhancing the speed of semiconductor devices. This is because it was found that by simply incorporating a strain on a semiconductor crystal, the speed at which charges travels through the crystal can be significantly altered. Putting that in perspective, straining the crystal by one percent can cause a five to twenty percent enhancement in transistor speed. [2]

In the growth of silicon and related materials using chemical vapor deposition or gas-source molecular beam epitaxy technique, the common gas-source precursors employed in the reactions are silane and disilane. The mechanisms of the pyrolysis of these precursors have been an area of intense research for many years. There have been debates about whether the kinetics of the pyrolysis is controlled by homogeneous gas phase reactions or by heterogeneous gas-surface reactions. Much of the earlier work by Purnell [3] and Walsh [4] concluded that silane thermolysis is primarily a homogeneous process. However it was due to more research progress in this area later in the 1980s that led people to the current understanding of these reactions. It is now generally accepted that surface reactions contribute significantly to the overall rate of dissociation of these

precursors. Especially at conditions of low pressure and high temperature employed during growth, surface pyrolysis of the growth precursors predominates.

The low-temperature reactivity of the silicon(100)-(2×1) surface toward silane and disilane has been attributed to the surface dangling bonds. As silane and disilane chemisorbs on the growing surface, they readily decompose upon interacting with available dangling bonds on the surface. Both precursors dissociate to first give SiH_3 and eventually other SiH_x products. It is the subsequent decomposition of the SiH_x that leads to film growth and H_2 evolution. The availability of dangling bonds on the surface is a key factor for growth. Various investigations have demonstrated that when the surface dangling bonds are passivated, with e.g. hydrogen, growth is severely retarded.

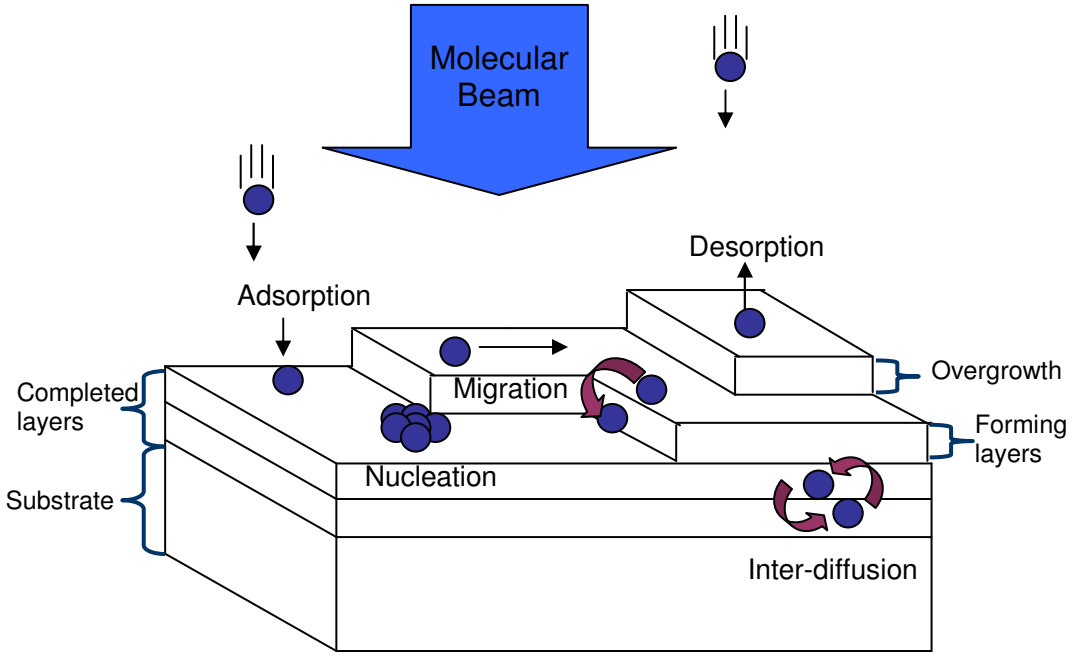

Figure 1.1: Surface processes occurring during growth. Illustrated processes include Nucleation, Migration, Inter-diffusion, Adsorption and Desorption. This figure omits details of pyrolysis reaction and contains only processes related to physical deposition.

Figure 1.1 above shows some examples of the various surface processes that are occurring during molecular beam epitaxy of thin films. They include adsorption, migration, nucleation, inter-diffusion and desorption. Various research groups all over the world have already been studying the growth processes of silicon since the late 60's. Many experimental techniques have been employed throughout the quest to understand such processes.

Table 1.2: A non exhaustive summary of the methods employed in the study of the surface processes occurring during the growth of silicon. These are listed randomly not based on preference, priority or seniority.

Methods employed	Research Groups
Electron Microscopy	United Aircraft Research Laboratories, East Hartford, Connecticut [5] (Since late 60's).
Optical microscopy	Research Institute of Electrical Communication, Tohoku University, Sendai, Japan [6]; Semiconductor Research Institute, Sendai, Japan [6].
UV photoemission spectroscopy	Bell Laboratories (since around late 70's) [7-15]; Max-Planck-Institut für Festkörperforschung (since around late 70's) [16].
Low energy electron diffraction	Bell Laboratories (since around late 70's) [7-15]; Department of Chemical Engineering, Massachusetts Institute of Technology (since around late 80's) [17; 18; 19].
Reflection high energy electron diffraction	Department of Physics and Interdisciplinary Research Center for Semiconductor Materials, Blackett Laboratory [20, 21]; Imperial College of Science, Technology and Medicine [20, 21].

Methods employed	**Research Groups**
Infrared spectroscopy	Bell Laboratories (since around late 70's) [7-15]; Research Institute of Electrical Communication, Tohoku University [22-25]; The Graduate University for Advanced Studies in collaboration with the Department of Vacuum UV Photoscience, Institute for Molecular Science [26].
Static Secondary Ion Mass Spectroscopy	Department of Chemical Engineering, Massachusetts Institute of Technology (since around late 80's) [17-19].
Temperature Programmed Desorption; Temperature Desorption Spectroscopy	Department of Chemical Engineering, Massachusetts Institute of Technology (since around late 80's) 17-19]; Department of Chemistry, University of California [28]; Department of Physics and Interdisciplinary Research Center for Semiconductor Materials, Blackett Laboratory [20, 21]; Imperial College of Science, Technology and Medicine [20, 21].

Methods employed	Research Groups
Supersonic molecular beam scattering techniques	School of Chemical Engineering, Cornell University [27-29].
Scanning Tunneling Microscopy	Department of Chemistry, University of Wisconsin [30-32]; Abteilung Oberflächenchemie und Katalyse, Universität Ulm [33-36]; Department of Materials, Oxford University [37-41]; Faculté des Sciences de Luminy, Groupe de Physique des États Condensés, Université de la Mediterranée [42].
Electron beam irradiation technique	Advanced Technology Research Center, Mitsubishi Heavy Industries [43, 44].
Semi-empirical calculation	Department of Chemistry, Oklahoma State University [45, 46].
First Principle Total Energy calculations	Philips Research Laboratories, The Netherlands [47, 48]; National Research Institute for Metals, Japan [49]; Institute of Physics, University of Tsukuba, Japan [50,51]; Centro de Ciencias de la Materia Condensada, Universidad Nacional Autonoma de Mexico [N. Takeuchi, Surf. Sci. 529, 274 (2003)].
Kinetic model calculations	Abteilung Oberflächenchemie und Katalyse, Universität Ulm [33-35, 52].

Methods employed	Research Groups
Density functional calculations	Department of Materials, Oxford University [37-41]; School of Physics, Georgia Institute of Technology [53]; Department of Chemistry and Biochemistry, University of Delaware [54, 55]; Department of Chemistry, Pennsylvania State University [56]; Department of Chemical Engineering, University of California-Santa Barbara [57-61]; Thermosciences Institute, NASA Ames Research Center [61]; Department of Chemistry, Tamkang University [62, 63]; Department of Physics, Tamkang University [63]; Department of Material Science and Engineering, Stanford University [64]; Department of Chemical Engineering, Stanford University [64]
Molecular dynamics simulation	Department of Chemistry and Physics, University of California, Santa Barbara [57, 58]; Department of Chemical Engineering, University of California-Santa Barbara [57-61]
Monte Carlo simulation	Department of Chemical Engineering, University of California-Santa Barbara [57-61]
Molecular statics simulation	Department of Chemical Engineering, University of California-Santa Barbara [57-61]

While current experimental methods, such as the atom-tracking STM, allows one to measure individual dynamic events occurring over time scales as short as 5 milliseconds, they are still not good enough for the experimental determination of the atomic pathway of SiH_3 decomposition. Five milliseconds is a lot longer than the 10^{-13} seconds timescale for typical elementary processes such as a silyl group hopping from one adsorption site to another or its molecular decomposition. Hence in order to understand the details of the motion of the atoms during growth, theoretical analysis is essential. Various theoretical groups have therefore worked on this problem using methods ranging from semi-empirical to density functional theory.

As mentioned earlier, the most common precursors for the gas source molecular beam epitaxy of silicon are silane and disilane. It has been demonstrated that the growth rate of silicon on the silicon(100) surface is enhanced when disilane is used instead of the conventional silane. This is because of the higher adsorption rates associated with the greater ease with which silicon-silicon bonds are broken compared to silicon-hydrogen bonds [42, 65y studies indicate fact that when these precursors dissociate on the substrate surface, especially at low coverage, they form the trihydride (SiH_3), and dihydride (SiH_2) before they decompose to a surface monohydride (SiH) species [17, 20, 21, 66]. Without doubt, one common species will be formed momentarily, the SiH_3 species. According to Gates *et. al.* [66], the initial decomposition of SiH_3 occurs at substrate temperature of 150-200K regardless of the coverage. Gates *et. al.* also reported that SiH_2 decomposes at a temperature of 750K. Hence SiH_2 and H will be the predominant growth species during growth. The bulk of this work is therefore dedicated to the understanding of how these

species are formed on the surface and how these species move on the surface after their formation to achieve growth.

1.2 Organization of Thesis

The motivation of this work has been briefly discussed in this section of the thesis. In the subsequent section, an overview of related work carried out by other researchers will be discussed. Chapter 3 and 4 will be dedicated to the discussion of the calculation method involved during the course of this work. In the discussion section starting from chapter 5 to chapter 7, some of the findings from this work will be reported. Firstly, the relative stabilities of the various stable configurations of SiH_2 on the surface of silicon(100) will be presented. These SiH_2 species are decomposition products of the SiH_3 species which are the most prevalent growth species on the surface during GSMBE. Next, the work that go on to elucidate the possible pathway via which the SiH_3 species decomposes will be discussed. Most of the previous theoretical investigations on this topic address only the energetics of the initial and possible final states, and only a few address the dissociation pathway of the SiH_3 group. In this work, an attempt was made to trace the reaction path and hence gain insight into the kinetics of the SiH_3 decomposition process in addition to the studies of the energetics. Finally, the surface diffusion process of the decomposition products of SiH_3 namely, SiH_2 and H, on silicon(100) will be discussed and compared to that on strained silicon to understand the impact of strain and germanium on the surface diffusion behavior.

2 An overview of the Si(100) and SiGe(100) surfaces and related studies

This section of the thesis gives a brief overview of the type of work that has been well researched and published in the study of growth on silicon and silicon-germanium surfaces. It is divided into various sub-sections including a description of the following: the clean silicon (100) and silicon-germanium (100) surfaces, the hydrogenated surface, the decomposition of silane and disilane, the decomposition of subsequent by-products and the diffusion of these by-products.

2.1 The clean silicon (100) and silicon-germanium (100) surfaces

Because the entire growth process discussed in this thesis takes place on the surface the substrate, it is important for us to have a detailed understanding of the structures of clean surfaces before we embark on the discussion of growth.

Silicon and germanium are both group IV elements with four valence electrons. They crystallize in the diamond structure with each atom bonded to four others in a tetrahedral fashion.

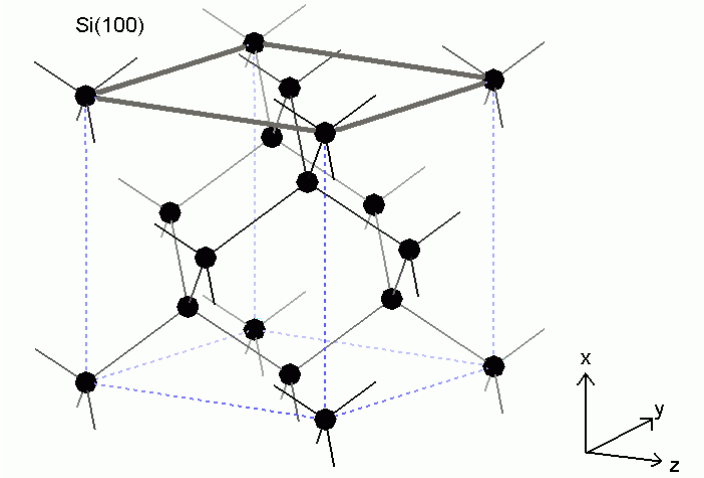

Figure 2.1: Silicon crystal structure – the diamond structure. The (100) plane is outlined in grey.

When cleaved in the (100) plane, each surface silicon atom will be left standing alone with two broken bonds. Intuitively, one would expect the resulting surface to be energetically unfavorable since so many bonds are broken. However, it is not immediately obvious which kind of reconstruction this surface would take. For over three decades, there had been much debate on the kind of reconstruction that would take place on the Si(100) surface. Various models have been proposed to answer for the 2×1 symmetry observed in LEED since 1957, e.g., the raised rows model [1], the missing rows model [2, 3], ridges model [3], and the multivacancies model. [4] It was only in 1986, with the advent of STM, that the dimer model, first proposed thirty years before, triumphed as the surface reconstruction on the Si(100) surface. [5, 6]

While the dimer model was confirmed as the surface reconstruction for the Si(100) surface, the question on the symmetry of the dimers remained unresolved until the mid 90s. Although STM images at room temperature showed symmetric dimers, surface scientists did not give up on the quest to seek the "true" state of the surface. This is because a static surface with symmetric dimers and a dynamic surface with flip-flop

buckled dimers will give rise to different type of surface processes. Finally, STM images taken by Robert Wolkow at liquid-nitrogen temperature confirmed the buckling of dimers [6] while ab-initio DFT calculations also showed that the buckled dimers were indeed energetically more stable. [7]

The buckling of the surface dimers opens up an energy gap on the metallic states present in symmetric dimers. [8, 9] This effect is similar to what is know is a Jahn Teller distortion [10]. In this case, the distortion mechanism involve the conversion of a partially occupied, degenerate state (the symmetric dimer), to that leaving the occupied state having a lower energy (the buckled "up" silicon atom) and thereby breaking the degeneracy. The total energy of the system is lowered as a result.

It is now generally accepted that the Si(100) surface consists of parallel rows of dimers. Each dimer is buckled at an angle of approximately 20^{o}. Over the years, theoretical and experimental determination of this value gives a deviation of about 5^{o}. Now, the buckled dimer is routinely obtained in most first-principles calculations. Dimers go through alternating dynamic buckling and they oscillate with a period of around 200 femtoseconds from one tilt direction to the other [11]. The reason why STM was not able to reveal this initially is because, in STM, the tip averages the different position assumed by the dimer atoms over a period of $10^{-2} – 10^{-1}$ s.

There are three types of steps on this surface, namely, the S_A steps, the non-rebonded S_B steps and the rebonded S_B steps. The S_A steps are steps where the dimer rows on the upper side are parallel to the step direction. The S_B steps are steps where the dimer rows on the upper side are perpendicular to the step direction. It is interesting to note that due to the orientation of the sp^3 orbitals on the silicon atoms, the dimer rows on

the upper side of a monolayer-high step are oriented perpendicularly to that on the lower side of the step.

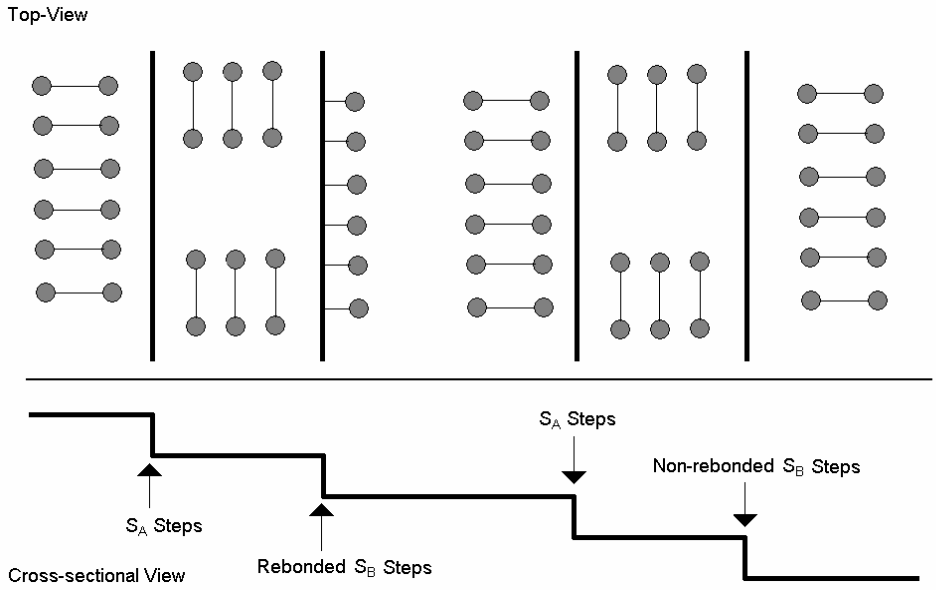

Figure 2.2: An illustration of the various steps on the silicon (100) surface

The Ge(100) surface, being very similar to the Si(100) surface, also has a dimer termination that is covalent in nature [12]. At low temperatures these surfaces show the c(2×4) reconstruction with each dimer buckled in anti-phase with its neighbor in both the dimer bond and the dimer row direction. At high temperatures, rapid thermal oscillation of the dimers cause the reconstruction to become (1×2). A high resolution photoemission study of the Ge/Si(100) surface showed that germanium grows first as mixed asymmetric silicon-germanium dimers with germanium occupying the "buckled-up" position and the silicon occupying the "buckled-down position". Mixed dimer [13] formation remains the predominant growth mechanism up to a surface concentration of 0.8ML germanium. First principles calculations also showed the predominance of mixed silicon-germanium dimers at sub-monolayer coverages [14] although when compared to the pure dimers, the mixed dimers are energetically more favorable only by a very small energy difference [15,

16]. While a significant number of pure germanium dimers are also formed on the surface as growth proceeds, some germanium atom also diffuse into deeper layers [13]. AES and XPS studies indicate significant diffusion as far as the 5^{th} surface layer after annealing at 873K [17]. From LEED studies, it was concluded that when a single monolayer of germanium is deposited onto the room-temperature silicon(100) substrate and then annealed at 523 - 873K, dimers form in the direction orthogonal to the substrate silicon dimer [18]. Both theoretical calculations and FTIR experiments indicates that only about one-fifth of this 1ML of germanium remain on the surface [19, 20], with the remainder diffusing sub-surface. The presence of surface hydrogen is known to suppress germanium segregation [21-28] and thus promotes the growth of desirable abrupt silicon-germanium interfaces.

While there is a good agreement between theoretical calculations and experimentally measured values of the pure silicon dimer bond lengths, both pure germanium dimers and mixed silicon-germanium dimers still see variances in the values of their calculated and measured bond lengths. For the clean germanium surfaces, the calculated dimer length for the asymmetric (2×2) and asymmetric c-(2×4) [12-14] comes closer to the experimental values than do those obtained from (1×2) reconstructions. For germanium dimers on the silicon (100) surface, all theoretical calculations point towards asymmetrical dimers. However, while some of these calculations found that the dimer length is approximately equal to the bulk germanium-germanium bond length [14, 15, 29-31], others show dimer bond lengths that are longer than the bulk germanium-germanium bond lengths [32, 33]. Experimentally, the germanium dimer bond lengths are measured to be longer than the bulk germanium-germanium bond lengths by both the surface-

extended x-ray adsorption fine structure technique [34] and the x-ray standing wave technique [35]. However, these two techniques could not agree whether the surface dimers are symmetrical or not. On the other hand, an STM [36] study identified some highly buckled dimers as mixed silicon-germanium dimers with germanium buckled up. These dimers flip about every 3s at room temperature and the observed "rocking" dynamics were argued to be the rotation of the silicon-germanium dimers instead of the up-down buckling dynamics. This argument was made based on some calculated barrier for rotation and dynamic buckling. The length for mixed silicon-germanium dimers on Si(100) varies considerably between the (1×2) reconstruction and the asymmetric c-(2×4) reconstruction. As with the germanium dimers, there is good agreement with experimental silicon-germanium dimer length for the larger reconstruction but not for the (1×2) reconstruction [37]. First principle calculations have shown that there is only a weak coupling between different types of surface dimers [38].

The mixed silicon-germanium dimers were observed to diffuse on the silicon surface. This diffusion is similar to that for the diffusion of pure silicon dimer. A barrier of 1.01 ± 0.09 eV [39] was proposed for the lowest energy, piecewise diffusion pathway of silicon-germanium on the silicon(100) surface. It has also been proposed that the piece-wise diffusion of these mixed dimers triggers the exchange of dimer germanium atom with a substrate silicon atom. The intermixing of germanium atom into the substrate substantially changes the energy landscape for surface processes such as diffusion and desorption to occur [39, 40].

2.2 The Hydrogenated Surface

When exposed to hydrogen, the surface dimers of Si(100) can take up hydrogen by breaking the weaker pi-bond within itself and forming a sigma bond with the hydrogen. Each silicon atom of the dimer can bond to one hydrogen forming monohydrides. The sigma bond within the dimer is preserved and thereby preserving the 2×1 reconstruction. When the coverage is below 0.2ML, hemihydrides are formed where only one silicon of the two in a dimer are bonded to hydrogen. Monohydrides are also known as doubly occupied dimers (DODs) while hemihydrides [41] are known as singly occupied dimers (SODs).

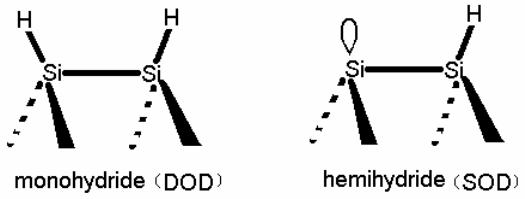

Figure2.3: An illustration of the monohydride and the hemihydride.

When germanium is deposited on a pre-hydrogenated silicon surface, it spontaneously substitutes for hydrogen and in-turn, hydrogen segregates to the outermost surface [25, 42, 43]. It has been observed that in the presence of hydrogen as surfactant, sharp silicon/germanium interfaces could be obtained [27, 44-46]. On the other hand, it is important to note that although hydrogen coverage on the surface does decrease the germanium segregation enthalpy [47] it does not eliminate germanium segregation completely.

Although the microscopic desorption mechanism of hydrogen from Si(100) is currently still a topic of active debate, the assignment of the thermal desorption spectral

peaks is already well established. The H_2 TPD spectrum for Si(100) after saturation at 210K exhibits three well defined peaks, the most dominant one being around 800K, another one around 650K and one between 350K to 550K. Each of these is assigned to hydrogen desorption from the different hydrogen-containing surface species. The highest temperature peak, also known as the β_1 peak, was assigned to the hydrogen desorbing from the monohydride species. The processes giving rise to this peak follows first order kinetics for medium to high surface coverage [48-51], and follows second order kinetics for very low surface coverage [49]. The first order kinetics of the desorption for medium to high surface coverage have been attributed to the preferential pre-pairing of hydrogen atoms on the silicon dimers [52-56]. The peak at around 650K is also known as the β_2 peak. It was assigned to the desorption from the SiH_2 species [57]. The processes giving rise to this peak follows second order kinetics [58]. Finally the low temperature peak, known as the β_3 peak, was assigned to the desorption from the SiH_3 on Si(100) [59]. It is interesting to note that while this peak is observed for the TPD of hydrogenated silicon(100) surfaces, it is not observed after the interaction of silane with the surface.

Table 2.1: Decomposition temperature of substrate-hydrogen bond estimated by different experimental techniques.

Type of bonds	Decomposition temperature	Techniques	Reference
Si-H on Si(100)	743K	HREELS	60
Si-H on Si(100)	798K	TPD	52, 61
Ge-H on Ge(100)	463K	HREELS	60
Ge-H on Ge(100)	563K	TPD	62

Table 2.2: Kinetic parameter for first order H_2 desorption from Si(100)

First Order Kinetics of H_2 desorption from Si(100)	Activation Energy	Pre-exponential factor
LITD [50]	1.95 ± 0.1 eV	2.2×10^{11} s^{-1}
LITD [48]	2.52 ± 0.1 eV	$(5.5 \pm 0.5) \times 10^{11}$ s^{-1}
TPD [61]	2.47 eV	2.0×10^{15} s^{-1}
SHG [49]	2.47 ± 0.1 eV	2.0×10^{15} s^{-1}
STM [63]	2.22 ± 0.2 eV	$3.4 \times 10^{(13 \pm 0.3)}$ s^{-1}

Table 2.3: Kinetic parameter for first order H_2 desorption from Ge(100)

First Order Kinetics of H_2 desorption from Ge(100)	Activation Energy	Pre-exponential factor
TPD [62]	1.82 eV	2×10^{15} s^{-1}
LITD(θ_H = 0.4 – 1.1 ML; 1 ML = 6.25 x 10^{14} Ge atoms/cm^2) [64]	1.73 ± 0.1 eV	$4 \times 10^{(13 \pm 1)}$ s^{-1}
STM [65] for H_2	1.65 ± 0.1 eV	$(2.7 \pm 0.5) \times 10^{13}$ s^{-1}
STM [65]for D_2	1.65 ± 0.1 eV	$(1.2 \pm 0.5) \times 10^{13}$ s^{-1}

In the low temperature epitxial growth regime, with temperature less than 823K, the silicon and silicon-germanium growth rate is limited primarily by hydrogen desorption kinetics [66].

On the germanium-doped silicon surfaces, germanium segregation and hydrogen desorption are mutually interactive processes. The presence of germanium on the silicon surface provides a lower-temperature hydrogen desorption channel. This was used to

account for the enhancement of growth rate of silicon-germanium alloy compared to pure silicon [67, 68]. On the other hand, HREELS studies on post–grown germanium-doped silicon found that some germanium hydrogen bonds were stabilized at around 600K due to the the presence of neighbouring silicon atoms [61, 69]. The mixed silicon-germanium dimer is proposed to be the candidate for germanium-hydrogen bond formation at a higher temperature.

2.3 The decomposition of Silane and Disilane

Silane and disilane have similar major decomposition products – the silyl group, the silylene group and hydrogen. However, the difference in the two growth precursors is that they have different sticking coefficient and their decomposition products exists in different neighborhoods.

2.3.1 Silane

The sticking coefficient is defined as the ratio of the rate of adsorption to the rate at which the adsorptive strikes the total surface. A variety of methods have been used to study the sticking coefficient of silane and disilane on silicon(100). They include thermal programmed desorption and ellipsometry.

For silane, it has been found that the initial sticking coefficient depends upon the incident kinetic energy, the substrate temperature and the surface hydrogen coverage. It is however essentially independent of the internal molecular energy distribution and only shows a weak isotope effect.

Table 2.4: Variation of initial sticking coefficient of silane with respect to surface temperature.

Surface temperature T_S	**Initial Sticking Coefficient S_0**	**Techniques**	**Reference**
150 K	10^{-2}	TPD	70
300 K	10^{-4}	TPD	71
375-775 K	10^{-5}	TPD	72
$\geq$ 670 K	$<3 \times 10^{-4}$	TPD	73-76
300 -773 K	7×10^{-3}	Ellipsometry	77

Desorption experiments [70, 71, 73-36] showed that the initial sticking coefficient of silane decreases with increasing substrate temperature while ellipsometry [77] showed a rather constant sticking coefficient over a wide temperature range. The latter also indicated that silane adsorption requires no activation.

The initial sticking coefficient of silane will increase with increasing incident kinetic energy of silane. Specifically, when the impinging flux has kinetic energy > 0.5 eV, the initial sticking coefficient doubles in the temperature range between 800K and 1200K. This doubling in sticking coefficient is attributed to a translationally activated adsorption channel. [78, 79]

It has also been found that the sticking coefficient of silane decreases rapidly with an increase in surface hydrogen coverage. For a temperature of 673K, the following table shows the trend of sticking coefficient with hydrogen coverage [80].

Table 2.5: Variation of sticking coefficient of silane with respect to the surface hydrogen coverage.

Hydrogen surface coverage θ_H	**Sticking Coefficient S**
0 – 0.2 ML	$S = S_0 = 3 \times 10^{-5}$
> 0.2 ML	$0.5\ S_0$
0.2 ML	$0.1\ S_0$
>0.4 ML	Below measurement limit

The initial decomposition step of silane on Si(100) is deduced based on SSIMS results [70, 73, 74, 76, 80, 81] to be as follows:

$$SiH_4 + 2db \rightarrow H(a) + SiH_3(a)$$

It has been proposed, by the use of density functional calculations [82], that the above reaction occurs via the interaction of one the hydrogen atom on the SiH_4 with the electrophilic atom of an asymmetric substrate silicon dimer. This interaction should result in the dissociation SiH_4 into one hydrogen atom and one silyl group both residing on adjacent dangling bonds of the same substrate dimer. This mechanism involves a barrier of about 0.5-0.6 eV.

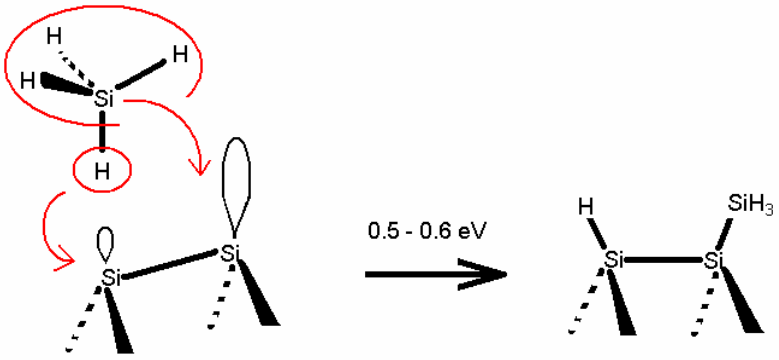

Figure 2.4: An illustration of silane decomposition.

If the adsorption takes place at or below 300K, both the hydrogen and the silyl group remain on the surface with no hydrogen desorption. This is supported by the fact that exposure to SiH_4 at 293K left the surface saturated with one quarter as much silicon as hydrogen [83, 84].

An attempt to study the reactive sticking coefficient of thermal SiH_4 on Si(100)-(2×1) by a Japanese group revealed that the order of silicon growth kinetics is different for high temperature and low temperature growth [85-87]. For growth at T > 850 K, the growth rate has a fourth order dependence on the concentration of dangling bonds. However, for growth at T < 850K, growth follows a second order rate equation. This observation leads to the conclusion of a different decomposition mechanism at these two temperatures. They proposed that at low temperature, growth takes place via a two step reaction, each step requiring two dangling bonds, while at high temperature, growth takes place via a single step decomposition involving four dangling bonds.

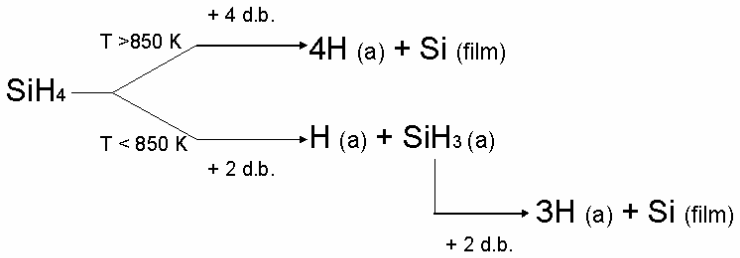

Figure 2.5: SiH_4 decomposition at different temperature regime.

2.3.2 Disilane

Similar to the case of silane, the initial sticking coefficient of disilane is dependent upon the incident kinetic energy of the impinging molecule, the substrate

temperature and the hydrogen surface pre-coverage. The sticking coefficient decreases considerably for surface with hydrogen adsorbed. For disilane, the initial sticking coefficient is independent upon the internal energy distribution and it shows no kinetic isotope effect.

Table 2.6: Variation of initial sticking coefficient of disilane with respect to surface temperature at different incident kinetic energy

Incident Kinetic Energy of Si_2H_6	**Initial Sticking Coefficient S_0 vs Temperature T_S**	**Reference**
< 100 meV	S_0 decrease with increase in T_S	79
> 0.5 eV	S_0 increase with increase in T_S	79, 88, 89

The increase of the initial sticking coefficient with increasing temperature for Si_2H_6 impinging the surface at kinetic energy greater than half an electronvolt has been attributed to two different possible adsorption channels, namely, adsorption via a precursor state and adsorption via a translationally activated adsorption channel [79, 88, 90-92].

The adsorption mechanism of disilane is dependent upon the incident kinetic energy, the surface temperature, the presence or absence of gas phase chemistry, and the hydrogen coverage on the Si(100) surface. The table below summarizes the fragments observed at various temperatures.

Table 2.7: Fragments of Si_xH_y observed with respect to temperature

Temperature	Fragments observed	Techniques	Reference
< 90 K	Molecular Si_2H_6	UPS	93, 94
> 150 K	Si-H and Si-SiH_3	UPS	93
150 K	-SiH_3, -SiH_2, -SiH	SSIMS	70, 81
200 K	Mainly -SiH_3, small quantities of SiH and SiH_2	FTIR	95
300 K	Mainly SiH_2 and unpaired H and SiH_3 that decomposed within minutes	STM	96, 97
300 K	SiH_2, SiH, SiH_3 (minority)	MIRIS	94, 98
300 K	SiH and SiH_2 and/or SiH_3	STS	99
R.T.	Mainly SiH_2	ELS	100, 101

At temperatures below 90K, disilane adsorbs on Si(100) as a molecule without dissociating [93, 94]. This physisorbed state can return to the desorbed state in the temperature range between 120 and 200K [70, 81, 93]. As temperature rises above about 150 K, the disilane begins to dissociate on the Si(100) surface, giving rise to the silyl group, the silylene group and hydrogen [70, 81, 93-100]. Evidently, the cleavage of the Si-Si bond occurs prior to the scission of the Si-H bond. When the surface has high hydrogen coverage or when the impinging disilane molecule has a very high kinetic energy, silane gas would be liberated as a by-product of the dissociation.

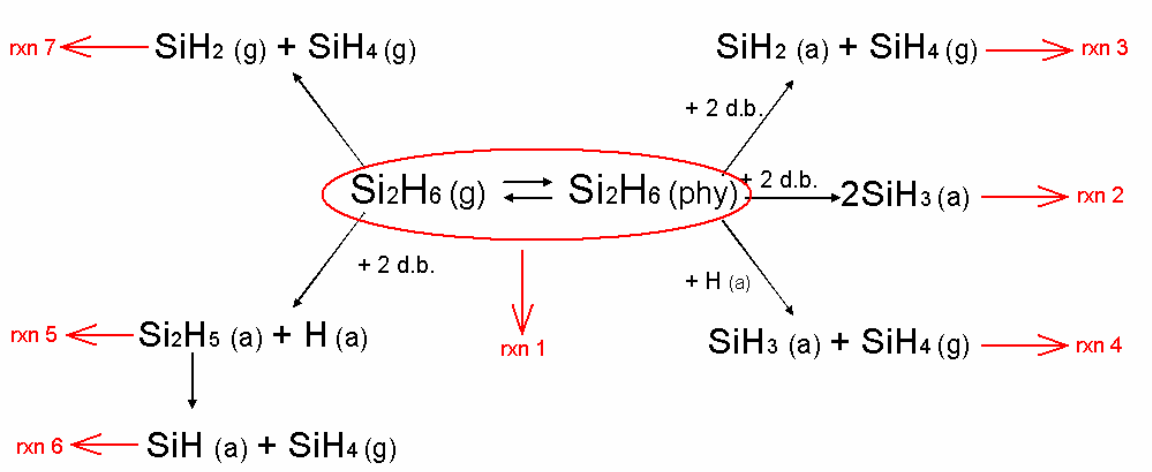

Figure 2.6: Si_2H_6 decomposition mechanism

Figure 2.6 summarizes a list of possible reactions that could occur when disilane interacts with the Si(100) surface. Reaction 1 (labeled as rxn 1) is the reversible molecular physisorption of disilane which takes place at very low temperature. This physisorbed state is also known as a precursor state that is used to explain the decreasing trend of sticking coefficient with increased temperature. Since silyl groups are observed as majority species at temperatures below room temperature, disilane can also possibly dissociate into two silyl groups. This is represented by reaction 2 (labeled as rxn 2). These two silyl groups can dissociate on a single silicon dimer or can dissociate on adjacent silicon dimer in the same dimer row [102]. Although one would expect to see silyl group to exist in pairs on the surface as a result of reaction 2, STM observed statistical distribution of these silyl groups [100]. This lack of pair correlation was attributed to the transient mobility that arises from the energy released by the dissociation.

Silane was liberated during the adsorption of disilane on Si(100) with moderate to high surface H coverage [92, 103]. Reactions 3-6 were proposed to account for that. Reaction 3 was proposed to account for the insertion of the SiH_2 groups into surface Si-H

bonds when hydrogenated Si(100) surface [81, 99, 104] and polycrystalline silicon surface [105] was exposed to disilane. It cannot be the sole reaction that occurs since the silyl group is experimentally observed to co-exist with the silylene species. On the other hand, reaction 4 was supported by the relatively high hydrogen coverage per Si atom found on the surface after it was exposed to disilane for growth below 700K [75, 81]. This reaction was also further supported by other growth studies [86, 91]. Reactions 5 and 6 were proposed for disilane impinging the surface at very high incident kinetic energy [92].

2.4 Decomposition of Silyl group and the configuration of the decomposition product

At around room temperature, the silyl group is the main product of silane and disilane decomposition [70, 72, 73, 81, 106]. The mechanism of the subsequent decomposition of the silyl group depends on the growth precursor. When silane is the precursor, the silyl group decomposes without liberating hydrogen gas via the following reaction:

$$SiH_3(a) + 2d.b. \rightarrow H(a) + SiH_2\ (a)$$

However, when disilane is the precursor, the decomposition mechanism of the silyl group depends on the disilane exposure. Hydrogen will be liberated around 450K during the silyl group decomposition when the disilane exposure is high (between 50 and 500 L). Otherwise, the silyl group will decompose without liberating hydrogen gas [93, 107].

The silyl group that originates from silane decomposes 20 times faster than that from disilane. This difference has been attributed to the different local environment due to the significant coverages of both SiH and SiH_2 derived from SiH_3 group in right after silane and disilane decomposition. [70] From that report, SiH_3 species derived from disilane have more such SiH_x species which blocks sites for SiH_3 decomposition.

Table 2.8: Kinetic parameters for the decomposition of silane and disilane

Precursor	Pre-exponential s^{-1}	Activation Energy /eV	Reference
Silane	0.5 - 5	0.05 – 0.13	70
Disilane	50	0.27	70
Disilane	2×10^5	0.57 ± 0.15	102

On average, the silyl group has a life time of several minutes at room temperature. STM and FTIR studies shows that when the silyl group decomposes without liberating hydrogen, it produces a hydrogen atom and the silylene species on the surface in equal proportion [96, 98, 100].

It is possible for us to envisage a variety of ways by which the silylene group can orientate on the surface. Since a sp3 hybridised silicon atom can have four bonds, the silyene group can make two bonds to the substrate. Four of the possible configurations are shown in the figure 2.7 below – the intra-row, the on-dimer, the in-dimer and the inter-row configuration. The intra-row configuration refers to the configuration where the silyene group straddles two adjacent dimers of the same dimer row. The on-dimer configuration and the in-dimer configuration, on the other hand, refer to the configuration

that straddles a single dimer. The on-dimer configuration preserves the dimer sigma bond while the in-dimer configuration breaks the dimer sigma bond. The inter-row configuration refers to the configuration where the silylene group straddles two adjacent dimers belonging to two different dimer rows.

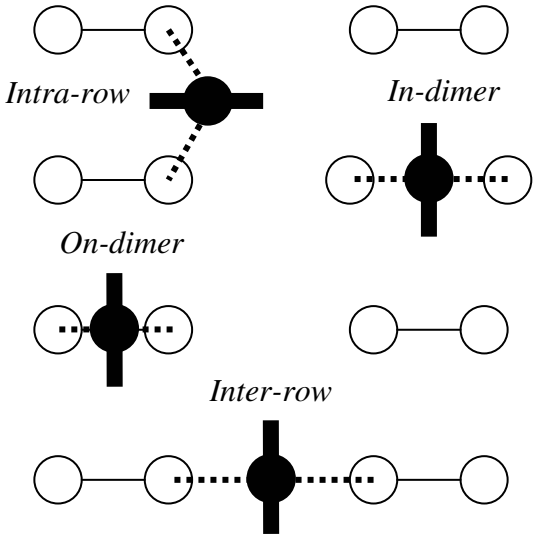

Figure 2.7: Local arrangement of the silylene species on the Si(100) surface

Experimentally, only the intra-row configuration has been observed by STM [41, 96, 100]. MIRIS study of the adsorption of silane on the Si(100) also showed that at low hydrogen coverage, the silane molecule dissociatively adsorbes on the Si(001)-2×1 to populate the intra-row site [108]. The in-dimer configuration and the inter-row configuration have been argued against theoretically due to their high relative energy with respect to the other surface configuration [109]. The only configuration, other than the intra-row configuration, that is shown to be energetically favoured is the on-dimer configuration. In fact, first principles calculations showed that the on-dimer configuration was even more stable than the intra-row configuration. However, the interaction energy

of two silylene groups in the on-dimer configuration was less favourable than that of two intra-row silylene group. This was used to argue against the possibility of the on-dimer configuration being the configuration leading to growth. It was later shown that the presence of hydrogen on the surface alters the relative stability of these configurations [110, 111]. In the presence of hydrogen, the intra-row configuration becomes more stable than the on-dimer configuration. Since hydrogen atoms are always present on the growing surface if a hydride source is used, this was used to explain why the intra-row configuration was the only configuration observed experimentally.

2.5 Decomposition of Silylene group

SiH_2 has been reported as the majority SiH_x species in the temperature regime of 500K to 690K [112] and its decomposition mechanism follow a second order kinetics. From the work by S.M Gates *et. al.* [113], two mechanisms for SiH_2 decomposition are experimentally distinguished; competition of these is governed by surface coverage. At low surface coverages, SiH_2 decompose between 650K and 775K, while at high surface coverages, the SiH_2 group decomposes from 750K onwards. The mechanism and rate of decomposition of surface SiH_2 are thought to be dependent on the local surface environment near these species. TPD studies of the SiH_2 decomposition mechanism found that at an initial silylene of below 0.2 ML, SiH_2 decompose without hydrogen desorption. At higher coverages, however, the SiH_2 decomposition process involves hydrogen desorption.

TPD studies also revealed that the intensity of the desorption peak originating from the decomposition of silylene group, the β_2 peak, is affected by the temperature at

which the disilane gas is being adsorbed. If the surface is exposed to disilane at 200K, the SiH_2 coverage is seen to increase upon annealing [98]. This is due to the decomposition of the SiH_3 group left on the surface after disilane decomposition. However, if the surface is exposed to disilane at around 375K to 400K, no β_2 peak is observed [114-117].

Table 2.9: Kinetic parameters for the decomposition of SiH_2

Pre-exponential s^{-1}	**Activation Energy eV**	**Reference**
4.7×10^{-2}	1.87	58
$4 \times 10^{0-1}$	1.96 ± 0.04	113

H. Noda *et. al.* [118] studied the bending and stretching vibrational spectra. They proposed a mechanism for the thermal decomposition of SiH_2 on Si(100) surfaces, involving two kinds of SiH_2 species: the adjacent dihydride and the isolated dihydride. The adjacent dihydride is less stable than the isolated dihydride. An illustration is shown in Figure 2.8 below.

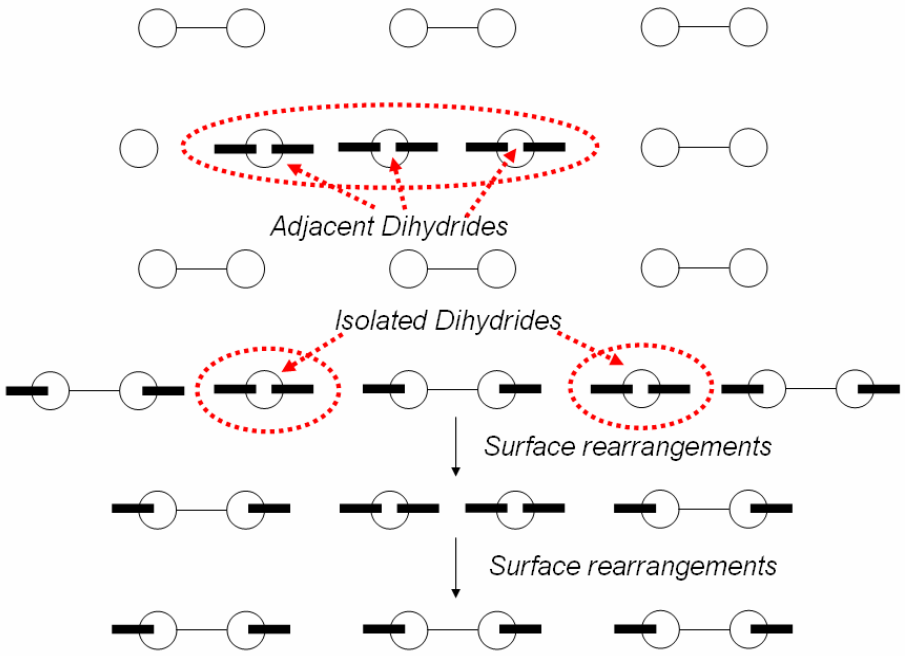

Figure 2.8: A schematic diagram showing the two types of dihydrides – adjacent dihydrides and isolated dihydrides. An illustration of how coupled monohydride can be generated by the surface rearrangements of isolated dihydrides.

Both adjacent dihydrides and isolated dihydrides can produce coupled monohydrides by thermal decomposition via second order kinetics 2(H-Si-H) → H-Si-Si-H + H_2 [48]. Since surface H migrates at elevated temperatures [119], the thermal reaction of isolated dihydride may generate coupled mono hydride by the decomposition reaction accompanied by the rearrangement of H.

Table 2.10: Temperature window for SiH_2 decomposition estimated by different techniques.

Technique	SiH_2 decomposition Temperature Window	Reference
TPD	420 – 500 K	98
MIRIS	< 450 K	98
Photoelectron	500 – 610 K	
ELS	655 – 705 K	94
SSIMS	650 – 775 K	114

Ad-dimers were observed by STM after the surface has been annealed beyond the decomposition temperature of the silylene group. These ad-dimers, believed to be the decomposition product of the silylene group, are oriented perpendicularly to the substrate dimers [99, 120]. Figure 2.9 depicts a possible scenario of how these silylene groups decompose to form rotated dimers. This mechanism has been proposed by Hamers [96] and Owen [121].

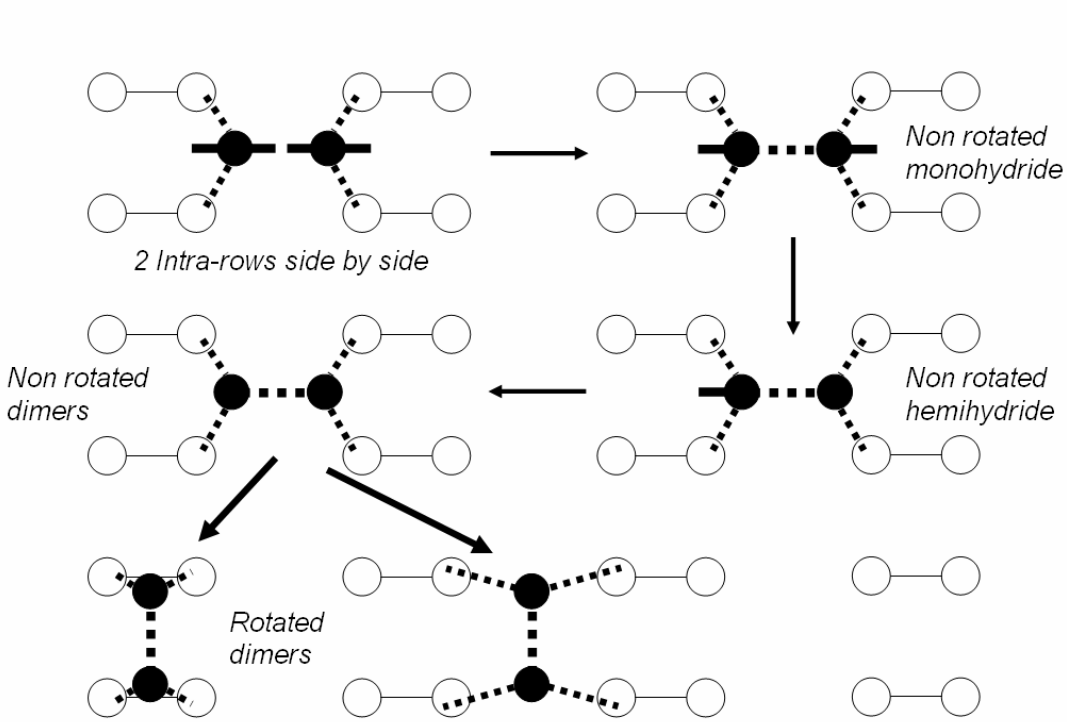

Figure 2.9: A schematic diagram showing the possible decomposition mechanism of silylene group.

It was proposed that two intra-row silylene groups diffuse to adjacent dimer rows and combine with each other to form a non-rotated monohydride dimer liberating hydrogen gas as a result. This non-rotated monohydride dimer later loses all its hydrogen and eventually rotates into the epitaxial position.

2.6 Diffusion of silylene

As mentioned in the previous section, the SiH_2 species has been reported as the majority SiH_x species in the temperature regime of 500K to 690K [112]. One of the proposed mechanisms for the silylene fragment to decompose involved the combination of two silylene groups to give a monohydride dimer and hydrogen gas [96, 121].

$$2\ SiH_2 \rightarrow H\text{-}Si\text{-}Si\text{-}H + H_2$$

The second-order kinetics of this reaction, as evident from temperature-programmed desorption (TPD) experiments, suggests that there is no pre-pairing of the silylene species. Thus it reveals the importance of silylene diffusion in silicon agglomeration which in turn affects growth.

By approximately 470 K, the silylene fragments are already mobile [121] as shown by STM and growth experiments. Indeed, earlier STM data also implied that the silylene species is mobile at room temperature although it was not clear at that time if the mobility at this temperature is transient or intrinsic [97]. More recent investigations of island growth kinetics yield an effective diffusion barrier of 1.3 eV [122]. These experimental probes of silylene diffusion yield only an upper limit for the diffusion barrier, and are indirect because of the large number of other elementary surface processes, such as the co-adsorption of hydrogen atoms and the decomposition of silylene fragments, occurring. Furthermore, these experiments are also unable to directly elucidate the diffusion pathway.

In Bowler's attempt to estimate the energy barrier and diffusion mechanism of a silylene species along the dimer row [123] by theoretical methods, he uses the local density approximation (LDA) to map out the potential energy surface for diffusion of the silylene species. In his work, he identified three paths as illustrated in fig. 2.10, the on-dimer to on-dimer path with the barrier of 1.4 eV, the intra-row to intra-row path also with a barrier of 1.4 eV, and the on-dimer to intra-row path with a low barrier of 1.1 eV. It was found that silylene diffusion along the dimer row occurs via a preferred zig-zag path, illustrated by small slanted arrows on Fig. 2.10, from on-dimer to intra-row and then from intra-row to on-dimer.

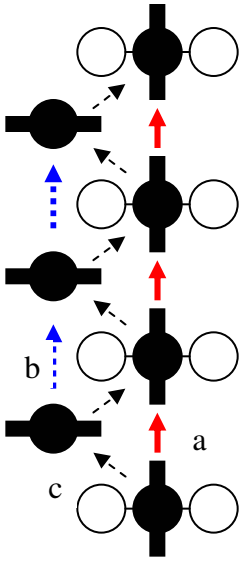

Figure 2.10: An illustration of the diffusion mechanisms proposed by Bowler et. al. [112] (a) on-dimer to on-dimer hop (represented by red arrows) with a barrier of 1.4 eV (b) intra-row to intra-row hop (represented by blue arrows) with a barrier of 1.4 eV (c) on-dimer to intra-row (represented by black arrows) with a barrier of 1.1 eV

Compared to the silylene species, the diffusion of the silicon ad-atom has been more thoroughly studied [25, 42, 43, 124-129]. For the silicon ad-atom, the diffusion barrier E estimated from STM data at temperatures between 350 and 550 K is approximately 0.67 ± 0.08 eV along dimer row and 1 eV along the dimer bond. A few other groups have used classical molecular dynamics [128, 129] and first-principles total energy calculations [126, 127, 130] to identify the adsorption site of silicon ad-atoms and the diffusion mechanism and barrier. From these studies, it was found that silicon ad-atom demonstrates diffusion anisotropy with a preferred direction along the dimer row with a barrier ranging from 0.55 to 0.75 eV. The anisotropic diffusion takes place via a pathway equivalent to Bowler's on-dimer to on-dimer hop (Fig. 2.10).

The surface diffusion barrier of the silicon ad-atom is also affected by the different concentration of co-adsorbed hydrogen ad-atoms. By the use of STM, it was observed that in the presence of co-adsorbed hydrogen ad-atoms, the silicon ad-atom

diffusion barrier along the dimer row doubled at very small hydrogen coverage [125]. On the other hand, it was found by first principles calculations using the LDA approximation that when the hydrogen coverage is increased to one monolayer the diffusion mechanism becomes substantially modified such that the barrier becomes similar to that for diffusion on a clean surface [42, 43]. With hydrogen coverage greater than one monolayer, however, the diffusion barrier is estimated to be so high (between 2.2 to 2.7) [25] that it can account for why growth becomes eventually disrupted [131]. It has been proposed that the silicon is more likely to hop in the direction perpendicular to the dimer row when it approaches a hydrogen-terminated silicon dimer [25].

2.7 Diffusion on Strained Silicon

Silicon can be pseudo-morphically grown over a silicon-germanium substrate to obtain strained silicon. With the increasing importance of strained silicon in the microelectronics industry, the understanding of ad-atom behavior on strained silicon become increasingly valuable. The strain dependencies of ad-atom binding and migration energies have an impact on the island growth kinetics in the hetero-epitaxial growth of lattice-mismatched thin films as well as on the film morphology. Since it is hardly possible to experimentally isolate the effect of strain on diffusion mechanism, they are most conveniently studied by using first-principles calculations.

Molecular dynamics studies performed by Roland and Gilmer [132] aimed at elucidating the effects of strain on the diffusion of ad-atoms. In this study, which used the Stillinger-Weber potential, the diffusion barrier along the dimer row is found to increase by about 10% for a 3% compressive as well as for 2% tensile strain. However, Spjut and

Faux [133] found that the diffusion barrier is lowered by the application of a 1% to 1.5% tensile strain to the substrate, in the direction perpendicular to the dimer row.

On metal surfaces, surface diffusion rates are found to be very sensitive to the presence of lattice mismatch-induced strain. For instance, on the strained Ag(111) surface, experimental and theoretical studies found good agreement in the effect of strain on the diffusion barrier. It was shown by experiment [134] that the diffusion barrier of Ag-atoms does decrease significantly as the surface is strained compressively by about 4%. Theoretical methods have also been used to show that within a strain of ±5%, the diffusion barrier varies linearly with respect to strain with the tensile or compressive strain causing the increase or decrease of diffusion barrier respectively. This is in agreement with the molecular dynamics by Schroeder and Wolf [135] which gave a generalization on the dependence of diffusion barrier on the strained (100) surfaces. Such generic models where the bonding is non-directional are probably not applicable to diffusion on the covalently defined silicon surface.

While it is now generally accepted that tensile strain increases the surface diffusion barrier of ad-atoms on metal surfaces and compressive strain enhances the rate of diffusion, we can expect the dependence of diffusion barrier on strain on the silicon surface to be different. Hence, it can be seen that while metal surfaces gave a clear trend of the effect of strain on diffusion barrier, on the semiconductor surfaces there is still no clear understanding of this.

Other more recent first principles calculations, performed to study diffusion on strained surface include the study of silicon ad-atom diffusion on strained silicon (111) surface [136] and the study of germanium ad-atom on strained silicon (100) and

germanium (100) surface [137]. These investigations using Gaussian94 [136] and VASP [137] showed that diffusion barrier of surface ad-atom decreases under tensile strain or compressive strain, respectively. The decrease in the diffusion barrier for both cases is around 0.1eV.

On the experimental side, Zoethout *et. al.* have attempted to study the diffusion of silicon ad-dimer along the dimer row of a strained silicon (100) surface [138]. It was found that the rate of diffusion of a silicon dimer along the substrate dimer rows on silicon (100) is relatively insensitive to tensile strain.

As the importance of strained material continue to gain importance both in research and industrial applications, it is therefore important for us to understand how strain affect the diffusion process on the surface during growth. We have therefore performed first-principle's calculations on the diffusion on strained silicon surfaces. It is the aim of this work to study the effects of strain and Ge-doping on the diffusion of SiH_3 decomposition products on silicon surfaces.

3 Theoretical Background

3.1 The Schrödinger Equation

At the heart of most quantum chemical calculation lies the time independent, non-relativistic Schrödinger equation of the form

$$\hat{H}\,\Psi = E\,\Psi \qquad \text{Eqn. 01}$$

The Schrödinger equation is an eigenvalue equation with H being the Hamiltonian operator, the energies (E) being the eigenvalues and a set of wavefunctions (Ψ) being the eigenfunctions.

The Hamiltonian operator is a differential operator that can be broken down in to its kinetic energy terms and its potential energy terms as follows. If we assume that the mass are measured in units of electron mass and ħ in the Hamiltonian equals to 1,

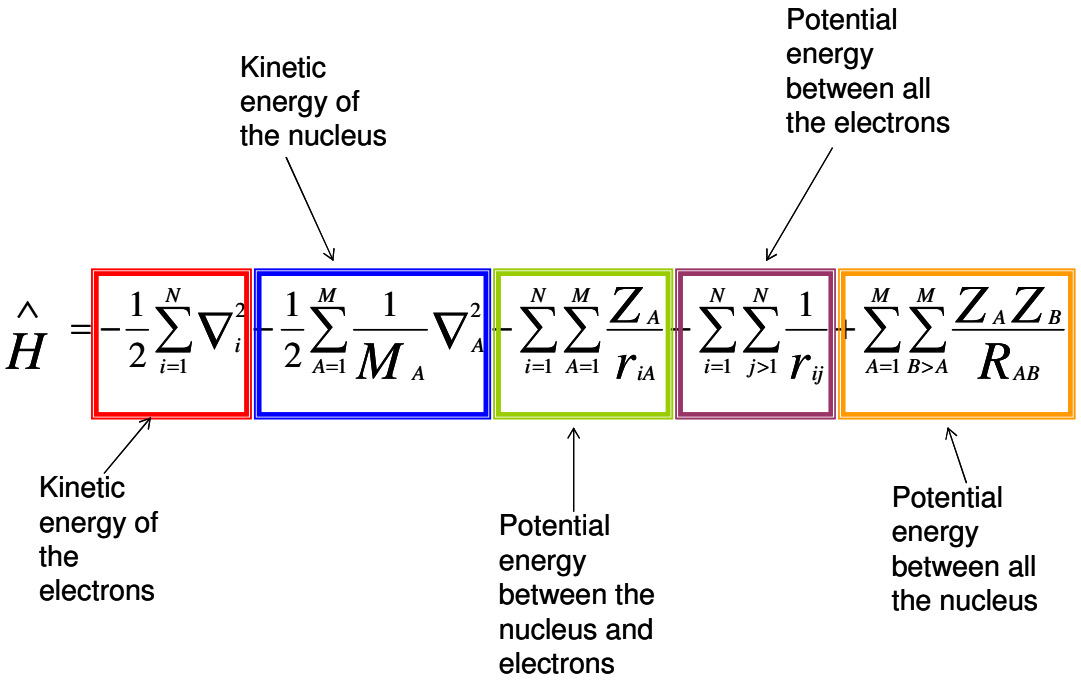

Figure 3.1: An illustration of the individual terms in the Hamiltonian and what they represent. While i and j run over N electrons, A and B denote the M nuclei in the system of interest.

The Laplacian ∇_α^2 operator in figure 1 is defined as a sum of differential operators in Cartesian coordinates,

$$\nabla_\alpha^2 = \frac{\partial^2}{\partial x_\alpha^2} + \frac{\partial^2}{\partial y_\alpha^2} + \frac{\partial^2}{\partial z_\alpha^2} \qquad \text{Eqn. 02}$$

While M_A denotes the mass of nucleus A in atomic units, r_{ij} (and R_{AB}) represents the distance between particles i and j (and A and B).

Although the Schrödinger equation for a hydrogen atom can be solved exactly, an exact solution is not possible for any molecule, even H_2^+, because the simplest molecule consists of three particles (two nuclei and one electron). This complicated energy balance must be simplified by applying several approximations to make the problem solvable. These approximations shall be introduced in the following discussion and they include:

1 The Born-Oppenheimer approximation.

2 HF approximation (Many-body problem to a single-body problem)

3 Density functional theory

4 Solid State Symmetry

5 Treating the nucleus and the inner electrons collectively as ions by applying pseudopotentials.

3.2 Born-Oppenheimer approximation

First, in the Born-Oppenheimer approximation, also known as the clamped-nuclei approximation, the nuclei is assumed to have negligible kinetic energy as implied in its name. The approximation is justified since even the lightest of all nuclei (hydrogen nuclei)

is many hundreds times (~1800 times) heavier than an electron. Thus, the nuclei would be moving very much slower than electrons. In view of this approximation, the nuclei kinetic energy term in the Hamiltonian disappears leaving the electronic Hamiltonian to include only the kinetic energy of the electrons, the potential energy arising from the interactions of the electrons and the potential energy between the stationary nuclei and the electrons.

$$\hat{H}_{elec} = -\frac{1}{2}\sum_{i=1}^{N}\nabla_i^2 - \sum_{i=1}^{N}\sum_{A=1}^{M}\frac{Z_A}{r_{iA}} + \sum_{i=1}^{N}\sum_{j>1}^{N}\frac{1}{r_{ij}} = \hat{H}_{k,e} + \hat{H}_{p,n-e} + \hat{H}_{p,e-e} \qquad \text{Eqn. 03}$$

The nuclear repulsion term is now represented by a constant

$$E_{nucl} = \sum_{A=1}^{M}\sum_{B>A}^{M}\frac{Z_A Z_B}{R_{AB}} \qquad \text{Eqn. 04}$$

and the total energy of the system can be calculated as

$$E_{total} = E_{elec} + E_{nucl} \qquad \text{Eqn. 05}$$

where the electronic energy can be calculated as the eigenvalues of

$$\hat{H}_{elec}\Psi_{elec} = E_{elec}\Psi_{elec}. \qquad \text{Eqn. 06}$$

Now, we only need to seek the eigenvalue of this simplified equation.

3.3 Variational Principle

A straight forward strategy hinted by the seemingly simple equation above is to first set up the Hamiltonian operator particular to the system that one is interested in and there after to find to the eigenfunctions Ψ and the corresponding eigenvalues E of Ĥ.

However, this algorithm is of no practical relevance, except in a few trivial examples, and a strategy to the exact solution of the Schrödinger equation is not known.

Fortunately, a systematic approach to finding the ground state wavefunction Ψ_0 which in turn delivers the ground state energy E_0 is available. This is known as the Variational Principle. This principle states that the energy computed from a guessed Ψ is an upper bound to the true ground state E_0.

$$E\,[\Psi_{trial}] = \left\langle \Psi_{trial} \middle| \hat{H} \middle| \Psi_{trial} \right\rangle = E_{trial} \geq E_0 = \left\langle \Psi_0 \middle| \hat{H} \middle| \Psi_0 \right\rangle \qquad \text{Eqn. 07}$$

Within this theorem, full minimization of the functional $E[\Psi]$ with respect to all allowed N-electron wave functions will give the true groundstate wavefunction Ψ_0 and energy $E[\Psi_0]=E_0$.

$$E_0 = \min_{\Psi \to N} E\,[\Psi\,] = \min_{\Psi \to N} \left\langle \Psi \middle| \hat{H}_{k,e} + \hat{H}_{p,n-e} + \hat{H}_{p,e-e} \middle| \Psi \right\rangle \qquad \text{Eqn. 08}$$

Since it is generally impossible to search through all allowed N-electron wave functions to find the true ground state Ψ_0, a suitable subset which offers a physically reasonable approximation to the exact wavefunction, would usually need to be chosen such that the minimization can be done in some algebraic scheme.

In summary, the recipe to systematically solve the Schrödinger equation is first to construct the electronic Hamiltonian from the number of electrons N and the interaction between the nucleus and electrons which is defined by the charge Z_A and position R_A of the nucleus. From the Hamiltonian constructed, we can in principle find the ground state electronic wavefunction by minimizing the energy with respect to all allowed wavefunctions. The groundstate wavefunction will in turn enable the determination of the ground state energy and all other properties of the system of interest.

3.4 Many-body problem

Although the Born-Oppenheimer approximation has reduced the full Schrödinger equation to one that only involves the electronic degrees of freedom, it is still not possible to solve the equation analytically for problems involving more than 1 electron.

We need to first understand the many-body problem before a method employed to approximate it can be discussed.

As an example, we can think of tennis balls moving on the tennis courts as analogous to electrons moving in solids. If we only have one tennis ball in the court, it is moving in some kind of force-field uncoupled to its own motion. Now, if we know the force acting on the ball at each point in space-time, the trajectory of the tennis ball can be mapped out easily using Newton's law. This is like a single particle moving in the influence of an external field.

If we now have a second tennis ball attached to the first by a spring, then the problem becomes a many body problem. The motion of each ball is now in the influence of a force-field coupled to its own motion through the spring. Although the motion of the balls can still be described by Newton's law of motion, the equation of motion must now be solved simultaneously. This is an example of a many body problem analogous to electrons moving in solids. The electrons are moving in force fields that are coupled to their own motion. The many-body problem grows out of hand as the number of mutually interacting body grows bigger. In fact, the three body problem of the sun-moon-earth interaction cannot be analytically solved. One of the earlier attempts to simplify the many-body problem is made by Hartree and it is subsequently improved to what is now famously known as the Hartree-Fock approximation.

3.5 Hartree and Hartree-Fock methods

In an attempt to dissect the many-body problem into digestible chunks, Hartree proposed to treat the many electron wavefunction as a product of a set of single electron wavefunctions. In a system with N electrons, there will be N equations that takes the form similar to the time-independent Schrödinger equation with the exception that the motion of these electrons is no longer coupled to the external potential (Hartree potential due to coulomb interaction). This assumption allows each electron to be treated as a single particle moving under the influence of an external field that is uncoupled to its own motion. This allows the problem to be solved with the help of variational principle. Unfortunately, Hartree's approximation failed to give good agreement to reality due to a loophole in the assumption made – the Pauli Exclusion Principle is violated.

The Pauli Exclusion Principle states that it is not possible for two fermions to exist at the same point in space with the same set of quantum numbers. This principle is mathematically accounted for by ensuring that the wavefunction of a set of identical fermions is antisymmetric under exchange of any pair of particles.

The Hartree-Fock method is an improvement to the Hartree method as it considers the effect of the Pauli Exclusion Principle when constructing the N-electron wave function. In the Hartree-Fock approximation, the N-electron wave function is approximated by an antisymmetrized product (Slater determinant, Φ_{SD}) of N one-electron wave functions $\chi_i\left(\vec{x}_i\right)$.

$$\Psi_0 \approx \Phi_{SD} = \frac{1}{\sqrt{N!}} \begin{vmatrix} \chi_1(\vec{x}_1) & \chi_2(\vec{x}_1) & \cdots & \cdots & \chi_N(\vec{x}_1) \\ \chi_1(\vec{x}_2) & \chi_2(\vec{x}_2) & & & \chi_N(\vec{x}_2) \\ \cdots & \cdots & & & \cdots \\ \cdots & \cdots & & & \cdots \\ \chi_1(\vec{x}_N) & \chi_2(\vec{x}_N) & \cdots & \cdots & \chi_N(\vec{x}_N) \end{vmatrix} \quad \text{Eqn. 09}$$

or alternatively

$$\Psi_0 \approx \Phi_{SD} = \frac{1}{\sqrt{N!}} \det\left\{\chi_1(\vec{x}_1)\chi_2(\vec{x}_2)\ldots\chi_N(\vec{x}_N)\right\} \quad \text{Eqn. 10}$$

The one electron wave functions $\chi_i(\vec{x}_n)$ called spin orbitals are composed of a spatial orbital $\phi_i(\vec{r})$ and one of the two spin functions, $\alpha(s)$ or $\beta(s)$.

$$\chi_i(x) = \phi_i(\vec{r})\sigma_i(s), \qquad \sigma_i = \alpha, \beta \quad \text{Eqn. 11}$$

where *i* is the quantum number for spatial parts and spin.

The spin functions are orthonormal. And the energy is minimized by searching through a basis set of Slater determinant.

$$E_{HF} = \min_{\Phi_{SD}\to N} E[\Phi_{SD}] = \langle \Phi_{SD} | \hat{H} | \Phi_{SD} \rangle = \sum_i^N \left(i \left| \hat{h} \right| i \right) + \frac{1}{2}\sum_i^N \sum_j^N (ii|jj) - (ij|ji) \quad \text{Eqn. 12}$$

It is important to note that the Hartree-Fock energy is a function of the spin orbital. Due to the constraints on the spin orbitals, a set of pseudo-eigenvalue equations can be established to identify the "best" spin orbitals to be used. The problem is a so-called "pseudo-eigenvalue" because the operator itself depends on the very solutions of the problem that needs to be solved. Thus, we need to use the self-consistent field technique to resolve the problem. That is, by starting with a "guessed" set of orbitals, the equations

are iteratively solved until the input and the output orbitals differ by less than a preset tolerance level.

The improved Hartree-Fock approximation describes electrons moving in both the Hartree potential (arising from coulomb interactions) as well as the exchange potential. The exact electron-electron interaction is approximated using a self-consistent mean-field approach. However, it was found that the Hartree-Fock approximation gave an even poorer agreement with the experiment than Hartree's theory. The problem arises from the fact that although Hartree approach violates Pauli Exclusion Principle, the approach also neglected the electrostatic correlation of electrons. These two neglected effects actually negate each other, thus bringing Hartree's approximation closer to reality.

While the exchange potential accounts for the adherence to the Pauli Exclusion Principle, the phenomenon of electron correlation is not so directly represented. Electron correlation is the difference between the exact ground state energy and the energy calculated with the Hartree-Fock approximation. This phenomenon includes two parts, the dynamical electron correlation and the non-dynamical or static correlation. The dynamical electron correlation accounts for the instantaneous repulsion of the electrons when they are allowed by the Hartree-Fock scheme to come too close to each other. On the other hand, the static correlation accounts for the deviation of the ground state Slater determinant from the true ground state wave function.

In small molecules where the number of electrons involved is small, the Hartree-Fock approximation would still be valid. However, both of these approximations would fail in describing electrons moving in solids where the number of electrons involved is tremendous. Despite their inadequacy, these two methods have laid important

foundations in theoretical calculation methods as they elucidated two important phenomenons – exchange and correlation. On a similar note, these methods have also introduced the idea of how a non-interacting reference system could be used to solve problems dealing with atoms and molecules. These concepts are important fundamentals on which the Density Functional theory is built on.

3.6 Density Functional theory

The N-electron wavefunction, approximated above as an antisymmetrized product (Slater determinant, Φ_{SD}) of N one-electron wavefunctions, is a function of 3N spatial coordinates and N spin coordinates. The wavefunctions are very complicated quantities that are experimentally inaccessible. With the above properties, it renders the wavefunction to be something unpleasant to work with.

The density functional theory is a theory that attempts to simplify complicated wavefunction-based problems into problems that are based on another variable – the electron density. Unlike the wavefunctions, the electron density is a function of only 3 spatial variables. It is also an experimentally measurable quantity that one can visualize by intuition.

It is also interesting to note that other than being able to replace the complicated wavefunctions, the electron density is also able to provide all the necessary ingredients for setting up the system-specific Hamiltonians. A careful inspection of Eqn. 03 reveals that the electronic Hamiltonian operator of any atomic or molecular system is uniquely defined by N, the number of electrons, R_A, the position of the nuclei in space, and Z_A, the charges of the nuclei. It happens that the integration of the electron density over the entire

space domain gives the number of electron, N. Furthermore, while the electron density has maxima at the positions of the nuclei in space, R_A, the density at the position of the nucleus contains information about the nuclear charge Z. Hence it makes perfect sense for the electron density to be used to set up the system-specific Hamiltonian.

In 1964, the above hand-waving justification was put into concrete form by Hohenberg and Kohn [1].

3.6.1 The Hohenberg-Kohn Theorems

3.6.1.1 The First Hohenberg-Kohn Theorem

The First Hohenberg-Kohn Theorem (The proof of existence) states that:

> *The external potential $V_{ext}(r)$ is (to within a constant) a unique functional of the electron density $\rho(r)$; since, in turn $V_{ext}(r)$ fixes H we see that the full many particle ground state is a unique functional of $\rho(r)$.*

This theorem simply means that given an electron density, there cannot be more than one external potential, and hence the electron density uniquely determines the Hamiltonian operator and all the physical properties of an electronic system. The energy functional and Hohenberg-Kohn functional is given by Eqn. 13 and 14 respectively.

$$E_0[\rho_0] = \int \rho_0(\vec{r}) V_{Ne} d\vec{r} + F_{HK}[\rho_0] \qquad \text{Eqn. 13}$$

$$F_{HK}[\rho_0] = T[\rho] + E_{ee}[\rho] = \left\langle \Psi \middle| \hat{T} + \hat{V}_{ee} \middle| \Psi \right\rangle \qquad \text{Eqn. 14}$$

$E_{ee}[\rho]$ includes all the electron-electron interactions energies and $V_{Ne}[\rho]$ is the interaction between the electrons and external fields such as that due to the nuclei. The

Kohn-Sham approach for describing an explicit expression for $E_{ee}[\rho]$ is described later (see section 3.6.3).

In their indirect proof of this theorem, based on *argument by contradiction*, they started with the assumption that two external potentials, $V_{ext(1)}$ and $V_{ext(2)}$, differing by more than a constant, give rise to the same electron density associated with the corresponding non-degenerate ground states of some number, N, of particles. Two Hamiltonians can now be established, namely, $\hat{H}_1 = \hat{T} + \hat{V}_{ee} + \hat{V}_{ext(1)}$ and $\hat{H}_2 = \hat{T} + \hat{V}_{ee} + \hat{V}_{ext(2)}$. The two Hamiltonians, $\hat{H}_1$ and $\hat{H}_2$, give rise to two different ground state energies, $E_{0(1)}$ and $E_{0(2)}$, through two corresponding ground state wave functions Ψ_1 and Ψ_2, keeping in mind that these two ground state wave functions will now pointing to the same electron density. Invoking the variational principle, the following must be valid,

$$E_{0(1)} < \langle \Psi_2 | \hat{H}_1 | \Psi_2 \rangle = \langle \Psi_2 | \hat{H}_2 | \Psi_2 \rangle + \langle \Psi_2 | \hat{H}_1 - \hat{H}_2 | \Psi_2 \rangle \qquad \text{Eqn. 15}$$

Since $\hat{H}_1 - \hat{H}_2 = \hat{V}_{ext(1)} - \hat{V}_{ext(2)}$, Eqn. 15 becomes,

$$E_{0(1)} < E_{0(2)} + \langle \Psi_2 | \hat{V}_{ext(1)} - \hat{V}_{ext(2)} | \Psi_2 \rangle = E_{0(2)} + \int \rho(\vec{r}) \{ \hat{V}_{ext(1)} - \hat{V}_{ext(2)} \} d\vec{r} \qquad \text{Eqn 16}$$

Based on Eqn 14, the following must also be valid,

$$E_{0(2)} < E_{0(1)} - \int \rho(\vec{r}) \{ \hat{V}_{ext(1)} - \hat{V}_{ext(2)} \} d\vec{r} \qquad \text{Eqn. 17}$$

The summation of Eqn. 16 and Eqn. 17 yields a contradiction:

$$E_{0(1)} + E_{0(2)} < E_{0(2)} + E_{0(1)} \qquad \text{Eqn 18}$$

From the above, it can be concluded that the initial assumption of two external potentials, $V_{ext(1)}$ and $V_{ext(2)}$, differing by more than a constant, giving rise to the same electron

density associated with the corresponding non-degenerate ground states of some number, N, of particles is invalid.

3.6.1.2 The Second Hohenberg-Kohn Theorems

The Second Hohenberg-Kohn Theorems (The Variational Principle) states that:

> *For any trial density satisfying the necessary conditions (such as* $\rho(\vec{r}) \geq 0$, $\int \rho(\vec{r}) d\vec{r} = N$*), and which is associated with some external potential* V_{ext}*, the related energy functional will be higher than the true ground state energy.*

$$E_0 \leq E[\rho_{trial}] = T[\rho_{trial}] + E_{Ne}[\rho_{trial}] + E_{ee}[\rho_{trial}] \qquad \text{Eqn. 19}$$

E_0 results if and only if the exact ground state density is inserted into the equation $E_0[\rho_0] = \int \rho_0(\vec{r}) V_{Ne} d\vec{r} + F_{HK}[\rho_0]$

Given the understanding of above theorem, it is also important for us to note that they are limited to the ground-state of a particular geometry. Problems dealing with electronically excited states cannot be directly solved using the variational recipe.

To add on the above, there are other conditions which the densities will have to fulfill before they are eligible in the context of the Hohenberg-Kohn theorems. These conditions are the V-representability or the N-representability. V-representability refers to the condition whereby the electron density is associated with an antisymmetric wave function and a Hamiltonian operator with an external potential. However, it is not specified which conditions are essential for the densities to obey so that they are V-representable. On the other hand, the N-representability is the less stringent condition which only requires the density to arise from an antisymmetric wave function without enforcing a connection to an external potential. These two conditions stem from the

more in-depth theoretical aspect of density functional theory and shall not be described in further detail in this discussion.

Even before Hohenberg and Kohn came out with their theorems, two famous workers initiated the use of the electron density as the basic variable in the place of the wave function. The very first application of density functional theory dates back almost as far as quantum mechanics itself.

3.6.2 The Thomas-Fermi Model

Thomas and Fermi (1927) were the pioneers who attempted to use the electron density instead of the electron wavefunction to obtain information about atomic and molecular systems.

The kinetic energy based on the uniform electron gas model is given by the equation

$$T_{TF}\left[\rho\left(\vec{r}\right)\right] = \frac{3}{10}\left(3\pi^2\right)^{2/3}\int \rho^{5/3}\left(\vec{r}\right)d\vec{r} \qquad \text{Eqn. 20}$$

The Thomas-Fermi expression for the energy of an atom

$$E_{TF}\left[\rho\left(\vec{r}\right)\right] = \frac{3}{10}\left(3\pi^2\right)^{2/3}\int \rho^{5/3}\left(\vec{r}\right)d\vec{r} - Z\int \frac{\rho\left(\vec{r}\right)}{r}d\vec{r} + \frac{1}{2}\iint \frac{\rho\left(\vec{r}_1\right)\rho\left(\vec{r}_2\right)}{r_{12}}d\vec{r}_1 d\vec{r}_2$$

Eqn. 21

In the Thomas-Fermi model, the kinetic energy is in a simple functional form proportional to $\int \rho^{5/3}\left(\vec{r}\right)d\vec{r}$ and this does not appear to be sufficiently accurate. Even the elementary Hartree-Fock method which completely ignored electron correlation, gave better accuracy.

Although this theory is significant because it is the first example of a genuine density functional for the energy, the Thomas-Fermi model is far from accurate since the exchange and correlation effects had not been accounted for.

3.6.3 The Kohn-Sham Approach

In the follow-up work to the Hohenberg-Kohn theorems, Kohn and Sham [2] developed a strategy to resolve the problem related to the unknown Hohenberg-Kohn functional $F_{HK}[\rho_0]$ for electronic kinetic and potential energy. In appreciation of the fact that orbital-based approaches are a cut above the density-based recipe in determining the kinetic energy, Kohn and Sham made use of the Hartree-Fock concept of a non-interacting reference system. In essence, the Kohn-Sham approach evaluates the bulk of the kinetic energy to good accuracy with the use of the non-interacting reference system established from a set of orbitals. The remaining portion of the kinetic energy is combined with the non-classical contributions to the electron-electron repulsion into a very small part of the energy component. The latter component is then evaluated by the use of an approximate functional.

Bearing in mind, in the Hohenberg-Kohn theorems, the ground state energy of a molecular system can be found by searching through all acceptable densities and can be represented by the following expression.

$$E_0 = \min_{\rho \to N} \left(\int \rho(\vec{r}) V_{Ne} d\vec{r} + F_{HK}[\rho] \right) \qquad \text{Eqn. 22}$$

The first term in the expression represents the external potential and it describes the interaction between the electrons and the rest of the system. It is a system dependent term. On the other hand, the second term in the expression is universally valid in the

sense that its form is independent of the system. This second term, which is defined as the Hohenberg-Kohn functional, includes the kinetic energy and the electron-electron interactions. The latter in turn includes the Coulombic interactions, $J[\rho]$, between electrons and other non-classical contributions, $E_{ncl}[\rho]$, to the electron-electron interactions as discussed previously under Hartree and Hartree-Fock methods – all the effects of self-interaction correction and exchange and Coulomb correlation.

$$F_{HK}[\rho_0] = T[\rho] + E_{ee}[\rho] = T[\rho] + J[\rho] + E_{ncl}[\rho] \qquad \text{Eqn. 23}$$

If the explicit form of the terms in the Hohenberg-Kohn functional were known exactly, the entire density functional solution of the Schrödinger equation would have been complete without any approximation. The Thomas-Fermi and all related scheme was close to defining all the terms explicitly. However, it failed to describe the molecular system accurately due to its simplicity in the prescription of the expression for kinetic energy.

Kohn and Sham made use of the Hartree-Fock concept of a non-interacting reference system to establish a Hamiltonian which involves an effective local potential. They assumed a system of N non-interacting electrons to be moving in an effective potential and approximated the bulk of the kinetic energy as

$$T_S = -\frac{1}{2}\sum_i^N \langle \varphi_i | \nabla^2 | \varphi_i \rangle . \qquad \text{Eqn. 24}$$

The Hamiltonian for this hypothetical system can be expressed as follows

$$\hat{H}_S = -\frac{1}{2}\sum_i^N \nabla_i^2 + \sum_i^N V_S(\vec{r_i}) . \qquad \text{Eqn. 25}$$

The first term represents the kinetic energy and the second term represents the effective local potential. Since the Hamiltonian describes a system of non-interaction electrons, its

ground state wave function can be represented by a Slater determinant (that is not related to that in the Hartree-Fock method).

$$\Psi_0 \approx \Theta_S = \frac{1}{\sqrt{N!}} \det\left\{\varphi_1\left(\vec{x}_1\right)\varphi_2\left(\vec{x}_2\right)..\varphi_N\left(\vec{x}_N\right)\right\} \qquad \text{Eqn. 26}$$

where the spin orbitals are determined iteratively by a self-consistent field through the following set of pseudo-eigenvalue equations.

$$\hat{f}^{KS}\varphi_i = \varepsilon_i\varphi \qquad \text{Eqn. 27}$$

$\hat{f}^{KS}$ is the one-electron Kohn-Sham operator defined as $\hat{f}^{KS} = -\frac{1}{2}\nabla^2 + V_S(\vec{r})$.

This hypothetical non-interacting system is coupled to the real interacting system through an effective potential that results in a density that equates to the ground state density of the real system.

$$\rho_S(\vec{r}) = \sum_i^N \sum_S \left|\varphi_i(\vec{r},s)\right|^2 = \rho_0(\vec{r}) \qquad \text{Eqn. 28}$$

While the bulk of the kinetic energy is computed accurately via Eqn. 24, the residual part of the kinetic energy, T_C, is summed with the non-classical component of the electron-electron interactions, E_{ncl}, in a term called the exchange-correlation energy, E_{XC}.

Taking into consideration of Eqn. 24, Eqn. 23 therefore becomes,

$$F[\rho(\vec{r})] = T_S[\rho(\vec{r})] + J[\rho(\vec{r})] + E_{XC}[\rho(\vec{r})] \qquad \text{Eqn. 29}$$

and the exchange-correlation energy is defined as

$$E_{XC}[\rho(\vec{r})] \equiv (T[\rho(\vec{r})] - T_S[\rho(\vec{r})]) + (E_{ee}[\rho(\vec{r})] - J[\rho(\vec{r})]) = T_C[\rho(\vec{r})] + E_{ncl}[\rho(\vec{r})]$$

Eqn. 30

where $T_C[\rho(\vec{r})]$ is the contribution to the kinetic energy arising from electron correlation effects.

The resulting density functional like expression for the energy of the interacting, real system of interest becomes

$$E[\rho(\vec{r})] = T_S[\rho(\vec{r})] + J[\rho(\vec{r})] + E_{XC}[\rho(\vec{r})] + E_{Ne}[\rho(\vec{r})] \qquad \text{Eqn. 31}$$

where the explicit form of the individual terms are all defined as follows except for E_{XC}.

$$T_S[\rho(\vec{r})] = -\frac{1}{2}\sum_i^N \langle \varphi_i | \nabla^2 | \varphi_i \rangle \qquad \text{Eqn. 32}$$

$$J[\rho(\vec{r})] = \frac{1}{2}\int\int \frac{\rho(\vec{r}_1)\rho(\vec{r}_2)}{r_{12}} d\vec{r}_1 d\vec{r}_2 = \frac{1}{2}\sum_i^N \sum_j^N \int\int \left|\varphi_i(\vec{r}_1)\right|^2 \frac{1}{r_{12}} \left|\varphi_j(\vec{r}_2)\right|^2 d\vec{r}_1 d\vec{r}_2 \qquad \text{Eqn. 33}$$

$$E_{Ne}[\rho(\vec{r})] = \int V_{Ne}\rho(\vec{r}) d\vec{r} = -\sum_i^N \int \sum_A^M \frac{Z_A}{r_{1A}} \left|\varphi_i(\vec{r}_1)\right|^2 d\vec{r}_1 \qquad \text{Eqn. 34}$$

It is important to bear in mind that the density is related to the spin orbitals via Eqn. 28.

Also similar to that in the Hartree-Fock scheme, in the Kohn-Sham scheme, the Hohenberg-Kohn's second theorem, the Variational Principle applies. In the minimization of the energy as described by Eqn. 31, a set of one-electron pseudo-eigenvalue equations is established so that it can be resolved self-consistently to obtain the electronic potential used to construct the equations from the electron density of the occupied states.

3.6.3.1 Exchange and correlation energy

It is important to bear in mind that the Kohn-Sham scheme described above is almost a complete description of a molecular system in density functional form except for the fact that the explicit form of the exchange and correlation energy as a functional of ρ is not known but is defined as

$$E_{XC}[\rho(\vec{r})] = T_C[\rho(\vec{r})] + E_{ncl}[\rho(\vec{r})] \qquad \text{Eqn. 35}$$

Although these approximate or yet unknown exchange and correlation functionals are subjected to constraints, there is unfortunately no systematic way that this functional could be improved over an approximate one as is possible in the case of wave function based approaches.

The most commonly known forms of exchange and correlation functionals include the local density approximation (LDA) as well as the generalized gradient approximation (GGA). [3]

3.6.3.1.1 LDA

The local density approximation forms the basis for almost all approximate exchange correlation functionals. In this model, the assumption is that the exchange and correlation functional can be written simply as

$$E_{XC}^{LDA}[\rho] = \int \rho(\vec{r}) \varepsilon_{XC}(\rho(\vec{r})) d\vec{r} \qquad \text{Eqn. 36}$$

where $\varepsilon_{XC}(\rho(\vec{r}))$ represents the exchange-correlation energy per particle of a uniform electron gas of density $\rho(\vec{r})$. This model assumes that both the number of electrons N and volume of the electron gas V approaches infinity, while the electron density N/V=ρ attains a constant value everywhere just like the case in an ideal metal. However, this

situation hardly applies to the atoms and molecules that DFT calculations often aim to describe. Nevertheless, this approximation is an important one because it is the only form of exchange and correlation energy function known to a very high accuracy.

The exchange-correlation energy per particle of a uniform electron gas can be divided into two portions, the exchange contribution and the correlation contribution.

$$\varepsilon_{XC}(\rho(\vec{r})) = \varepsilon_X(\rho(\vec{r})) + \varepsilon_C(\rho(\vec{r})) \qquad \text{Eqn. 37}$$

The exchange contribution is equal to the Hartree-Fock exchange, originally proposed by Bolck and Dirac, multiplied by a pre-factor.

$$\varepsilon_X = -\frac{3}{4}\sqrt[3]{\frac{3\rho(\vec{r})}{\pi}} \qquad \text{Eqn. 38}$$

On the other hand, while the explicit form of the correlation part remains an unknown, there are various analytical expressions of ε_C proposed based on the numerical quantum Monte-Carlo simulation work by Ceperley and Alder, 1980. [4]

Often, approximate XC functionals are also expressed in the unrestricted version, where the two spin densities, $\rho_\alpha(\vec{r}), \rho_\beta(\vec{r})$, are used as the inputs instead of the electron density. It is important to note that $\rho_\alpha(\vec{r}) + \rho_\beta(\vec{r}) = \rho(\vec{r})$, hence the extension of LDA, the local spin-density approximation (LSD) can be presented in the following form,

$$E_{XC}^{LSD}[\rho_\alpha, \rho_\beta] = \int \rho(\vec{r})\varepsilon_{XC}(\rho_\alpha(\vec{r}), \rho_\beta(\vec{r}))d\vec{r} \qquad \text{Eqn. 39}$$

A measure of the degree of spin polarization is given by the spin polarization parameter,

$$\xi = \frac{\rho_\alpha(\vec{r}) - \rho_\beta(\vec{r})}{\rho(\vec{r})} \qquad \text{Eqn. 40}$$

Where $\xi = 0$ represents the spin compensated case and $\rho_\alpha(\vec{r}) = \rho_\beta(\vec{r})$, and $\xi = 1$ represents the fully spin polarized case in which all electrons have only one kind of spin.

The success of the LDA in describing equilibrium structures, harmonic frequencies or charge moments is counter-intuitive since its physical interpretation depends on the assumption that the exchange and correlation potential depends only on the local values of $\rho_\alpha(\vec{r})$ and $\rho_\beta(\vec{r})$ which barely resembles the systems that they aim to describe. On the other hand, it is well-known that this approximation gives rise to an over binding tendency i.e. it tends to overestimate atomization energies.

3.6.3.1.2 GGA

Where computational chemistry is concerned, the limitations of LDA and even the LSD render them insufficient to address most chemistry problems. An extension to the LDA was clearly needed and by the 80s there has been an attempt to treat the LDA as the first term of a Taylor expansion of the uniform density and extending the series with the next lowest term in the hope of getting a better approximation of the exchange-correlation functional. The Gradient Expansion Approximation (GEA) was obtained as follows,

$$E_{XC}^{GEA}[\rho_\alpha, \rho_\beta] = \int \rho(\vec{r}) \varepsilon_{XC}(\rho_\alpha(\vec{r}), \rho_\beta(\vec{r})) d\vec{r} + \sum_{\sigma,\sigma'} \int C_{XC}^{\sigma,\sigma'}(\rho_\alpha(\vec{r}), \rho_\beta(\vec{r})) \frac{\nabla\rho_\sigma(\vec{r})}{\rho_\sigma(\vec{r})^{2/3}} \frac{\nabla\rho_{\sigma'}(\vec{r})}{\rho_{\sigma'}(\vec{r})^{2/3}} d\vec{r} + \ldots$$

Eqn. 41

Contrary to expectations, the GEA performs worse than the LDA. It was realized later that this shortfall was because the exchange-correlation hole that arise from GEA have lost some of their physically meaningful properties as a result the expansion. By

conserving the essence of the physical properties, and manipulating the expansion, the Generalized Gradient Approximation is arrived at,

$$E_{XC}^{GGA}[\rho_\alpha, \rho_\beta] = \int f(\rho_\alpha(\vec{r}), \rho_\beta(\vec{r}), \nabla\rho_\alpha(\vec{r}), \nabla\rho_\beta(\vec{r}))d\vec{r} \qquad \text{Eqn. 42}$$

For practical purposes, the GGA exchange-correlation functional is usually split into its exchange and correlation contributions.

$$E_{XC}^{GGA} = E_X^{GGA} + E_C^{GGA} \qquad \text{Eqn. 43}$$

However, it should be noted that the actual form of these functionals does not necessarily reflect the physics behind them.

$$E_X^{GGA} = E_X^{LDA} - \sum_\sigma \int F(s_\sigma)\rho_\sigma^{4/3}(\vec{r})d\vec{r} \qquad \text{Eqn. 44}$$

$$s_\sigma(\vec{r}) = \frac{\left|\nabla\rho_\sigma(\vec{r})\right|}{\rho_\sigma^{4/3}(\vec{r})} \qquad \text{Eqn. 45}$$

where F is the reduced density gradient for spin σ and s_σ is the local inhomogeneity parameter.

Two main classes of the reduced density gradient have been put forth, the first depends on empirical parameters while the second is free of semiempirical parameters. The one developed by Becke, commonly abbreviated by superscript B or B88 [5], belongs to the first class of reduced density gradient.

$$F^B = \frac{\beta s_\sigma^2}{1 + 6\beta s_\sigma \sinh^{-1} s_\sigma}, \qquad \text{Eqn. 46}$$

where β is an empirical parameter.

An example of the second class of GGA exchange functional is the one developed by Perdew in 1986 [6]. It can be observed that this functional, unlike the previous example, is without any semiemprical parameter.

$$F^{P86} = \left(1 + 1.296\left(\frac{s_\sigma}{(24\pi^2)^{1/3}}\right)^2 + 14\left(\frac{s_\sigma}{(24\pi^2)^{1/3}}\right)^4 + 0.2\left(\frac{s_\sigma}{(24\pi^2)^{1/3}}\right)^6\right)^{1/15} \quad \text{Eqn. 47}$$

Other examples of the above type of functional include those put forth by Becke in 1986 (B86) [7], Lacks and Gordon in 1993 (LG) [8] and the more recent implementation by Perdew, Burke and Ernzerhof in 1996 (PBE) [9].

There are also myriad choices of correlation functionals available. However their forms are even more notoriously complicated compared to their exchange counterparts. While the P86 correlation functional is one of the most widely used choices, each exchange functional could in principle be used in combination with any other correlation functionals. Just to name a few common combinations, BP86, BLYP and BPW91 refers to the combination of Becke's exchange functional used in combination with Perdew's 1986 correlation functional, Lee-Yang-Parr [10] correlation functional and the Perdew-Wang 1991 [11] correlational functional respectively.

In general, GGA not only does improve the atomization energies [12-15] over that calculated by LDA, it also improves the total energies [12, 13], the energy barriers and the structural energy differences [16-19].

3.6.3.1.3 Perdew-Burke-Ernzerhof functional [9]

This is the functional used in all calculations mentioned in this work. This functional is an improved and simplified version of the PW91 [11] in which various problems exist. Specifically, the construction of the PBE functional is such that only the

energetically significant conditions are satisfied rather than satisfying as many exact conditions as possible as it is with the case of the PW91 functional.

$$E_C^{GGA}[\rho_\alpha, \rho_\beta] = \int d^3 r n[\in_C^{LSD}(r_s, \xi) + H(r_s, \xi, t)] \qquad \text{Eqn. 48}$$

where r_s is the local Seitz radius and $\rho = \frac{3}{4}\pi r_s^{\,3} = \frac{k_F^{\,3}}{3\pi^2}$, ξ is the relative spin polarization defined by $\frac{\rho_\alpha(\vec{r}) - \rho_\beta(\vec{r})}{\rho(\vec{r})}$ and t is a dimensionless density gradient with $t = \frac{|\nabla n|}{2\phi k_s n}$ [10]. Here, the spin scaling factor $\phi(\xi)$ is defined as $\phi(\xi) = \frac{(1+\xi)^{2/3} + (1-\xi)^{2/3}}{2}$ and the Thomas-Fermi screening wave number k_s is defined as $k_s = \sqrt{\frac{4k_F}{\pi a_0}}$ and $a_0 = \frac{\eta^2}{me^2}$.

In this scheme, the gradient contribution $H(r_s, \xi, t)$ was constructed from three conditions: firstly, to the limit of slow time variation as $t \to 0$, then to the limit of rapid time variation as $t \to \infty$, and finally to the limit of high-density under uniform scaling where the correlation energy scales to a constant [20].

On the other hand, the exchange energy was constructed from four other conditions: firstly, under the uniform density scaling described along with the third condition above, the exchange energy must have the following form,

$$E_X^{GGA}[\rho_\alpha, \rho_\beta] = \int d^3 r n \in_X^{LSD} (\rho) F_X(s) \qquad \text{Eqn. 49}$$

where $\in_X^{LSD} = -\frac{3e^2 k_F}{4\pi}$. Note that while $s = \frac{|\nabla n|}{2k_F n} = \sqrt{\frac{r_s}{a_0}}\frac{\phi t}{c}$ is another dimensionless density gradient with $c = \sqrt[3]{\frac{3\pi^2}{16}} \approx 1.2277$, $F_X(0) = 1$ will allow the recovery of the correct uniform gas limit.

Secondly, the spin-scaling relationship is obeyed by the exact exchange energy. Thirdly, under the condition of small density variations around the uniform density, the exchange energy must be able to recover the linear response demonstrated by the LSD. Finally, the Lieb-Oxford bound $E_X[\rho_\alpha, \rho_\beta] \geq E_{XC}[\rho_\alpha, \rho_\beta] \geq -1.679e^2 \int d^3 r n^{4/3}$ will be satisfied if the spin-polarized enhancement factor grows gradually with s to a maximum value less than or equal to 2.273, i.e., $F_X(s) \leq 1.804$.

The exact mathematical form of the above can be found in reference [9].

3.7 Implementation for surface calculations

3.7.1 Planewave basis set

In this section, we shall look at the essential elements of using planewaves in an electronic structure for periodic system.

A periodic system is one in which the unit cells are repeated *ad infinitum* on a Bravais lattis. Thus the effective potential, which can be a Kohn-Sham potential, in a crystalline solid is V(**r**):

$$\mathbf{V(r + R) = V(r)} \qquad \text{Eqn. 50}$$

Where **R** is any Bravais lattice vector.

For simplicity of notation, we use the one-dimensional case for this discussion since the three-dimensional case is merely a straightforward extension of this.

For an infinite system, the wavefunction can be expressed in terms of integrals of planewaves.

$$\Psi(x) = \int_{-\infty}^{\infty} c_k e^{ik.x}\, dk \qquad \text{Eqn. 51}$$

where all values of k are included in the integral since the planewaves $e^{ik.x}$ form a complete basis set. Considering a system consisting of a supercell with length L being periodically repeated, then

$$\Psi(x) = \sum_k c_k e^{ik.x} \qquad \text{Eqn. 52}$$

where the wavevector k can take on an infinite number given by:

$$k = \frac{2\pi}{L} n, n = 0,\pm 1,\pm 2,\pm 3.... \qquad \text{Eqn. 53}$$

The wavefunction $\Psi(x)$ is periodic with period L. Considering the effective potential in a piece of solid which is periodic with periodicity given by the lattic constant a

$$V(x) = \sum_G V_G e^{iG.x} \qquad \text{Eqn. 54}$$

where G represents the reciprocal lattice vectors. That is G is given by:

$$G = \frac{2\pi}{a} n, n = 0,\pm 1,\pm 2,\pm 3.... \qquad \text{Eqn. 55}$$

Taking the Kohn-Sham equation,

$$\left(-\frac{\eta^2}{2m}\frac{d^2}{dx^2} + V \right)\Psi_n = E_n \Psi_n \qquad \text{Eqn. 56}$$

where n labels the quantum states available, one can obtain the following equations:

$$\sum_k -\frac{\eta^2}{2m}\left(-k^2\right)c_k e^{ik.x} + \sum_G \sum_k V_G c_k e^{ik.x} e^{iG.x} = E_n \sum_k c_k e^{ik.x} \qquad \text{Eqn. 57}$$

Upon equating the coefficients of each planewave, we obtain:

$$\left(\frac{\eta^2}{2m}k^2 - E_n\right)c_k + \sum_G V_G c_{k+G} = 0 \qquad \text{Eqn. 58}$$

This is sometimes referred to as the central equation.

G can take on an infinite number of values. For each of these values of G, assuming that the value of k occurring in the first term of the central equation is $k = \frac{2\pi}{L}$, then the coefficients c_{k+G} are $c_{\frac{2\pi}{L}+0}, c_{\frac{2\pi}{L}\pm\frac{8\pi}{L}}, c_{\frac{2\pi}{L}\pm\frac{16\pi}{L}},...$

Since G represents the reciprocal lattice vectors, each planewave in the set of planewaves only interact with other planewaves in the same set:

$$e^{i(k+G).x}, G = 0, \pm\frac{2\pi}{a}, \pm\frac{4\pi}{a}, ... \qquad \text{Eqn. 59}$$

There are in all four distinct sets of planewaves labeled using the value of k in the first term of the central equation:

$$-\frac{\pi}{L} \le k \le \frac{\pi}{L} \qquad \text{Eqn. 60}$$

Note that these are all possible k values in the first Brillouin Zone.

A cutoff energy is chosen so that there are only a finite of equations for each value of k in the first Brillouin zone.

$$E_{cutoff} = \frac{\eta^2 k_{cutoff}^2}{2m} \qquad \text{Eqn. 61}$$

Due to the cutoff energy, there are now N_p planewaves left and thus N_p unknown c_k for each of the set of k. The determinant of the matrix of coefficients of c_k is set to zero

in order to obtain non-trivial solutions. Thus we are able to obtain N_p different values of E_n, each value being one eigenenergy for the system of equations and subsequently obtaining the wavefunctions. Upon solving each set of these equations, the wave function can be written as:

$$\Psi(x) = \sum_G c_{k-G} e^{i(k+G)x} = \left[\sum_G c_{k-G} e^{iG.x} \right] e^{ik.x} = U(x) e^{ik.x} \qquad \text{Eqn. 62}$$

where U(x) is periodic with the lattice constant a. This is known as Bloch's Theorem.

3.7.2 Pseudopotentials

By the use of Bloch's Theorem, a planewave energy cut-off in the Fourier expansion of the wavefunction and with careful k-point sampling, a good approximation to the Kohn-Sham equations for an infinite crystalline system can be found. However as a very large number of planewaves are usually required to accurately describe the rapid oscillating wavefunctions of electrons in the core region, it is not very efficient to expand the electronic wavefunction. Furthermore, the fitting of wavefunctions with Gaussian orbitals or plane waves is extremely difficult and small errors can create large differences in the core eigenvalue. A crucial property of the pseudo-wavefunction is that it can accurately describe different bonding configuration.

On the same note, when the full coulomb potential is considered in a calculation, the inaccuracy of the calculation becomes significant. That is because when the total energy of the system becomes extremely large, the small difference between clusters of similar size becomes similar in order to its error.

In the pseudopotential model, matter is treated as a sea of valence electrons moving in a background of ion cores. The cores are made up of the nuclei and the inert inner shell electrons. This approximate model is justified where chemistry is concerned

since the highly localized core wavefunctions cannot take part in the bonding of the atoms.The main advantage of this model is that the complexities of an all electron calculation can be avoided. The core electrons potential are simplified while only the valence electron potential is considered.

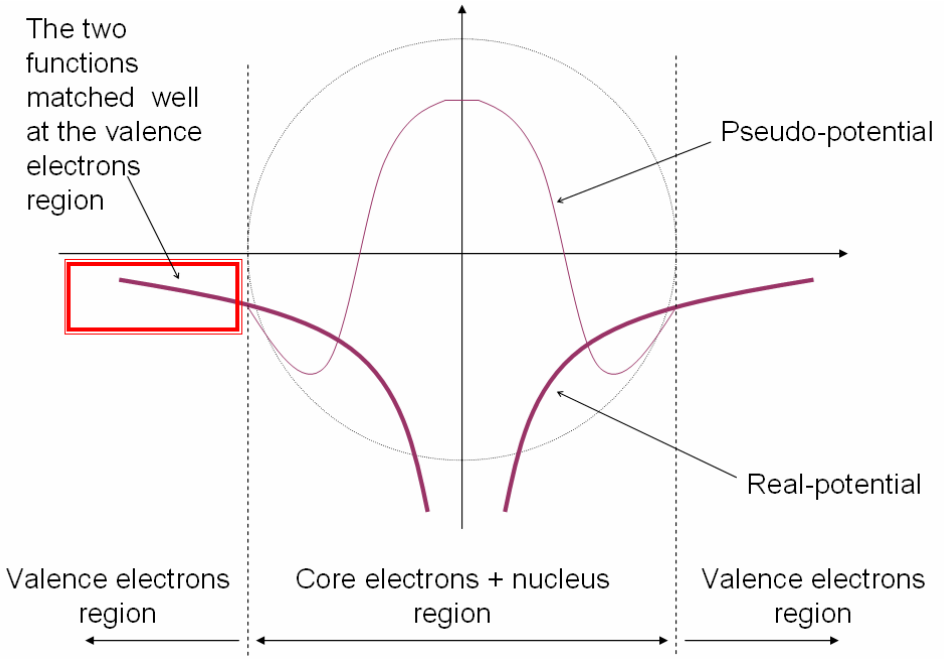

Figure 3.2: A simplified illustration of the pseudo-potentials. Thick curves represent the real potential of the electrons while the thin curve represents the pseudo-potential of the electrons. It is important to note that these curves are well matched at the valence electron region and thereby are useful when we are only concerned with the interactions of the valence electrons.

4 Calculation Details

Ab initio calculations using the slab model

4.1 Overview

This section of the thesis gives the technical details of the slab calculations used for the bulk of this work. These calculations were carried out using a DFT based ab initio total energy calculation program where the Si(100) surface was modeled using slabs that contained six layers of Si atoms. The top-most 5 layers were fully relaxed without any constraints while the bottom-most layer was fixed at bulk-like geometry. Dangling bonds at the bottom of the slab were terminated with hydrogen. Each slab was separated from the slab above and below by a vacuum separation of approximately 10Å. The slab is illustrated in figure 4.1 below.

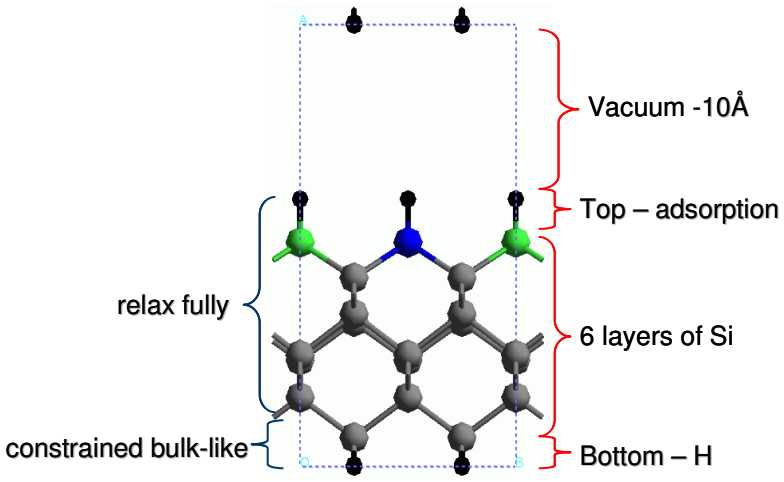

Figure 4.1: An illustration of the slab model that we used for our calculations

Our calculations were carried out using various types of supercells, namely, the 2 by 2, 2 by 4 and the 4 by 2 supercells as illustrated in figure 4.2 below. Since it is well

established that coupling between adjacent dimer rows is extremely weak, cells with only one dimer row were used for most of the calculations. It is only in cases where interactions across the dimer rows are important, such as the study of diffusion across the dimer row, that two dimer rows are considered.

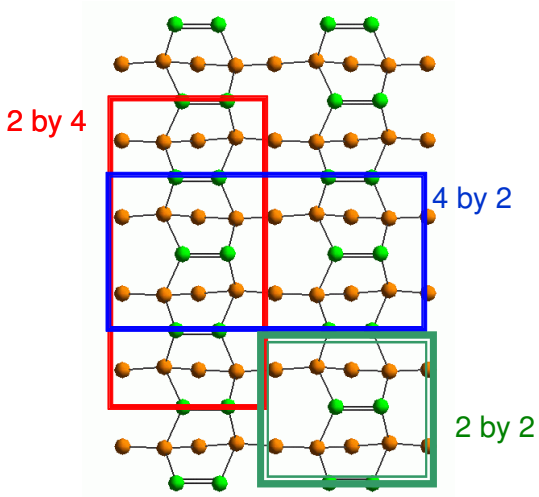

Figure 4.2: An illustration of the "2 by 2" supercell, "2 by 4" supercell and the "4 by 2" supercell used in this series of calculations

The ionic and electronic degrees of freedom are relaxed using a conjugate-gradient algorithm [1]. The electron exchange correlation was approximated with the generalized gradient approximation (GGA) functional by Perdew-Burke-Ernzehof [2]. The silicon ion cores are treated using completely separable norm-conserving nonlocal pseudopotentials in the Kleinman-Bylander form [3]. The hydrogen atoms were treated using the full 1/r potential. The cut-off radius for each of the s, p and d channels is 0.95Å.

The Kohn-Sham equations were solved using a plane wave basis set with a cut-off energy of 20 Ry and electronic states were sampled at 4-k-points, namely (0, ±1/4a, ±1/4b) for the 2×2 and 2-k-points, namely (0, 0, ±1/4b) for the 2×4 supercell and (0, ±1/4a, 0) for the 4×2 supercell. Where "a" is the length of the supercell in the direction along the dimer rows and "b" is the length of the supercell in the direction along the

dimer bond. The first direction is along the dimer bond, the second is along the dimer row and the third is perpendicular to the slab surface.

Our choices of cut-off energy for the planewaves, the number of k-points used for Brillouin zone sampling and the vacuum thickness were chosen based on an extensive study on the convergence, with respect to these quantities, of a very similar slab calculation by Ramstad *et. al*. [4] and is deemed accurate for the purpose of this study. Geometrical parameters for the clean surface and the paired-hydrogen are used to gauge the reliability of our calculations. The buckling angle and dimer bond length for the clean surface are 19.3^{o} and 2.35Å. For paired-hydrogen dimers, the dimer bond angle is zero and the dimer bond length is 2.41Å. The silicon-hydrogen bond length is 1.52Å.

4.2 Comparison between LDA and GGA

As a comparison study, we have carried out a series of LDA and GGA calculations on clean silicon slabs. By artificially forcing the silicon lattice spacing (a = 5.43Å) to take that of a germanium lattice (a = 5.66Å), we have progressively introduced a lattice strain of up to 4% deviation from the actual silicon lattice. With the lateral expansion of the slab there is an observed compression of the slab in the direction perpendicular to the surface.

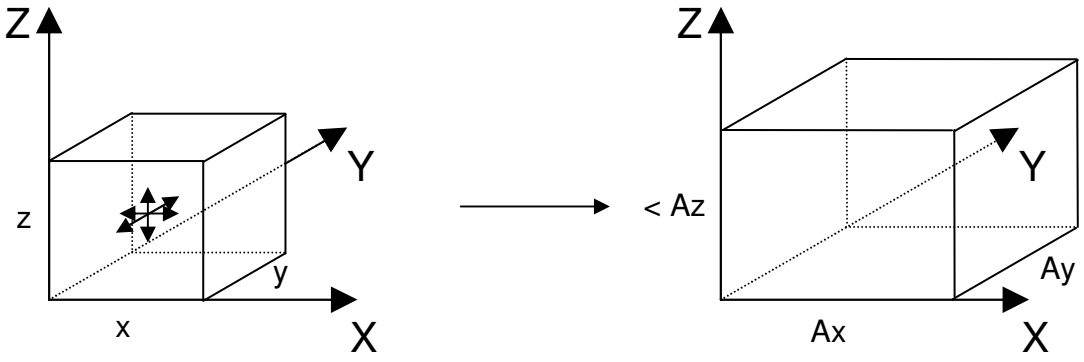

Figure 4.3: An illustration of how strain is modeled in our calculation. On the left of the figure is the unstrained slab. On the right of the figure is the strained slab. When a slab undergoes expansion in the x-y plane, there is an observed compression of the slab in the direction perpendicular to the x-y plane.
(Not drawn to scale).

The compression in the slab during straining is not simply the effect of conserving the volume of the material. In another words, there is a reduction in the density of the material as we introduce strain.

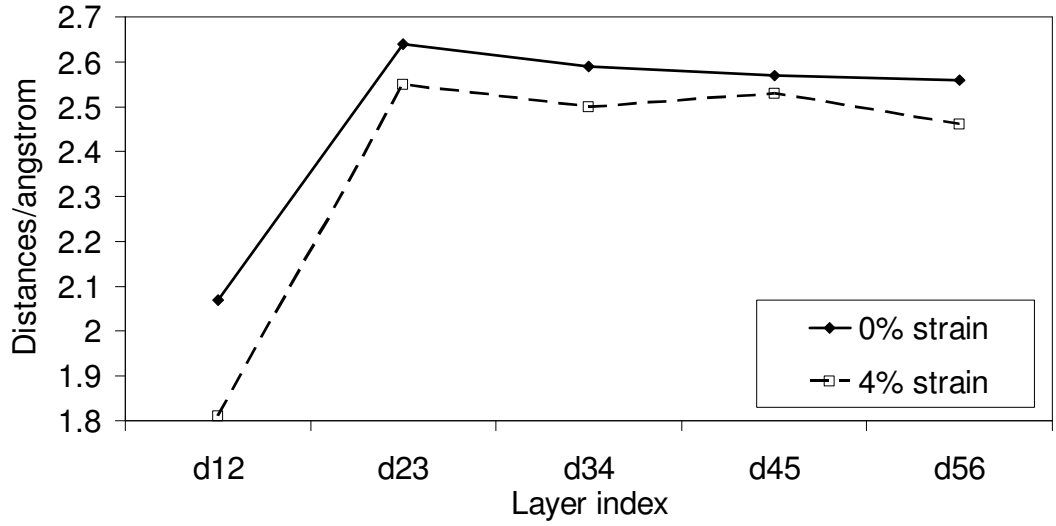

Figure 4.4: An illustration of slab compression due to strain. dxy refer to the distance between the xth layer and the (x+1)th layer. With layer 1 referring to the topmost surface layer. From our calculation, the average inter-layer distances of silicon decreased from 2.49Å for 0% strained slab to 2.37Å for the 4% strained slab.

Table 4.1: Comparison of our GGA & LDA calculations.

	GGA calculations	LDA calculations
Volume of 0% strained slab, $V_{0\%}$/Å^3	3003	2916
Volume of 4% strained slab, $V_{4\%}$/Å^3	3154	3021
Difference in volume, ($V_{4\%}$ - $V_{0\%}$)/Å^3	151	105
% difference in volume	5%	3.6%
Plane Strain	-0.0323	-0.0454

It is interesting to note here that while GGA is better for the calculation of reaction energies, it tends to overestimate the volume and underestimate the modulus. On the other hand, LDA tends to underestimate the volume and over estimate the bulk modulus.

Table 4.2: Comparison of our GGA calculated structure with literature values.

	Literature values	GGA calculated	Discrepancy %
Lattice constant	5.43 Å	5.45 Å	0.4 %
Bulk Si-Si distance	2.35 Å	2.36 Å	0.4 %
Dimer bond length	2.25 Å	2.346 Å	4 %
Dimer buckling	$20^o \pm 5^o$	19.3^o	3.5 %

Our calculated clean surface structures of Si(100) are in good agreement with that routinely reported in literature. That is a good starting point for our study of surface processes.

5 Decomposition of SiH_3 to SiH_2 on Si(100)-(2×1)

In this chapter, the decomposition energetics of the silyl group into silylene and hydrogen on the Si(100)-(2×1) surface was studied using pseudopotential density functional calculations. The results provided insight on the relative stability of the adsorption configurations of silylene in the presence of different coverages of co-adsorbed hydrogen. We find that the prevalence of the intra-row silylene on the growth surface is a result of both thermodynamics and kinetics. Our results also suggest that both the silylene group and the hydrogen atom formed by silyl decomposition acquire frustrated translational energy in the exit valley of the decomposition pathway. In particular, the hydrogen atom is approximately 0.5 eV more energetic than the thermal energy. This is consistent with observations made in STM images that show the dissociating hydrogen atom migrating away from the decomposition site.

5.1 Introduction

Silicon is an important material in the semiconductor industry because of the well-established CMOS technology. Although trends are slowly moving towards developing new materials for devices, a better understanding of the silicon growth process will also help to shed light upon the growth process of other related material such as silicon-germanium and strained silicon. Silane and disilane are common gas source precursors used in the GSMBE of silicon [1]. Investigations of the decomposition of these gas source precursors leading to the growth of epitatic Si layers are therefore required for further advances.

The first step in this decomposition involves the formation of the silyl group. Its subsequent decomposition to the silylene group has been investigated by a number of groups. The equilibrium adsorption sites of the silylene are now rather well established [2-7]. Without adsorbed hydrogen atoms in the vicinity of the silylene group, the most favorable adsorption configuration is the on-dimer structure with the silylene adsorbed onto a surface dimer leaving the surface dimer σ-bond intact. With hydrogen atoms coadsorbed in the vicinity of the silylene the more stable configuration is the intra-row structure with the silylene adsorbed on one side of the dimer row between two neighboring dimers. Two other structures that have also been considered are the in-dimer structure and the inter-row structure. The former is similar to the on-dimer structure except that the σ-bond of the dimer is broken. The latter consists of a silylene group adsorbed between two dimers on neighboring dimer rows. These adsorption configurations are illustrated in Figure 5.1 below.

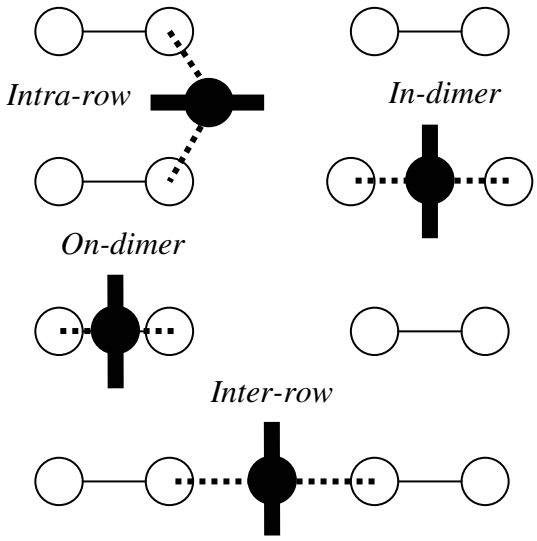

Figure 5.1: An illustration of possible adsorption sites of the silylene group. Black circles in indicate the silicon atom of the silylene group. Thick lines indicate the two hydrogen atoms of the silylene group. Empty circles indicate the silicon atoms of the dimer. Dashed lines indicate the bonds between silylene and surface silicon atoms. The difference between the on-dimer and the in-dimer configuration is that in the former, only the π bond of the dimer is broken while in the latter, both the σ bond and the π bond of the dimer are broken to accommodate the silylene insertion.

The energetics of these silylene configurations have been well studied by theoretical methods. Earlier density functional theory (DFT) calculations have shown that the inter-row configuration and in-dimer configuration have energies that are higher than the intra-row configuration and the on-dimer configuration [2]. Thus, much of the later theoretical work was focused on resolving the energy difference between the latter two configurations. On the clean surface, all the calculations reported in the literature indicate that the on-dimer configuration is at least as stable as, if not more stable than, the intra-row configuration [2-5]. However, the on-dimer configuration is not experimentally observed even at room temperature and (silane or disilane or SiH2 or H) total coverages of silylene and hydrogen below 0.1 [6, 7]. Bowler and Goringe [2] argued against the on-

dimer configuration based on the strong repulsive lateral interaction calculated for two such groups on nearest-neighbor dimers along a dimer row. Their calculations, on the other hand, showed no strong repulsive interactions for two intra-row groups. However, the effects of lateral interactions are expected to be small for sufficiently low coverages. An additional factor that is important is the presence of co-adsorbed hydrogen. Since decomposition of the silyl group leads to adsorbed hydrogen, it makes sense to study the relative stabilities of these in the silylene configurations with one or more co-adsorbed hydrogen atoms in the vicinity. More recent calculations revealed that in the presence of co-adsorbed hydrogen, the trends of the relative stabilities of the two configurations are reversed [3-5].

Although the adsorption sites are well established, the decomposition pathway from silyl to silylene is still not resolved. Surface analysis techniques such as secondary-ion-mass spectroscopy (SIMS), temperature-programmed desorption (TPD) and low-energy electron diffraction (LEED) have been used by Gates *et al.* to study the decomposition mechanism of SiH_x species on the Si(100)-(1×2) surface [8-11]. This work, as well as many others [6, 7, 12-18], shows that the silyl group produced by the decomposition of silane and disilane is metastable and has an average life-time on the order of a few minutes at room temperature [6]. Scanning tunneling microscopy (STM) studies also show that the silylene group resulting from silyl decomposition remains stable below 470K [19]. Silylene is therefore believed to be the predominant species occurring on Si(100)-(1×2) during growth by GSMBE. The adsorbed silyl group interacts with two dangling bonds on the surface to give rise to a silylene group and a hydrogen atom, the decomposition rate depending upon the dangling bond coverage in the vicinity.

From temperature-programmed SIMS data and using the analysis in Refs. 20 and 21 the activation barrier for silyl decomposition can range from 0.08 eV at saturation silane dosage to 0.1 eV at low silane dosage. The corresponding pre-exponential factors are rather low at 0.7 s^{-1} and 4 s^{-1}, respectively. These results led Gates, *et. al* to conclude that the decomposition rate is limited by the availability of dangling bonds on the surface.

Two theoretical studies have calculated the activation barrier of silyl decomposition process. DFT calculations using cluster models [22] find a low barrier of 0.25 eV when the process is assisted by atomic hydrogen leading to an in-dimer structure (but a rather higher barrier of 1.43 eV without hydrogen-abstraction assistance). However, the hydrogen-abstraction assisted process proposed in Ref. 16 does not involve the participation of dangling bonds, and is thus inconsistent with the experimental data that established a dependence upon the dangling bond coverage. The activation barrier of 0.25 eV is relative to a reactant state that includes a hydrogen atom in the gas phase. In the transition state, the dimer bond is broken (ring-opening) but the activation barrier is not large because the transition state includes a gas phase hydrogen molecule formed from the reactant hydrogen atom. In addition, there are a couple of points that should be noted here. It has been shown in earlier calculations [2] using slab models of the surface that the in-dimer structure resulting from the proposed hydrogen-abstraction assisted process is less stable than the intra-row structure by about 0.2 eV [2]. Furthermore, the cluster models used in Ref. 16 have only one dimer along each dimer row and thus are not able to probe the intra-row model at all. Even though the activation barrier found is low and is somewhat in agreement with the experimental data in Ref 8-11, the pathway identified seems problematic.

A more recent DFT slab calculation modeled within a generalized gradient approximation (GGA) by Smardon and Srivastava [23], discusses the decomposition of silane and disilane and the subsequent decomposition of the resulting silyl species. They reported a barrier of 2 and 2.5 eV for the low hydrogen ambience decomposition pathway of silyl decomposition to the intra-row and on-dimer respectively. While there is an apparent preference for the intra-row pathway under low hydrogen ambience, the preference is reversed in the case where fragmented hydrogen is present with a 1.0 eV difference in the decomposition barrier. This is despite the intra-row configuration being 0.1 eV more energetically stable than the on-dimer configuration.

There is also experimental evidence for silyl decomposition leading to the intra-row structure from STM at low disilane coverage [6-7]. In the sequential images of Si(100)-(1×2) the adsorption of the silyl group and its subsequent dissociation reaction into intra-row silylene and hydrogen have been observed. However, this is not a conclusive evidence for a pathway leading directly from adsorbed silyl to the intra-row configuration as the latter can also be formed from the relaxation of the silylene group from a higher energy configuration after the decomposition process. Subsequently, data from various other groups also supported the decomposition of the silyl group into the intra-row site through different experimental means. The absence of a symmetry axis perpendicular to the surface as indicated by multiple internal reflection infrared spectroscopy (MIRIS) polarized radiation measurements [18] points to the fact that vibration is tilted, consistent with the intra-row configuration. With a combination of MIRIS and density functional theory cluster calculations, it has also been shown that the

calculated stretching frequencies of the intra-row configuration are in good agreement with the experimentally observed modes.

In this section of the thesis, we present density functional slab calculations of the silyl group decomposition pathways leading to on-dimer and intra-row silylene structures. Comparison of calculated energetics of the silylene configurations on a clean Si surface or with one or more co-adsorbed hydrogen atoms in the vicinity will be useful in providing insight into the molecular pathways for the silyl decomposition. Thus far, the GGA has been used in one previous study [23]. Our calculations could also serve as useful comparisons with previous calculations using the LDA [2-5]. We find that the resulting intra-row silylene on the growth surface is a result of both favorable thermodynamics and favorable kinetics.

5.2 Results and discussion

We first discuss the structure and energetics of the intra-row and on-dimer adsorption states for silylene. Then we present results for the decomposition paths to get from the silyl group to each of these silylene adsorption states. Figures 5.2 and 5.3 illustrate the structures of interest for the intra-row configuration and the on-dimer configuration, respectively, with different numbers of co-adsorbed hydrogen atoms. Some bond lengths and bond angles are summarized in Table 5.1.

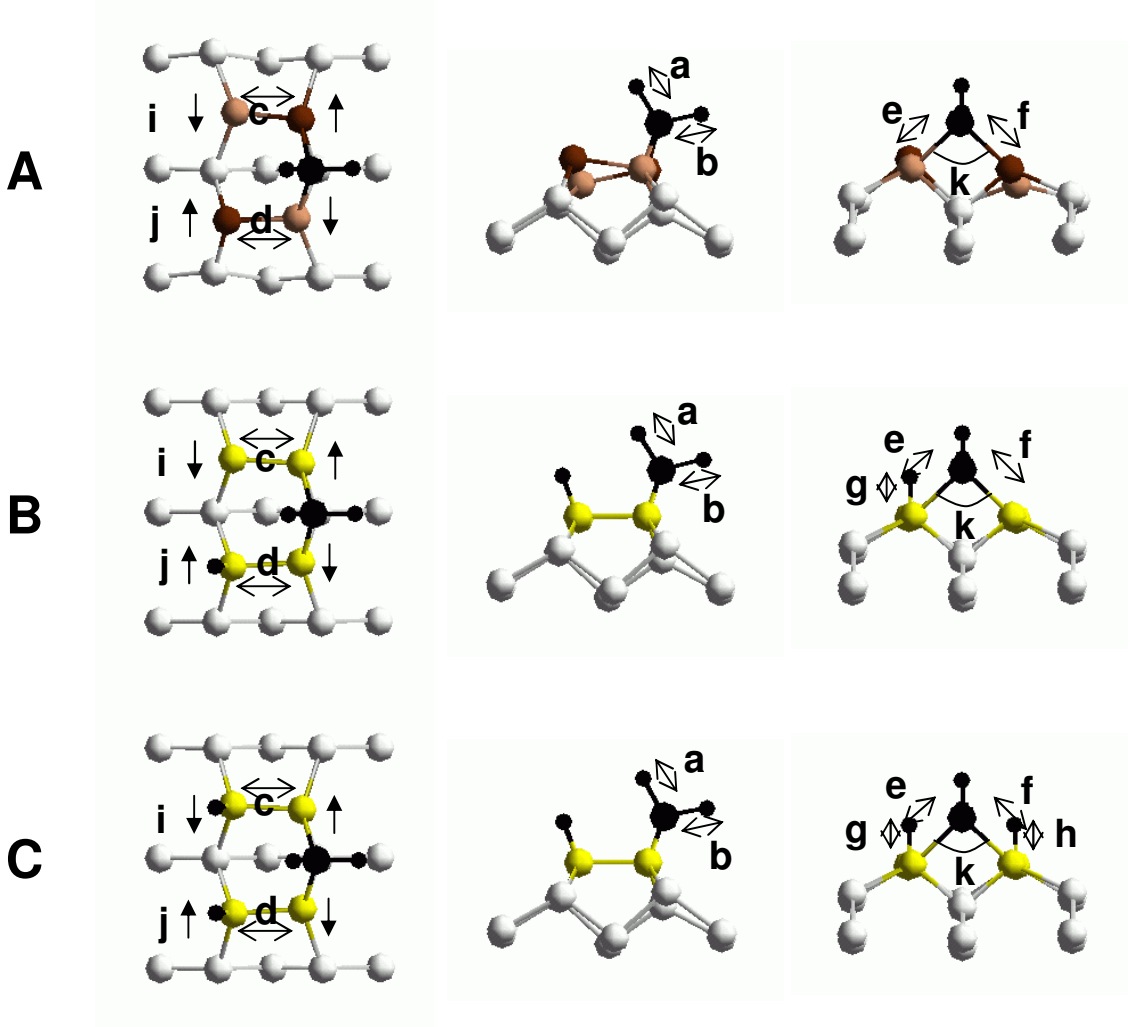

Figure 5.2: An illustration of the silylene group adsorbed in the intra-row configuration without any neighbouring hydrogen atom (structure A), with one co-adsorbed hydrogen atom (structure B) and with two co-adsorbed hydrogen atoms (structure C). The labels a to k indicate the lengths and angles given in Table 5.1. Buckled up atom on the dimer (dark brown); buckled down atom on the dimer (light brown); un-buckled dimer (yellow).

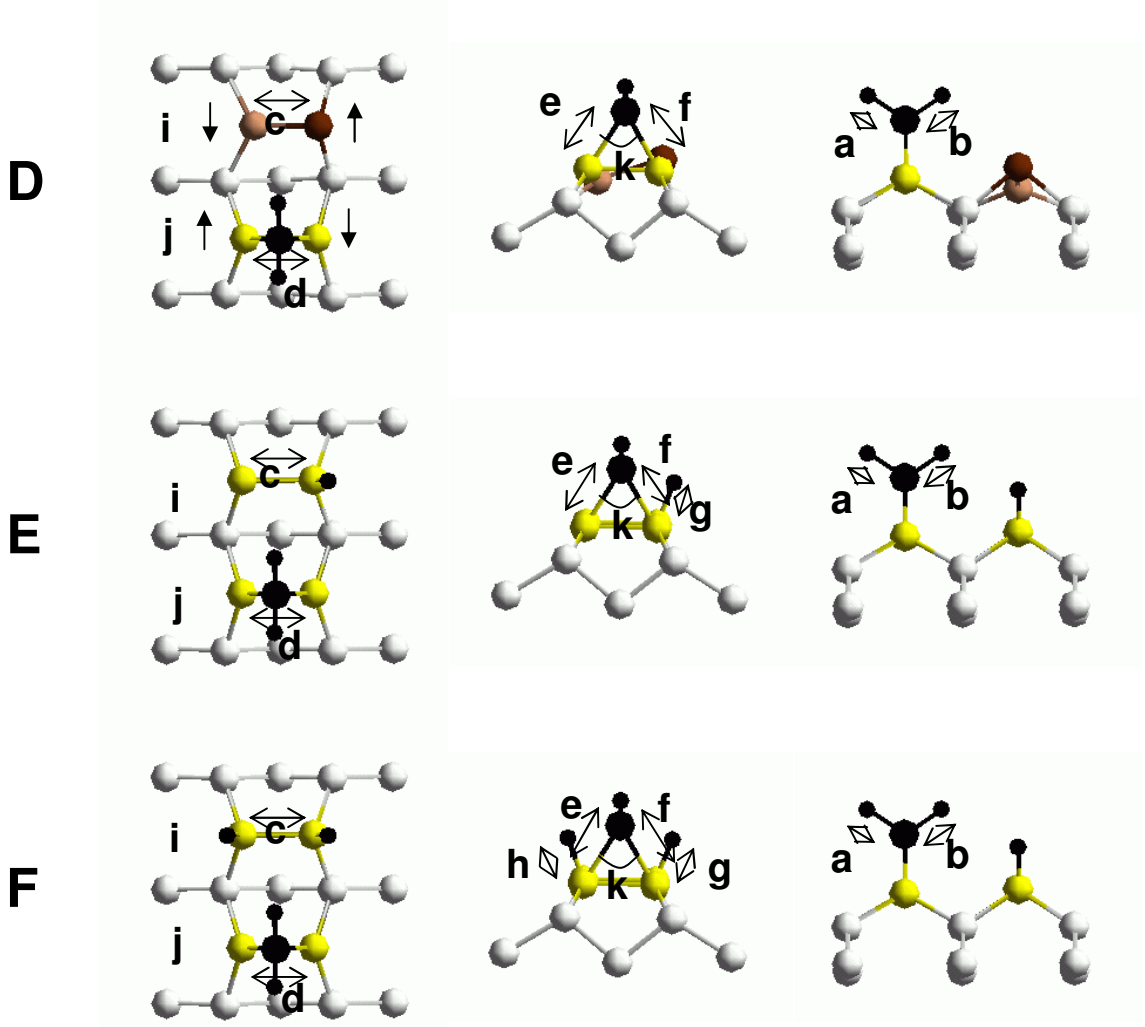

Figure 5.3: An illustration of the silylene group adsorbed in the on-dimer configuration without any neighbouring hydrogen atom (structure D), with one co-adsorbed hydrogen atom (structure E) and with two co-adsorbed hydrogen atoms (structure F). The bond lengths and angles of optimized structures denoted by a to k are given in Table 5.1. Buckled up atom on the dimer (dark brown); buckled down atom on the dimer (light brown); un-buckled dimer (yellow).

Table 5.1: Bond lengths and bond angles for the intra-row and the on-dimer configurations illustrated in Figs. 5.2 and 5.3. Lengths a – h are in angstroms, angles i - j are in degrees.

	A	**B**	**C**	**D**	**E**	**F**
a	1.523	1.523	1.524	1.514	1.515	1.516
b	1.522	1.521	1.522	1.514	1.515	1.516
c	2.376	2.388	2.410	2.321	2.403	2.412
d	2.442	2.406	2.410	2.421	2.445	2.434
e	2.411	2.423	2.427	2.329	2.331	2.334
f	2.433	2.423	2.426	2.336	2.329	2.333
g	-	1.523	1.524	-	1.522	1.523
h	-	-	1.524	-	-	1.523
i	14.3	4.9	3.8	18.5	0.5	0.0
j	7.3	3.5	3.7	1.0	0.4	0.1
k	91.6	91.1	91.0	62.7	63.3	62.9

Adsorption onto the dimer weakens the dimer bond. This can be seen in the increase in the dimer bond lengths after adsorption. From our calculations, the clean dimer bond length is 2.35 Å, while the dimer bond length for the on-dimer structure is 2.42, 2.45 and 2.43 Å with zero, one and two hydrogen atoms adsorbed on the neighboring dimer. For the intrarow configuration, the dimer bond lengths for the adsorbing dimer-pair are 2.38 and 2.44 Å when no hydrogen atoms are coadsorbed on the dimer-pair (structure A). Both dimers are buckled. When the dimer-pair is coadsorbed with hydrogen atoms, the bond lengths are both 2.41 Å and there is no buckling. Thus, as expected, in both the on-dimer and the intrarow configurations, adsorption weakens the dimer bond significantly. This is readily rationalized in terms of the weakening of the π-

bond when adsorption occurs. Adsorption at the on-dimer site leaves no extra dangling bonds behind while adsorption at the intra-row site leaves two dangling bonds at the other end of the dimer-pair leading respectively to the formation of a three-member and a four-member ring structure. When there is no neighboring hydrogen coadsorption the adsorbed dimers are buckled for adsorption at both intra-row and on-dimer sites. However, the buckling angles are smaller than those for the clean surface. The angle (~60º for on-dimer and ~90º for intra-row) between the two silylene-surface bonds is rather different from the tetrahedral angle thus suggesting that these ring structures are probably highly strained structures. Indeed the on-dimer structure was ruled out by early work on the basis of the small bond angle [7]. It is interesting to note that the adsorption of an on-dimer silylene group on a dimer leaves the adjacent clean dimer slightly shortened. Table 5.2 is a summary of adsorption energetics including results obtained in previous calculations. We will briefly discuss the relative stabilities of the silyl decomposition products before we look at the activation energies for silyl decomposition. Our results are in good agreement with what have been previously reported in the literature [2-5, 23].

Table 5.2: A summary of the methods previously used and the relative adsorption energetics of the on-dimer and intra-row configuration on clean and co-adsorbed silicon surfaces

	Ref. [2]	**Ref. [3]**	**Ref. [4]**	**Ref. [5]**	**Ref. [23]**	**Our work**	**Our work**	**Our work**
Slab Thickness	5 layers Si	6 layers Si	8 layers Si	5 layers Si	8 layers Si	6 layers Si	6 layers Si	6 layers Si
Method	DFT/ LDA	DFT/ LDA	DFT/ LDA	DFT/ LDA	DFT/ GGA	DFT/ GGA	DFT/ GGA	DFT/ GGA
E_{cut}/Ryd	14.7	10	8	10	10	20	20	20
Supercell size	2×2	p(√8×√8) R45^o	2×2	4×4	2×2	2×2	2×2	2×4
# k-points	†N.R.	2	3	1	4	1	4	2
***ΔE (SiH_2)**	0.004	-0.14	-0.10	-0.26	…	-0.04	-0.04	-0.18
***ΔE (SiH_2+ H)**	…	0.13	0.15	…	…	0.05	0.13	0.15
***ΔE (SiH_2 + 2H)**	…	0.11	-0.08	0.11	0.1	0.09	0.15	…

***ΔE = E(on-dimer) - E(intra-row)**

†Not Reported

In the present study, two different supercell sizes are used. The 2×2 supercell consists of two dimers in a single dimer row. Thus, a calculation of the intra-row structure using this supercell inevitably includes the interaction between an intra-row

silylene and the next intra-row silylene adsorbed on the next dimer pair along the same dimer. The 2×4 supercell consists of four dimers along a single dimer row. Here the lateral interaction is less than that present in the 2×2 supercell since the silylene groups are separated by two dimers from its nearest-neighbor along the dimer row. The same considerations apply for the on-dimer configuration. Without hydrogen co-adsorption, our calculations with the 2×2 supercell show a small energy difference $\Delta E = E_A - E_D$ of 0.04 eV between the less stable intra-row (structure A) and the more stable on-dimer (structure D) configurations. The relative stability is in agreement with most previous calculations [3-54] although these calculations show a significantly larger energy difference. Çakmak and Srivastava [4], using a 2×2 supercell found $\Delta E = 0.10$ eV with a local density approximation, while the earlier calculations [2] also using a 2×2 supercell found an energy difference of 0.004 eV. Our 2×2 supercell results are probably more in agreement with the conclusion that the energy difference between these two structures is small [2]. However, with the 4×2 supercell where the energetics are less likely to be affected by lateral interactions, a larger energy difference of 0.18 eV is observed. This compares reasonably well with Hong [3] and Takeuchi [5] who found $\Delta E = 0.14$ eV and 0.26 eV, respectively, using the local density approximation. Our results show that a sufficiently large supercell size is required to obtain an accurate comparison for these structures. Considering the change in the buckling of the dimers as a result of adsorption, lattice effects probably contribute quite significantly to this lateral interaction. A comparison of the results of previous LDA calculations from two different groups [4, 5], one with a 2×2, and the other with a 4×4 supercell, suggests the same conclusion that supercell size does affect the accuracy of the results. The on-dimer configuration was

found to be more stable by 0.10 eV and 0.26 eV, respectively. The relative stability of the on-dimer configuration can be understood from the analysis of the configurations. As mentioned in section A, the adsorption at the on-dimer site leaves no extra dangling bonds behind while adsorption at the intra-row site leaves two dangling bonds at the other end of the dimer-pair. These additional dangling bonds are believed to give rise to the energy difference. We note that the LDA energy difference is larger than our GGA result.

On the clean surface, the on-dimer configuration is energetically more favorable than the intra-row configuration. However, in the presence of co-adsorbed hydrogen, our calculations show that the intra-row configuration (Figure 5.2, structure C) is now more stable than the on-dimer configuration (Figure 5.3, structure F). This reversal in relative stabilities of the on-dimer and the intra-row configurations can be attributed to the saturation of the additional dangling bonds formed by the intra-row configuration when hydrogen is co-adsorbed. With the saturation of the dangling bonds, the strain induced in the three or four-membered ring structures becomes the deciding factor for relative stabilities. This result is consistent with all but one previously reported calculation. The hydrogen co-adsorption calculation performed by Çakmak and Srivastava [4] predicted the opposite relative stability. Their calculation uses a small (2×2) supercell along with the local density approximation and from our discussion above, the (2×2) supercell calculation is probably affected by lateral interactions. Thus a sufficiently large supercell size is required to obtain an accurate comparison for these structures.

The greater stability of the intra-row structure implies that decomposition leads to the intra-row configuration since at least one hydrogen atom would be co-adsorbed in the vicinity of the silylene group immediately after it is formed. As suggested in the STM

study by Bronikowski *et. al.* [7], hydrogen can subsequently diffuse away, leaving silylene adsorbed in the intra-row configuration. This will be discussed further towards the end of this chapter.

The calculations of the activation barrier, for silyl decomposition into the silylene and hydrogen, provided evidence that the formation of the on-dimer configuration, other than being thermodynamically unfavorable, is also kinetically hindered. In order to trace the decomposition paths, optimized geometries were obtained for a number of structures in each of which the distance $d_{Si\text{-}H}$ between the silyl silicon atom and its dissociating hydrogen atom is held fixed at different values. A total of 21 (26) different structures were computed for the path leading to the intra-row (on-dimer) configuration. The positions of the silyl silicon atom and the dissociating hydrogen atom in the plane of the surface are plotted in Figure 5.4 for both intra-row (a) and on-dimer paths (b), with the transition state for each indicated.

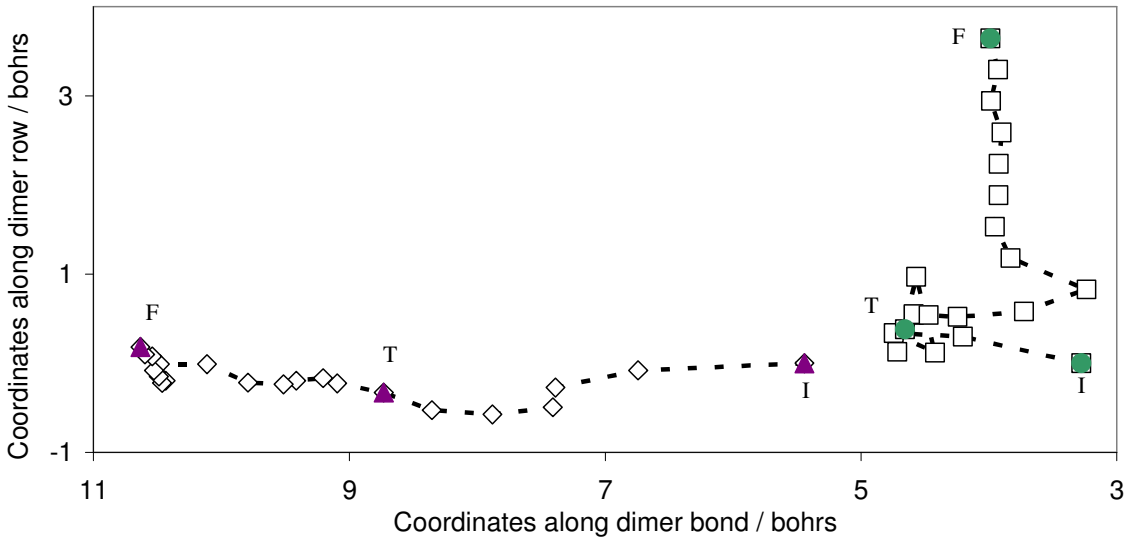

(a)

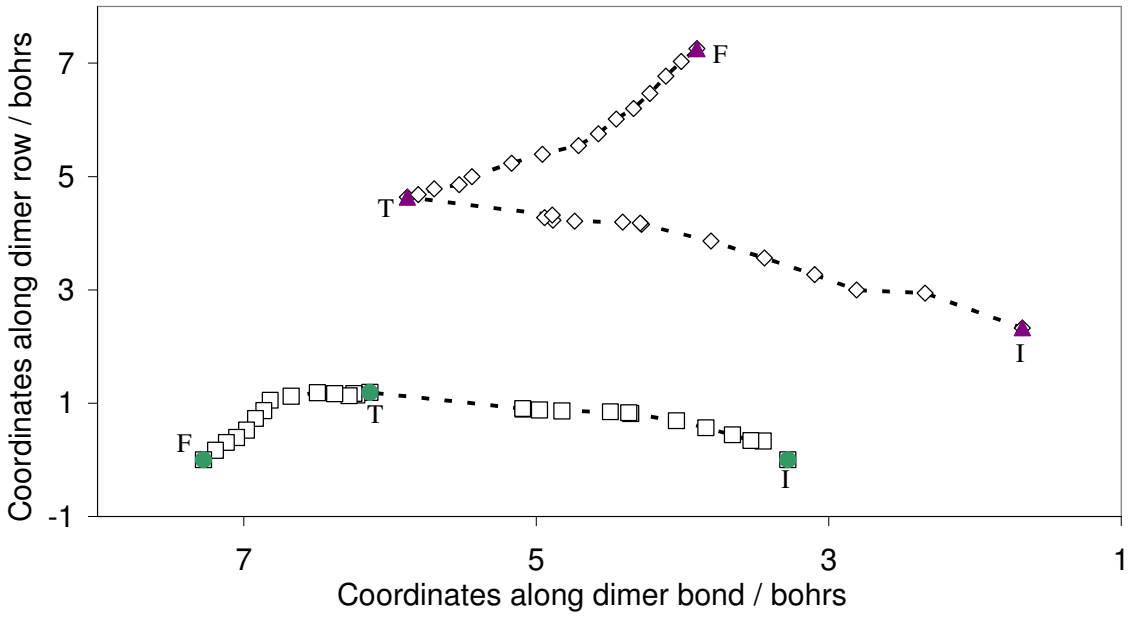

(b)

Figure 5.4: The positions of the silyl group (□) and the hydrogen atom (◊) along the decomposition path to a) the intra-row configuration, and b) the on-dimer configuration. The initial, transition and final states are denoted by I, T and F, respectively.

The results for energetics are summarized in Figure 5.5 where the energy for each structure along the path is plotted. The same data is plotted in Figure 5.6 to show the dependence upon d_{Si-H}. The activation barrier for the silyl group to decompose to the intra-row silylene is found to be 1.12 eV and that to decompose to the on-dimer silylene is found to be 1.34 eV.

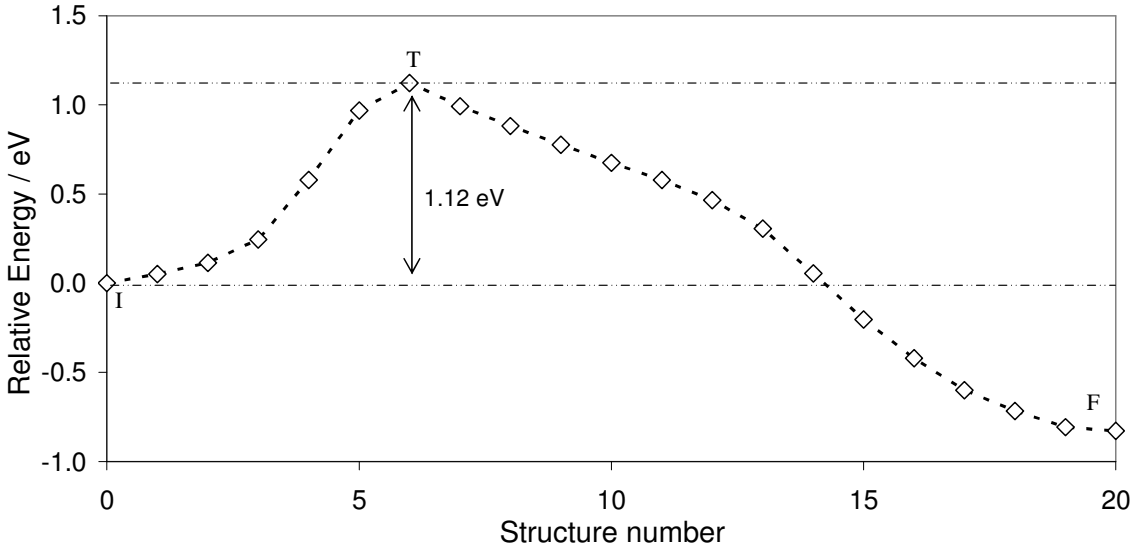

(a)

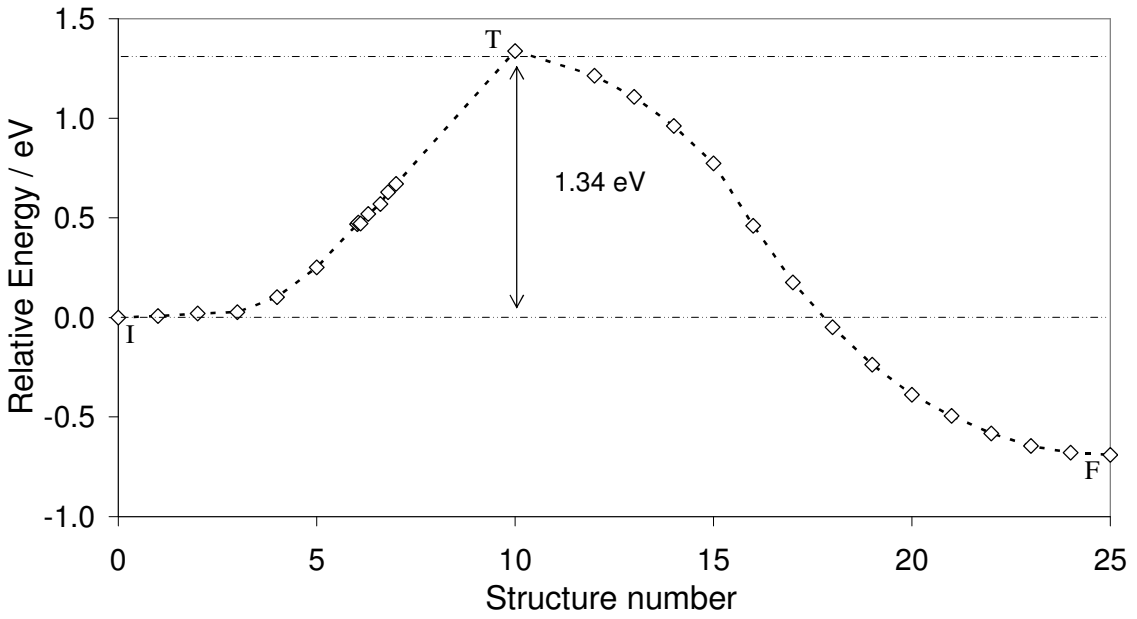

(b)

Figure 5.5: Plots of energy versus structure number for (a) the intra-row path and (b) the on-dimer path. For both paths, structure number "0" corresponds to the initial structure. The initial, transition and final states are denoted by I, T and F, respectively.

The decomposition barrier of the silyl group has also been studied [22] with cluster models of the silicon surface, which use more reliable methods of locating the

transition point than the reaction path tracing that was used in this work. In Ref. 22, the decomposition barrier of a silyl group into a silylene group and a hydrogen atom adsorbed on the same dimer are calculated to be approximately 1.12 eV using a three-dimer trench cluster. This cluster model of the surface consists of three adjacent dimers in the direction perpendicular to the dimer row. The reaction path includes an intermediate state with a hydrogen atom and a silylene group adsorbed on a dimer. The latter forms an on-dimer structure through a dimer-breaking and ring-formation process that has a barrier of 1.12 eV. Our slab calculations, however, show that the intermediate structure in these cluster calculations is actually unstable (as opposed to being metastable) if there is an adjacent dimer in the direction of the dimer row; the silylene group bonds to the silicon atom in the adjacent dimer (along the dimer row) to form the intra-row structure. In the cluster model used, this instability is not observed, probably because the model consists of only one dimer in the dimer row. Thus, cluster model size is particularly important here. Indeed, both the reaction paths we investigate in this chapter probably require at least a four-dimer trench cluster model with two dimers to model each of two adjacent dimer rows. To the best of our knowledge, there are currently no cluster calculations with models that are sufficiently large to probe the reaction paths we study here.

It is quite clear from the results in Figs. 5.4 and 5.5 that the reaction coordinate is not simply the silicon-hydrogen distance $d_{Si\text{-}H}$. In particular, a graphical illustration of this is seen in Figure 5.7 where the structures of the silyl group (a), the transition state (b) and silylene (c) are compared for the intra-row path. In the transition state the hydrogen atom is already quite close to its final position in the decomposition process. However, the position of the silylene group is still quite far from its final position in the process.

That is, the entry "valley" of the decomposition path is mainly defined by the dissociation of the hydrogen atom from the silyl silicon, whereas the exit "valley" is mainly defined by the formation of the bond between the silylene group and the silicon atom on the neighboring dimer. This will be further discussed below in relation to an estimate of the vibrational energies imparted to the hydrogen atom and the silylene group as a result of the decomposition. Since the difference in the activation barriers is 0.22 eV, assuming the same pre-exponential factors, the ratio of the rate of formation of the intra-row structure C to the rate of formation of the on-dimer structure F is approximately 5000. At 573K, the rate of forming structure C would still be approximately 85 times faster than the rate of forming structure F. Thus our results show that the intra-row configuration is favored both energetically and kinetically. The difference in the activation barriers is actually larger than the difference in the energies of the two configurations.

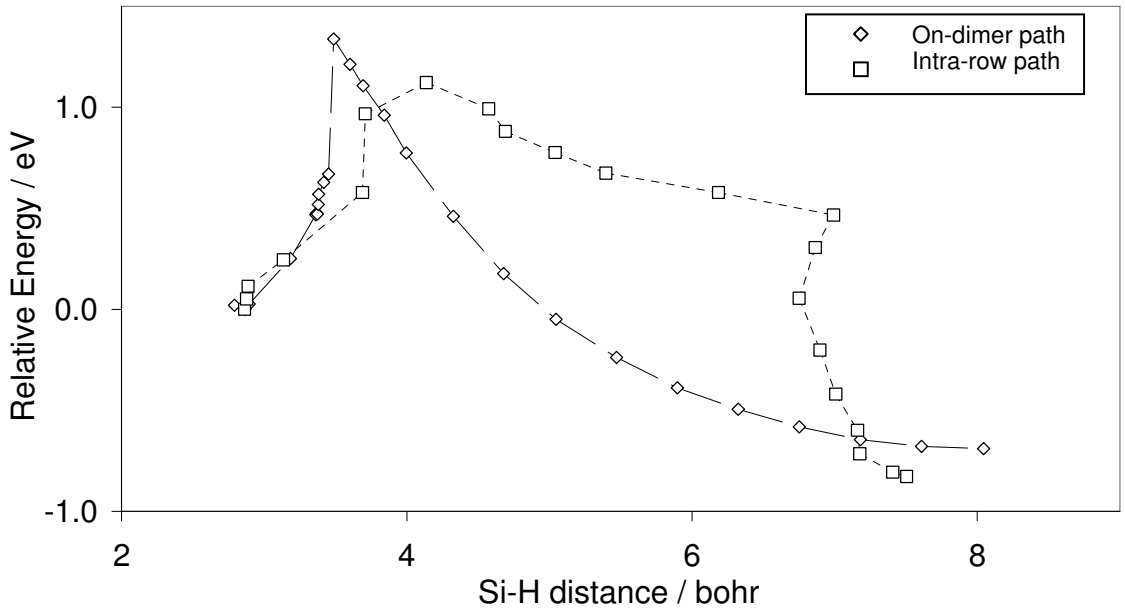

Figure 5.6: Plots of energy versus Si-H distance for the intra-row path (□) and the on-dimer path(◊). The initial, transition and final states are denoted by I, T and F, respectively.

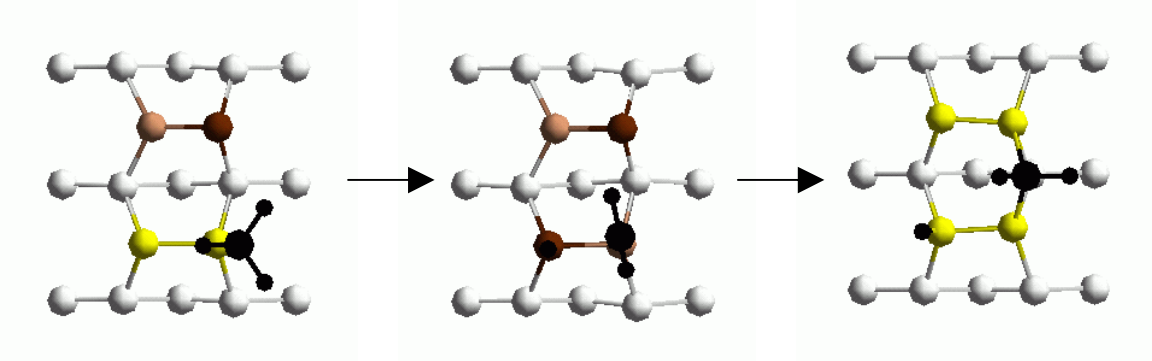

(a) (b) (c)

Figure 5.7: Structures of the (a) reactant, (b) transition and (c) product states for the intra-row path.

As shown above, the silicon-hydrogen distance d_{Si-H} is large at the transition state with the hydrogen atom already close to its final position in the product well. Thus, a significant amount of the energy needed to reach the transition state must go into this silicon-hydrogen bond stretching. An attempt was made to address the question of how this energy is partitioned into the various degrees of freedom of the decomposition products after the system passes the transition state. This is done by calculating, within a classical mechanical approximation, the frustrated translational energies acquired by the hydrogen atom and the silylene fragment in the exit valley of the reaction path. The work done on the fragments by the potential energy surface is plotted in Fig. 5.8 and 5.9 for the silylene and the hydrogen atom, respectively. As the system passes from the transition state to the decomposition product state, both the hydrogen atom and the silylene group acquire a significant amount of energy. In the exit valley, the force acting on each of the hydrogen atom and the silylene group is in the same direction as the displacement. It has been assumed that beyond the transition state the silylene and hydrogen atom are sufficiently decoupled from each other such that they do not exchange energy. This

estimate of the energy acquired in the exit channel is a rather rough estimate since we are essentially following the bottom of the minimum energy path, and hence do not take into consideration the dynamical coupling of the hydrogen and silylene motion to the phonon bath. The silylene-surface and hydrogen-surface bonds are roughly of the same strength but the hydrogen mass is much smaller so that this approximation may be better for hydrogen than for the silylene group. Within this approximation the results in Figs. 5.8 and 5.9 suggest that the decomposition process produces a hydrogen atom that is approximately 0.5 eV more energetic than the average thermal energy. This is consistent with STM observations [7], showing non-correlated positions of the silylene species and the hydrogen atoms, suggesting mobility of these species right after silyl decomposition.

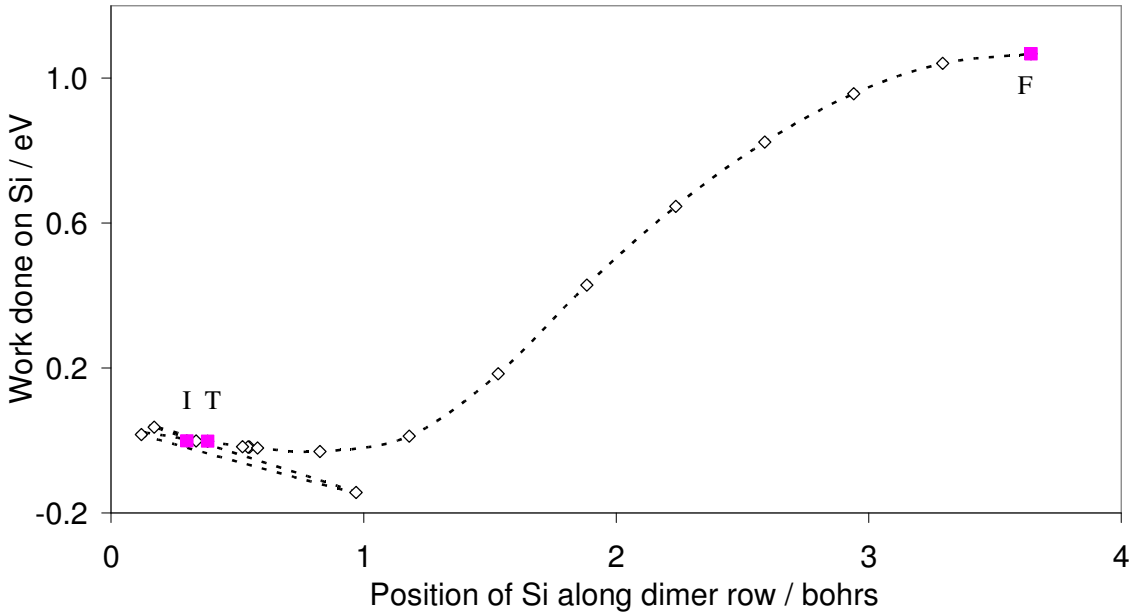

Figure 5.8: A plot of work done on the silicon atom in the [110] direction along the dimer row during the silyl decomposition into the intra-row silylene group. The initial position, transition state and its final position are as indicated on the plot as I, T and F, respectively. It can be seen from the plot that the silylene species gains energy as it moves in the direction of the dimer row after it breaks apart from the silyl species.

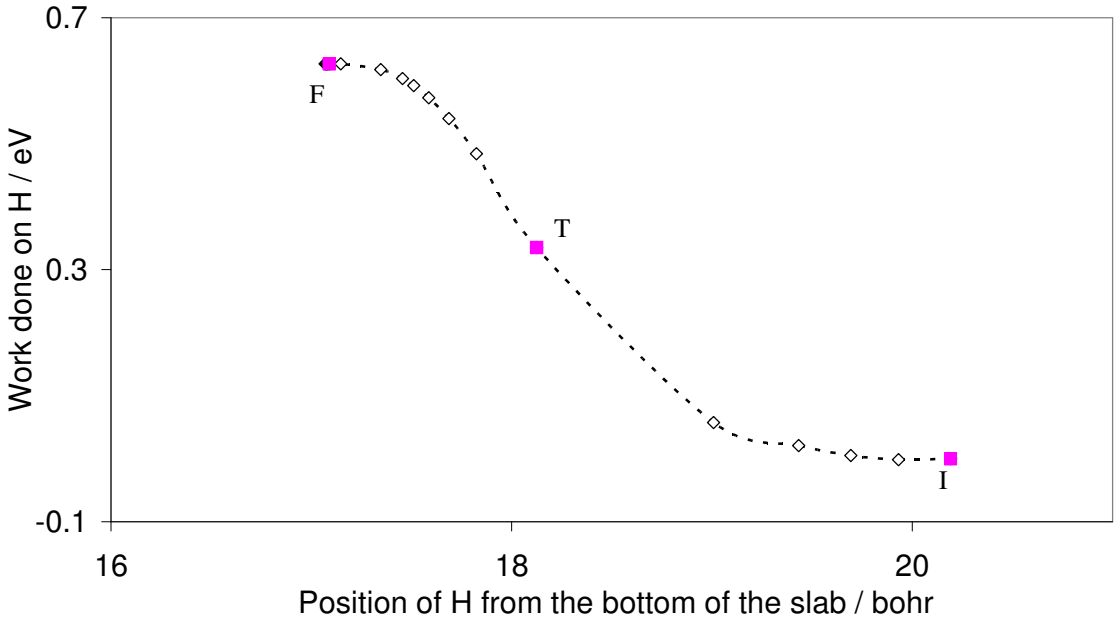

(a)

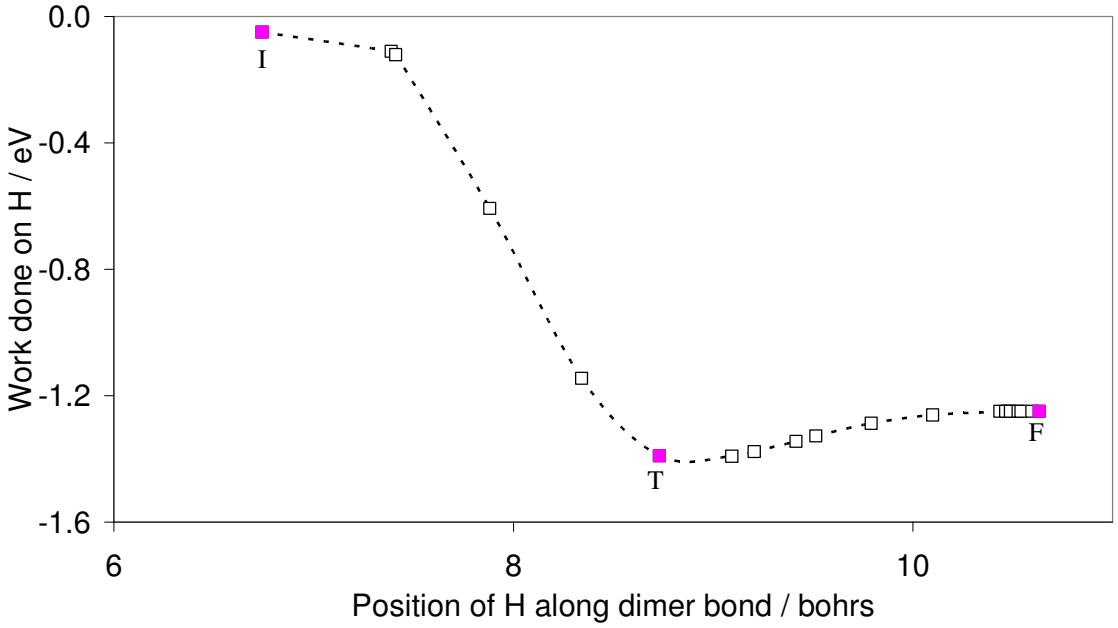

(b)

Figure 5.9: Plots of work done on the hydrogen atom that dissociated from the silyl group during the decomposition process: (a) work done in moving the hydrogen atom closer to the surface; (b) work done in moving the hydrogen atom in the direction along the dimer bond. Its initial position, transition state and its final position are as indicated on the plot as I, T and F, respectively. It can be seen from both plots that the atomic hydrogen gains energy in the exit channel of the dissociation path.

The on-dimer configuration has not been reported experimentally to the best of our knowledge. This is despite its energy being lower than the intra-row configuration in the absence of neighboring co-adsorbed hydrogen. Our results support the following scenario for silyl decomposition. First, the silyl group decomposes into intra-row silylene rather than an on-dimer silylene because of the more favorable kinetics. Then the hydrogen atom diffuses away leaving an isolated silylene which is trapped in the intra-row configuration.

5.3 Conclusions

In conclusion, two possible dissociation pathways from adsorbed silyl to silylene and hydrogen have been investigated. Our results show that the intra-row adsorption site is favored over the on-dimer adsorption site for the silylene group, for both thermodynamic and kinetic reasons. The activation barrier for forming silylene at the on-dimer site is 0.22 eV higher than at the intra-row site. Our calculations show that the adsorption energy at the intra-row site is larger by 0.18 eV in agreement with previous calculations that also favor the intra-row site thermodynamically. Analysis of the forces acting on the dissociating silyl group in the exit channel of the intra-row path shows that the hydrogen atom and the silylene groups are both significantly energetic after the dissociation process thus providing support for the transient mobility of the hydrogen atom.

6 Diffusion of SiH_3 decomposition products on Si(100)-(2×1)

This chapter of the thesis aims to describe some of the first-principles calculations that have been performed to study the diffusion of the silylene species on the silicon (100) surface. We compared the diffusion behavior of the silylene species to a silicon ad-atom and our results show that diffusion anisotropy of the silylene species is similar to that of a silicon ad-atom. The silylene diffusion path elucidated from our calculations is compared with previous results. The effect of co-adsorbed hydrogen on the silylene diffusion is also discussed. The presence of hydrogen not only modifies the diffusion barrier of the silylene along the dimer row, it also changes the diffusion path of the species. Finally we present here the energetics of silylene diffusion on a strained surface for the first time. We show that strain has a negligible effect on the surface diffusion of the silylene species.

6.1 Introduction

In the growth of silicon by ultra high vacuum chemical vapor deposition (UHV-CVD) or gas source molecular beam epitaxy (GSMBE), the species adsorbed on the surface during growth is, to a large extent, different from that occurring on the surface during growth by solid source molecular beam epitaxy (SSMBE). This is largely due to the hydrogen atoms that are added in conjunction with the silicon atoms when the gas source hydride precursors break apart on the substrate surface. For example, when using hydride precursors, we can expect silicon hydrides SiH_x to be the main silicon-containing species [2-5] on the surface during growth instead of the silicon ad-atom which is the sole species found in SSMBE [6]. We can therefore expect that the mechanism leading to growth from different sources will be different to some extent. On a macroscopic scale,

these differences translate to differences in the surface morphology. Although both growth methods (gas source and solid source) give rise to anisotropic islands at the early stages of growth, at coverage of 0.1 to 0.2 ML and temperatures between 573 and 673 K, the average island has an aspect ratio in the range of 10-30 for solid-source growth as opposed to the much shorter chain length of about 5 for gas-source growth. [5]

Common hydride precursors used in gas-source growth include silane and disilane. Under growth conditions, these hydrides will first react with the surface dangling bonds to form the silyl SiH_3 species via the following reactions:

$$Si_2H_6 + 2db \rightarrow 2SiH_3 \qquad \text{Rxn. (1) [2, 7-16]}$$

$$SiH_4 + 2db \rightarrow SiH_3 + H \qquad \text{Rxn. (2) [2-4, 8, 17, 18]}$$

When there is a sufficient number of dangling bonds in the vicinity, the silyl species will dissociate further to give adsorbed silylene and hydrogen in equal proportions.

$$SiH_3 + 2db \rightarrow SiH_2 + H \qquad \text{Rxn. (3)}$$

These reactions occur at temperatures as low as 150K. [2-4, 7-18]

The decomposition of the silylene fragment, on the other hand, is not so straightforward. One possible mechanism that was proposed involved the combination of two silylene groups to give a monohydride dimer and hydrogen gas [10, 19].

$$2\ SiH_2 \rightarrow H\text{-}Si\text{-}Si\text{-}H + H_2 \qquad \text{Rxn. (4)}$$

The second-order kinetics of this reaction, as evident from temperature-programmed desorption (TPD) experiments, suggests that there is no pre-pairing of the silylene species. Thus it reveals the importance of silylene diffusion in silicon agglomeration which in turn affects growth.

The temperature at which the silylene species decomposes is dependent on the precursor flux and the surface coverage. A kinetic simulation has shown that the silylene species will survive up to a higher temperature when the silane flux is increased [20]. The simulation considered the variation of two essential deposition parameters within the range compatible with their experiments. Firstly, the surface concentration of various decomposition products is analyzed by varying temperature between 500K and 800K and keeping pressure of silane constant at 2×10^{-6} mbar. Secondly, they also simulated the case of holding temperature constant at 690K and varying pressure between 2×10^{-7} mbar and 2×10^{-5} mbar. The conclusion is that the silylene species is the dominant SiH_x species at 690 K while $p(SiH_4) \geq 1 \times 10^{-5}$ mbar and at $p(SiH_4) = 2 \times 10^{-6}$ mbar with $T \leq$ 650 K. A SSIMS and TPD study carried out by Gates, *et. al.* found that at low surface coverages, SiH_2 decomposes between 650K and 775K, while at high surface coverages, the SiH_2 group decomposes from 750K onwards [2]. It is clear from the above that the silylene group is the main silicon-containing species on the surface of silicon (100) at the growth conditions used in gas source growth. The diffusion of this species is therefore an important process to look at in the study of growth.

STM and growth experiments show that the silylene fragments are already mobile at approximately 470 K [19]. Indeed, earlier STM data also imply that the silylene species is mobile at room temperature although it was not clear at that time if the mobility at this temperature is transient or intrinsic [11]. More recent investigations of island growth kinetics yield an effective diffusion barrier of 1.3 eV [21]. This is an upper limit for the actual diffusion barrier because of the effects of co-adsorbed hydrogen atoms and the decomposition of the silylene fragment upon the kinetics. These experimental probes

of silylene diffusion yield only an upper limit for the diffusion barrier, and are indirect because of the large number of other elementary surface processes occurring. The diffusion pathway is also not directly accessible through these experiments.

The energy barrier and diffusion mechanism of a silylene species along the dimer row have been theoretically estimated by Bowler [22]. In his work, the local density approximation was used to map out the potential energy surface for diffusion of the silylene species. This potential energy surface shows three paths as illustrated in fig. 6.1, the on-dimer to on-dimer paths with the barrier of 1.4 eV, the intra-row to intra-row paths also with the barrier of 1.4 eV, and the on-dimer to intra-row with a low barrier of 1.1 eV. Although addressing the same three paths, our conclusions are fundamentally different from his. The difference will be discussed in the later sections. In the work discussed above, silylene diffusion along the dimer row occurs via a preferred zig-zag path, illustrated by small slanted arrows on Fig. 6.1, from on-dimer to intra-row and then from intra-row to on-dimer.

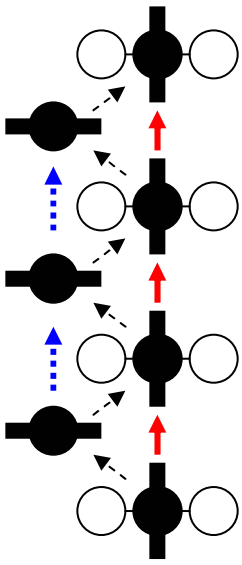

Figure 6.1: An Illustration of the diffusion mechanisms proposed in Bowler's work. (a) on-dimer to on-dimer hop with a barrier of 1.4 eV (b) intra-row to intra-row hop with a barrier of 1.4 eV (c) on-dimer to intra-row with a barrier of 1.1 eV

On the other hand, silicon ad-atoms diffusion is a more thoroughly studied subject as opposed to that of the silylene species [6, 23-30]. The diffusion coefficient is defined as $D_0\exp(-E/k_BT)$ where the barrier E is estimated from STM data at temperatures between 350 to 550 K to be 0.67 ± 0.08 eV along dimer row and 1 eV along the dimer bond; D_0 is estimated to be about $10^{-3\pm1}$ cm^2/s [6]. A few groups have used classical molecular dynamics [29, 30] and first-principles total energy calculations [27, 28, 31] to identify the adsorption site of silicon ad-atoms and the diffusion mechanism and barrier. These provide evidence for the anisotropic diffusion of the silicon ad-atom with a preferred direction along the dimer row with a barrier ranging from 0.55 to 0.75 eV. Diffusion takes place via a pathway equivalent to the on-dimer to on-dimer hop (Fig. 6.1a) described in Bowler's work [22].

In the presence of co-adsorbed hydrogen ad-atoms, the silicon ad-atom diffusion barrier along the dimer row has been observed using STM to double at very small hydrogen coverage [23]. However, when the hydrogen coverage is increased to one monolayer, first principles calculations using the LDA approximation suggest that the diffusion mechanism becomes substantially modified such that the barrier becomes similar to that for diffusion on a clean surface [24, 25]. On the other hand, with hydrogen coverage greater than one monolayer, the diffusion barrier is estimated to be so high (between 2.2 to 2.7 eV) [26] that it can account for why growth becomes eventually disrupted [32]. It has been proposed that the silicon is more likely to hop in the direction perpendicular to the dimer row when it approaches a hydrogen-terminated silicon dimer [26].

6.2 Results and Discussion

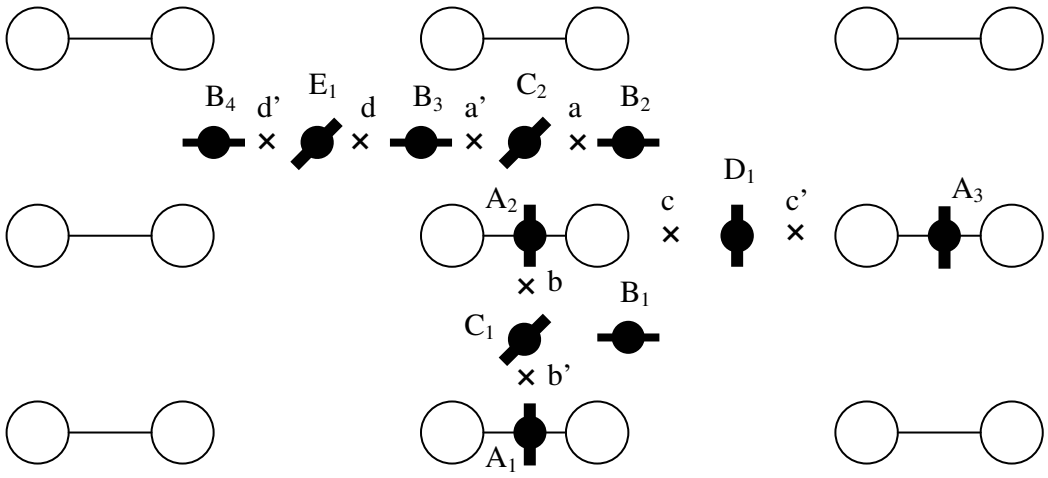

(a)

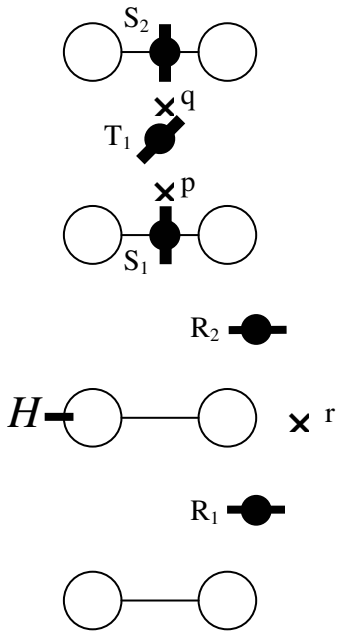

(b)

Figure 6.2: An illustration of the Si(100) surface from the top view. Surface dimers are shown by open circles joint by a horizontal line. Capital letters A-E and black dots marks the different local minima the silylene group could exist in. Small letters a-d and crosses marks the various saddle points. Subscripts and superscripts differentiate equivalent structures, for instance, A_1, A_2 and A_3 are equivalent minima while a and a' are equivalent saddles. (a) silylene adsored on bare silicon (100) surface (b) silylene co-adsorbed with hydrogen on the silicon (100) surface.

By tracing various diffusion paths of silylene on the surface, the minima and saddle points for diffusion are mapped. The results are summarized in the top portion of Table 6.1 and Fig. 6.2(a).

Table 6.1: Diffusion barrier of silylene with and without co-adsorbed hydrogen atom. The starting structure and ending structure are labeled according to that illustrated in figure 6.2.

Starting structure	Ending structure	Forward barrier	Reverse barrier
A_1	C_1	0.88 eV	0.16 eV
C_1	A_2	0.16 eV	0.88 eV
A_2	D_1	1.46 eV	0.75 eV
D_1	A_3	0.75eV	1.46 eV
B_2	C_2	0.63 eV	0.08 eV
C_2	B_3	0.08 eV	0.63 eV
B_3	E_1	< 2.4 eV	~0.15 eV
E_1	B_4	~0.15 eV	< 2.4 eV
R_1	R_2	1.30 eV	1.30 eV
S_1	T_1	1.15 eV	0.15 eV
T_1	S_2	0.15 eV	1.11 eV

In Fig. 6.2(a) the surface dimers are represented by large empty circles joined by lines. The local minima for adsorbed silylene species are denoted by capital letters and the saddle points for silylene species diffusion are denoted by small letters marked with crosses. The global minimum for silylene adsorption (in the absence of co-adsorbed hydrogen) is the on-dimer configuration denoted by A_n. The subscript n simply labels the

various equivalent adsorption sites. With respect to the global minimum at A, the minima at B, C and D have relative energies of 0.17eV, 0.72eV and 0.71eV respectively. Note that D is a local minimum located in the trench between two dimer rows. There is another local minimum in this trench at E. This latter structure is rather unstable, having a relative energy of about 2.4 eV greater than A. Similarly, relative to the minimum at A, the saddle points a, b and c have relative energies of 0.80eV, 0.88eV and 1.46eV respectively, while the energy of saddle point d is approximately 2.6 eV greater than A. The energetics of the paths A_1-C_1-A_2 (along the dimer row), A_2-D_1-A_3 (across the dimer row) and B_2-C_2-B_3-E_1-B_4 (also across the dimer row) are plotted in Figs. 6.3, 6.4 and 6.5 respectively.

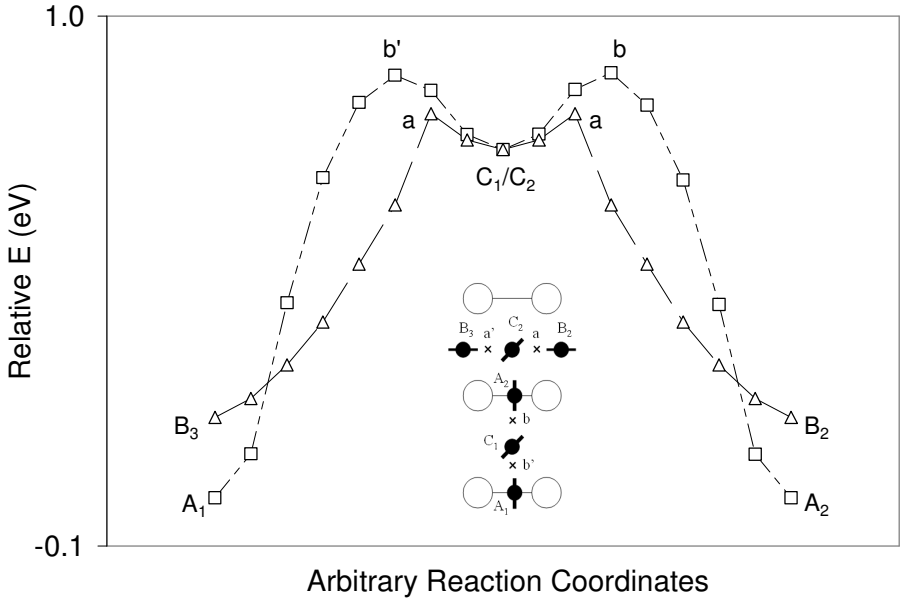

Figure 6.3: This graph shows the superposition of the total energy variation when the two SiH_2 diffusional paths A_1-C_1-A_2 and B_2-C_2-B_3 are superimposed.

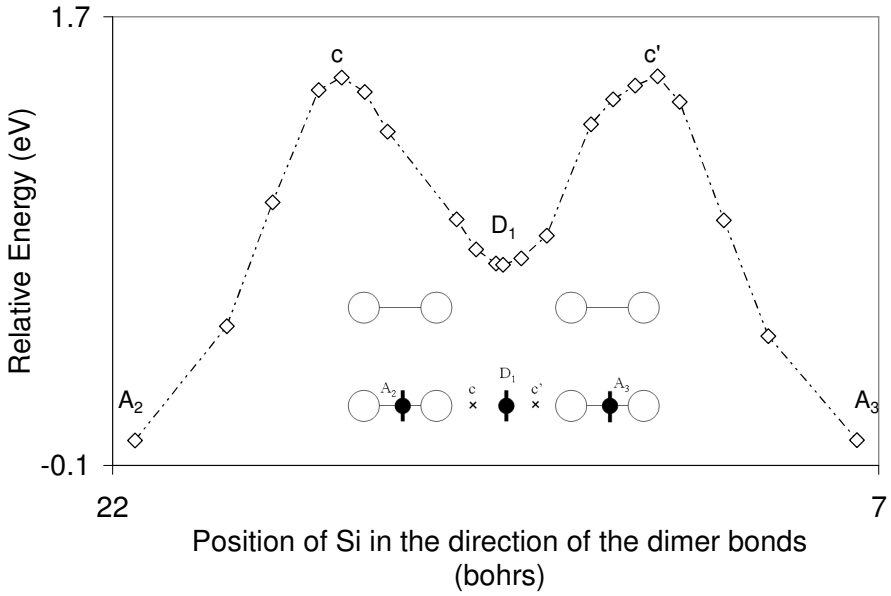

Figure 6.4: This graph shows the energy variation for the inter-row SiH_2 diffusion via the A_2-D_1-A_3 path.

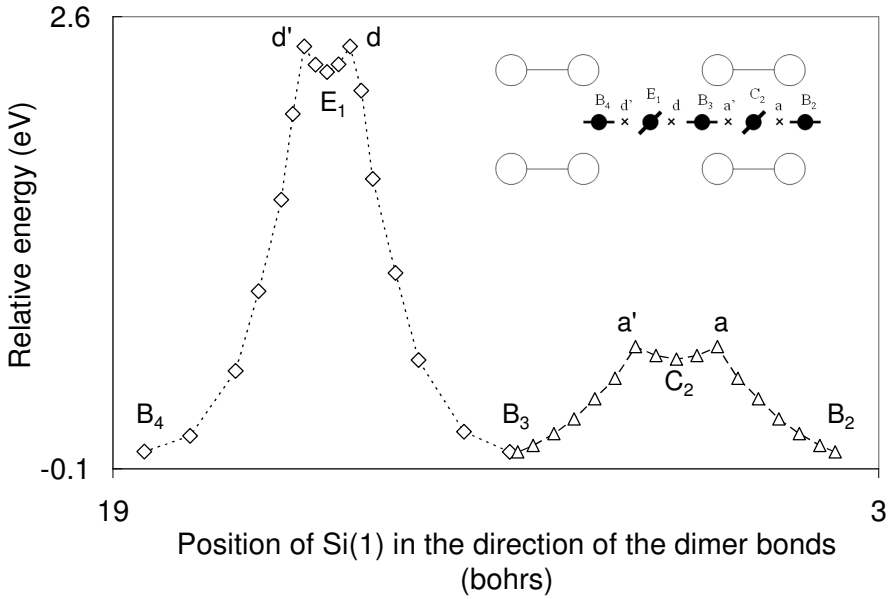

Figure 6.5: This graph shows the total energy variation for the inter-row SiH_2 diffusion via the B_2-C_2-B_3-E_1-B_4 path

For diffusion along the dimer row, the lowest energy path for the silylene at A_1 to diffuse will be through C_1 along the middle of the dimer row; this is the on-dimer to on-dimer path A_1-C_1-A_2. The energy barrier for this path is 0.88eV. We did not find a

diffusion path that joins B_1 to B_2 (the intra-row to intra-row path) along the dimer row. Despite an intense search we also did not find a diffusion path that directly joins A_1 to B_1 (the on-dimer to intra-row path). Thus, from our data, the diffusion barrier along the dimer row is approximately 0.88 eV. On the other hand, for diffusion perpendicular to the dimer row, the silylene species can move directly on-top of the dimers via the A_2-D_1-A_3 path or in the gap in between two dimers via the B_2-C_2-B_3-E-B_4 path. The energy barrier for the former path is 1.46eV while that for the latter path is considerably higher at 2.59 eV. We did not trace the path for silylene to move along the trench between two dimer rows but the energy barrier is approximately 1.73eV from the relative energies of D and E.

For diffusion along the dimer row via the on-dimer to on-dimer hop, assuming an attempt frequency of about 10^{13} s^{-1}, the rate of diffusion is appreciable at room temperature. At room temperature, for example, the on-dimer silylene group will hop from one dimer to the next in less than one minute. By 400 K, the hopping of silylene from one dimer to the next will take less than one second. However, for diffusion across dimer row through the A_2-D_1-A_3 path, the high barrier of 1.46eV implies that diffusion across the dimer row becomes appreciable only at temperatures close to 600K. Our results show that for silylene on a bare surface, the energy barrier difference for diffusion across the dimer row relative to diffusion along the dimer row is 0.58 eV. This can be compared to the 0.4 eV energy barrier difference for the silicon ad-atom [27].

Thus, it is clear, at this point, that the silylene species has similar diffusion anisotropy to a silicon ad-atom on the clean silicon (100)-(1×2) surface. The silylene species diffuses (significantly) preferentially along the dimer row although clearly at

sufficiently high temperatures, diffusion along both directions occurs. On the bare silicon surface, there is a slightly greater anisotropy in the case of the silylene species (0.58 eV compared to 0.4 eV). For the silicon ad-atom, anisotropic diffusion was used to explain why the fast growth is observed at the ends of the dimer rows and diffusion along both S_A and S_B step edges may be faster than on the flat terrace surfaces. Our results imply that similar conclusions apply for the silylene species with respect to step dynamics.

It is known that islands of silicon grown on Si(100)-(1×2) have an anisotropic shape; these islands are considerably more elongated in the direction perpendicular to the dimer rows (in the [110] direction) of the terrace below rather than along the dimer row (in the $[\bar{1}\bar{1}0]$ direction). [5, 37]. If we assume that island shape is determined by the relative diffusion rates, we might expect that the shape of the silicon islands grown using gas sources will be even more anisotropic, since the diffusion anisotropy is slightly greater for silylene than for silicon ad-atoms. Experimental observations of the islands, however, show a discrepancy [5, 37]. Thus, our calculations of the diffusion anisotropy for silylene in comparison with that for silicon ad-atoms suggests two possible scenarios; either the island shape depends more upon the probability of incorporation of silicon atoms into a growing island than upon the rate at which silicon is transported to the island, or the presence of hydrogen during GSMBE as another impact on the diffusion anisotropy than that related to the silylene species. This point will be revisited in the discussion of silylene diffusion in the presence of co-adsorbed hydrogen.

A similar study of the diffusion paths for silylene has been performed previously [22] using the local density approximation. The paths traced by Bowler are illustrated in Fig. 1 and they are equivalent to our A_n-A_{n+1}, B_n-B_{n+1} and A_n-B_n. Contrary to this work,

we have found no direct path between A_n and B_n and similarly so between B_n and B_{n+1}. In view of Bowler's study, we have performed calculations to find a path between structures A_1 and B_1 first by fixing the lateral (Y, Z) coordinates of the silicon on the silylene diagonally along a straight line between these two structures. These points are plotted in Fig. 6.6 and are separated into two regions, Region 1 and Region 2, respectively. They are henceforth known as the diagonal-points.

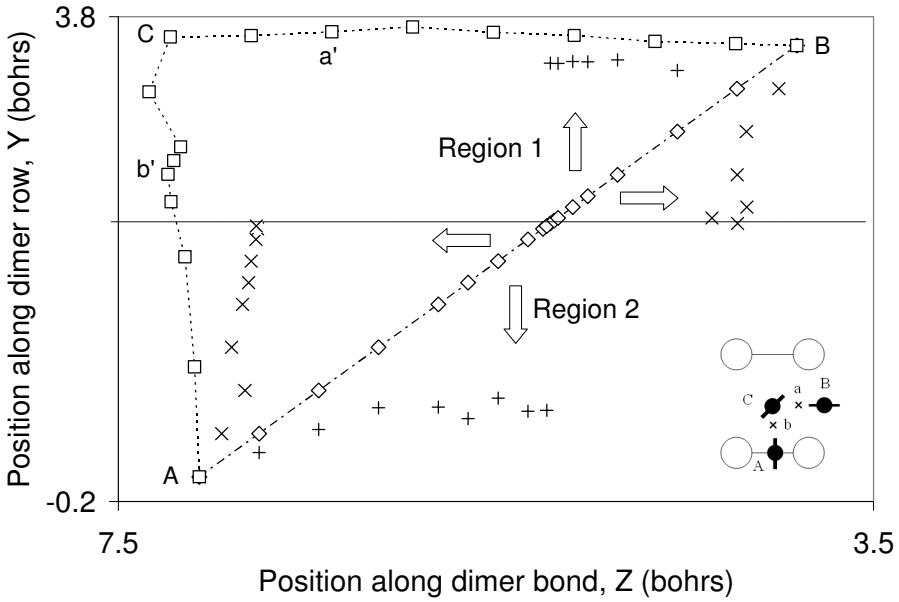

Figure 6.6: An illustration of the absence of a direct path between structures A_1 and B_1. A possible path between A_1 and B_1 is via C_1. The positions A_1, B_1 and C_1 are illustrated in the lower-right-hand corner of the figure.

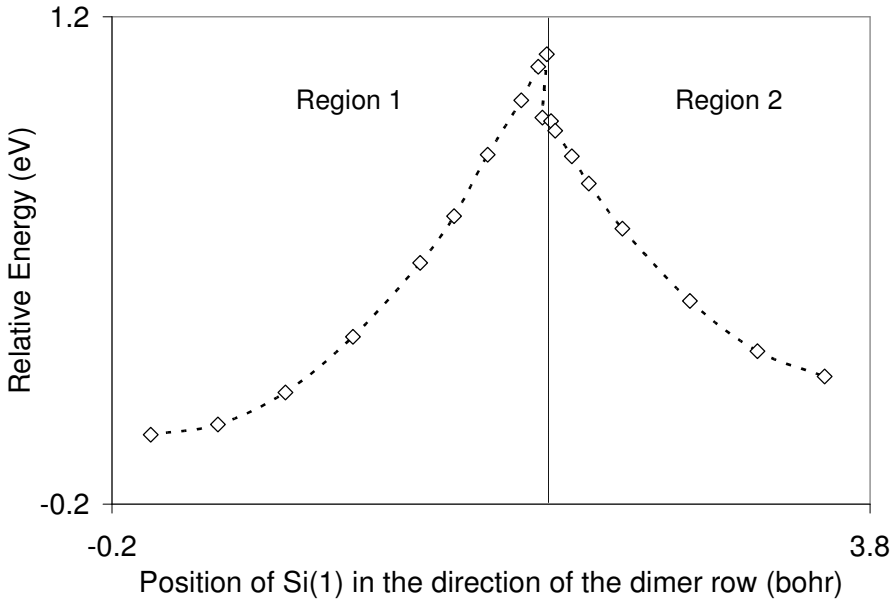

Figure 6.7: Total energies variation along the path between structures A_1 and B_1 and corresponding to the points with lateral coordinates of the silicon on the silylene fixed diagonally across A_1 and B_1.

The corresponding total energies of these diagonal-points are shown in Fig. 6.7, where the regions 1 and 2 are also labeled. It is apparent from the plot that the total energy variation of these points is disjoint. The discontinuity in the energy is expected in this case since this is a forced-fitting of the minimum energy path directly along a diagonal line between A_1 and B_1. In actual fact, the path might not be directly along the diagonal but can deviate from the line. This discontinuity in the energy graph simply implies that there is no such "classic-saddle point behavior" directly on the diagonal line as describe in Bowler's dissertation. We have also found that at the points along the diagonal where the discontinuity in the total energy occurs, a discontinuity in the positions of the hydrogen atoms in the silylene group occurs. We attempt to identify a path that is close to the diagonal path between A_1 and B_1 by optimizing structures starting from the converged diagonal-points and releasing one of the constraints such that these points are now either constrained in the Y coordinate or constrained in the Z coordinate

but not both. We found that the points in region 1 collapse upwards and to the right while the points in region 2 collapse downwards and to the left. The results shown in Fig. 6.6 lead us to a totally different conclusion from that by Bowler. The arrows on the graph in Fig. 6.6 show the direction that the diagonal-points move along when one of the constraints is removed. The arrows pointing up and down show the directions in which the diagonal-points move when they are constrained in the plane fixed by the Z coordinate. On the hand, the arrows pointing left and right show the directions in which the diagonal-points move when they are constrained in the plane fixed by the Y coordinate. The results of these single-constraint calculations still show relatively large forces of the order of 10^{-3} hartree/bohr in the direction of the arrows. Thus, we conclude that there is no potential energy valley that connects the on-dimer minimum (A_1) directly to the intra-row minimum (B_1). In view of the direction of the forces and the relatively long time that the calculations took to fully converge, we proposed that the diffusion path along the dimer row for a silylene fragment is A_1-C_1-B_1. The forces along A_1-C_1-B_1 are relatively small in the vertical direction ($< 2.5\times10^{-4}$ hartree/bohr) but are quite significant in the plane of the dimer rows. Particularly, when the silylene is moving from A_1 to C_1, the forces are negligible along the dimer bond but have magnitude as high as 0.0275 hartree/bohr along the dimer row. On the other hand, when the silylene is moving from C_1 to B_1, the forces are negligible along the dimer row but have magnitude as high as 0.015 hartree/bohr along the dimer bond. We also attempted to trace the same path in the presence of a co-adsorbed hydrogen, but we were not successful.

From our results, there is no classic saddle-point behaviour to go between the on-dimer and the intra-row structures suggested by Bowler's work for silylene to diffuse

from the A_1 and B_1. In addition, we have also observed that there is no such saddle-point behaviour between the two structures even in the presence of a co-adsorbed hydrogen ad-atom. Diffusion between A_1 and B_1 is likely to go through a path via C_1, with a very shallow minimum at C_1. The total energy variation for this path is shown in Fig. 6.8. The silylene species at A_1 moves along the dimer row towards a local minimum at C_1 surmounting a barrier of 0.88 eV at the saddle-point b and then moves in the direction parallel to the dimer bond towards B_1 with a very small barrier of only 0.08 eV at saddle-point a.

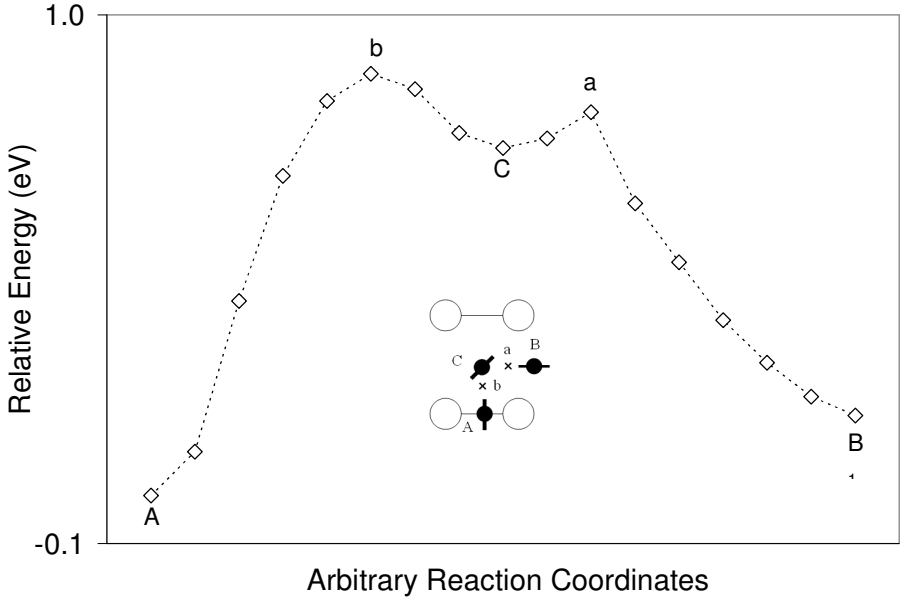

Figure 6.8: Total energy variation for the SiH_2 diffusion path via the A-C-B path.

From our calculations, we also were not able to find a potential energy valley that connects B_1 to B_2 directly. It is found that by constraining the silylene fragment to move along a path connecting B_1 directly to B_2, the structure converges to the minimum at A2. A silylene species at B_1 can only diffuse to B_2 indirectly through some other path. A possibility is the path through C_1, C_2 and A_2 which will has a barrier of 0.88 eV as in diffusion from A_1 to A_2. However, this path involves a tremendous change in the

momentum of the species as the direction of motion need to be constantly changed for the species to fall into the "right" valley.

Now, what happens to the diffusion barrier in the presence of co-adsorbed hydrogen? We find that the presence of hydrogen modifies not only the diffusion barrier of the silylene along the dimer row; it also changes the diffusion path of the species. The equivalent of Fig. 6.2(a) for diffusion in the presence of a hydrogen ad-atom is shown in Fig. 6.2(b). As with Fig. 6.2(a), capital letters R, S and T denote the minima, and small letters p, q and r denote the saddle points. We saw above that diffusion along the dimer row of silylene directly from one intra-row position to the next intra-row position (B_1-B2 in Fig. 6.2(a)) does not occur in the absence of hydrogen. Quite interestingly, this diffusion path (R_1-r-R_2 in Fig. 6.2(b)) is easily found with a co-adsorbed hydrogen ad-atom present. When hydrogen is co-adsorbed with the silylene species, the global minimum for the silylene species is R_n (the intra-row configuration) instead of S_n (the on-dimer configuration). This switch in the relative energy of the on-dimer and the intra-row structures is in agreement with other theoretical work [40-43]. Adsorption at the sites S_1, S_2 and T give energies of 0.15eV, 0.19 eV and 1.15 eV relative to adsorption at site R. A plot of total energy variation in the presence and absence of hydrogen for the on-dimer to on-dimer hop can be found in Fig. 6.9 below.

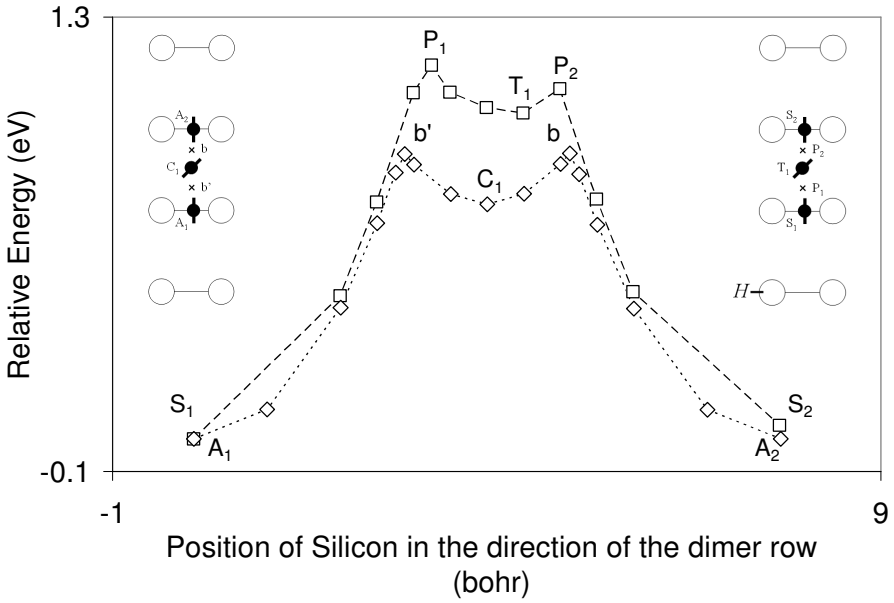

Figure 6.9: Total energy variation of the intra-row SiH2 diffusion path via the on-dimer-on-dimer hop. The path in the presence of co-adsorbed H is plotted on the same graph as the path on bare surface.

The bottom half of Table 6.1 gives a summary of the diffusion barrier of the silylene species along the dimer row in the presence of a hydrogen ad-atom. We can see that the diffusion of the silylene species along the dimer row can now occur via the R_1-r-R_2 path and the S_1-p-T_1-q-S_2 path. The former path has a barrier of 1.3 eV while the latter path has a barrier of 1.15 eV. We assume that the silylene diffusion across the dimer row is only slightly affected by the presence of hydrogen on the surface since the distance between neighbouring dimer row is quite large compared to neighbouring dimers on the same dimer row. Thus, we expect the difference in the silylene diffusion barrier across the dimer row and the diffusion barrier along the dimer row is now smaller in the presence of co-adsorbed hydrogen.

Our calculations suggest that the effects of hydrogen co-adsorption on silylene diffusion are twofold. Firstly, in the presence of co-adsorbed hydrogen, the rate of

diffusion of the silylene species along the dimer row becomes significantly slower. This is evident from the higher value (1.15 eV compared to 0.88 eV) of the diffusion barrier when hydrogen is present. The magnitude of the calculated energy barrier suggests that in the presence of co-adsorbed hydrogen there is effectively no diffusion at room temperature. Secondly, the surface diffusion of the silylene species would be less anisotropic because the difference in the diffusion barrier along the dimer row relative to that across the dimer row is now smaller. A similar effect has been reported for diffusion of silicon ad-atoms, whereby the presence of co-adsorbed hydrogen causes the silicon ad-atom diffusion path perpendicular to the dimer row to become more favorable compared to diffusion along the dimer row [28]. This study used the local density approximation to calculate the diffusion barrier of silicon ad-atoms on a silicon surface with co-adsorbed hydrogen. It was found that when the silicon ad-atom approaches a hydrogen-terminated silicon dimer, the diffusion barrier is significantly increased from 0.6 eV to 1.3 eV – which is 0.3 eV greater than the barrier for the silicon ad-atom to get across the dimer row.

As we have mentioned earlier, the presence of hydrogen during GSMBE might have other impact to the diffusion anisotropy than that related to the silylene species as we found a discrepancy between the species diffusion anisotropy and the growth island aspect ratio. In this case, for SSMBE, there is no hydrogen on the surface, hence the anisotropy is governed by the energy barrier difference for silicon ad-atom to diffuse across the dimer row relative to that along the dimer row. This is reported as 0.4eV in reference 27. However, in the case for GSMBE, other than a change in diffusion species (from a silicon ad-atom to the silylene species), there is also the presence of hydrogen on

the growth surface that affects the diffusion anisotropy. The difference in diffusion barrier across and along the dimer row in the latter situation is now 0.16eV, which is 0.24eV lower than that for a silicon ad-atom. Thus we can now understand the difference in the aspect ratio of the growth island with reference to the difference in the diffusion anisotropy in the case of SSMBE and GSMBE.

The effect of hydrogen on the silylene diffusion barrier can be attributed to the chemisorption-induced disruption of the surface electronic structure on the silicon (100) surface [36]. In the work by Chen and Boland, a*b initio* calculations were used to show how surface states of dimers next to an adsorbate, in particular hydrogen, become significantly modified. The bare surface dimer bond that is isolated by hydrogenated dimers in its neighborhood becomes strengthened by the enhanced local π-interaction. In their study, tilted bare dimers that are separated by one hydrogenated dimer are shortened by 0.036Å and the bare dimer bond lengths decreases as the separation between bare dimers increases. This trend reflects the increasing isolation of the bare dimers which in turn enhances the local π-interaction between the dangling bonds, resulting in shorter bond lengths. In our study, we found that a clean dimer bond in a nearest-neighbour position to an adsorbed hydrogen or a silylene gets slightly shortened by about 0.02 Å compared to the clean surface. This change is of the same order of magnitude as that found in the work by Chen and Boland [36] and suggests a similar disruption of surface electronic structure, although in our work the neighboring dimer is singly occupied, whereas in Ref. 36 the effect observed is due to a neighboring doubly-occupied dimer. The silicon-silylene bond is shorter when hydrogen is co-adsorbed on a neighbouring dimer; this suggests a stronger adsorbate bond. On the surface with co-adsorbed

hydrogen the silicon-silicon bond between the adsorbed silylene and the surface dimer gets shortened by 0.01 Å compared to that on the bare surface. While this change is extremely small, it gives an indication of the extent by which the adsorbate and substrate bond is strengthened. Hence with co-adsorbed hydrogen, the silylene species encounters a greater barrier to break its bond to the substrate and hop to the next adsorption site.

6.3 Conclusions

To summarize, our calculations point us to various similarities and differences between the diffusion behaviour of silicon ad-atom and silylene species on the silicon (100) surface. Both species have anisotropic diffusion with a preferred direction along the dimer row, but our results indicate that diffusion of the silylene species is less anisotropic compared to that of the silicon ad-atom. This result is consistent with the experimental observation of less anisotropic islands in gas-source growth than in solid-source growth. While the presence of co-adsorbed hydrogen increases the diffusion barrier of the silicon ad-atom, its presence enables the diffusion of the otherwise immobilized intra-row silylene species.

7 Diffusion on strained and Germanium-doped Silicon surface

This final discussion chapter presents the diffusion kinetics of the silylene and hydrogen on strained and germanium-doped Si(100)-(2×1) surface that was studied using pseudopotential density functional calculations. The results provide some understanding of the effect of strain on surface diffusion kinetics. We find that while lattice strain has an negligible effect on the diffusion kinetics of the silylene species, it can significantly increase the surface diffusion barrier of an hydrogen ad-atom when the lattice is strained beyond ~1.3%. In particular, the barrier for hydrogen atoms to diffuse is increased by 0.15eV (~10%) when the silicon lattice undergoes a 4% tensile strain. Finally, we have also attempted to decouple the chemical effect of germanium and the effect of strain on hydrogen diffusion.

7.1 Introduction

Silicon-germanium is an important material to the semiconductor industry because of the great interest in silicon-germanium heterostructure devices. Hence understanding growth processes on strained silicon and silicon-germanium is important.

Silicon can be pseudomorphically grown over a silicon-germanium substrate to obtain strained silicon. With the increasing importance of strained silicon in the microelectronics industry, the understanding of ad-atom behaviour on strained silicon becomes increasingly valuable. The strain dependencies of ad-atom binding and migration energies have important impacts on island growth kinetics in the heteroepitaxial growth of lattice-mismatched thin films as well as film morphology. Since

it is hardly possible to experimentally isolate the effect of strain on diffusion mechanism, they are most conveniently studied by using first-principles calculations.

The effect of strain on the diffusion of ad-atoms on Si(100) surface has been studied by Roland and Gilmer [1]. In their molecular dynamics study, using the Stillinger-Weber potential, the diffusion barrier along the dimer row is increased by about 10% for a 3% compressive as well as for 2% tensile strain. In another study, Spjut and Faux [2] found the diffusion barrier lowered by the application of a 1% to 1.5% tensile strain to the substrate, in the direction perpendicular to the dimer row.

On metal surfaces, surface diffusion rates are found to be very sensitive to the presence of lattice-mismatch-induced strain. For instance, on the strained Ag(111) surface, experimental and theoretical studies found good agreement in the effect of strain on the diffusion barrier. Experimentally [3], the diffusion barrier of Ag-atoms is shown to decrease significantly as the surface is strained compressively by about 4%. Theoretical methods have also been used to show that within a strain of ±5%, the diffusion barrier varies linearly with respect to strain with the tensile or compressive strain causing the increase or decrease of diffusion barrier respectively. This is in agreement with the molecular dynamics by Schroeder and Wolf [4] which gave a generalization on the dependence of diffusion barrier on the strained (100) surfaces. Such generic models where the bonding is non-directional are probably not applicable to diffusion on the covalently defined silicon surface.

While it is now generally accepted that tensile strain increases the surface diffusion barrier of ad-atoms on metal surfaces and compressive strain enhances the rate of diffusion, we can expect the dependence of the diffusion barrier on strain to be

different on the silicon surface. Hence, it can be seen that while metal surfaces gave a clear trend of the effect of strain on diffusion barrier, on the semiconductor surfaces there is still no clear understanding of this.

Other more recent first principles calculations, performed to study diffusion on strained surface include the study of silicon ad-atom diffusion on strained silicon (111) surface [5] and the study of germanium ad-atom on strained silicon (100) and germanium (100) surface [6]. These investigations using Gaussian94 [5] and VASP [6] showed that diffusion of surface ad-atom decreases under tensile strain or compressive strain, respectively. The decrease in the diffusion barrier for both cases is around 0.1eV.

On the experimental side, Zoethout *et. al.* have attempted to study the diffusion of silicon ad-dimer along the dimer row of a strained silicon (100) surface [7]. It was found that the rate of diffusion of a silicon dimer along the substrate dimer rows on silicon (100) is relatively insensitive to tensile strain.

As the importance of strained material continue to gain importance both in research and industrial applications, it is therefore important for us to understand how strain affect the diffusion process on the surface during growth. We have therefore performed first-principle's calculations on the diffusion on strained silicon surfaces. It is the aim of this work to study the effects of strain and Ge-doping on the diffusion of SiH_3 decomposition products on silicon surfaces.

In the simulation of a lattice undergoing tensile strain, we have forced the silicon atoms to deviate progressively from the silicon lattice (a = 5.43Å) to take-on the lattice constant of a germanium lattice (a = 5.66Å). By doing so, we are simulating a

pseudomorphic silicon grown on substrate ranging from 0% germanium to 100% germanium with a maximum of 4% lattice mismatch.

7.2 Results and Discussion

While the influence of co-adsorbed hydrogen on the diffusion of a silylene species is tremendous [as shown by our work], the effect of apply a tensile strain on the lattice is negligible. The change in the barrier and the shape of the total energy variation is not significant. As shown in figure 7.1, the difference in the two barriers is only 0.02 eV. This amount is of the same order of magnitude as the error involved in the calculations.

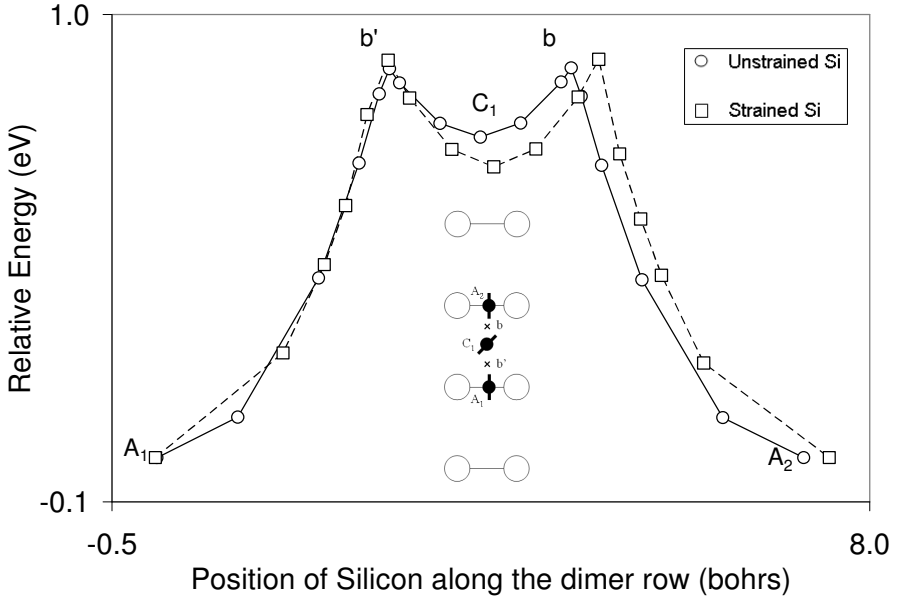

Figure 7.1: Plots of energy versus position of silylene-silicon in the direction along the dimer row for the strained (□) and unstrained (O) silicon substrate. Positions of the silylene species (A_1, b, b', C_1, A_2) are marked respectively as illustrated in the figure attached.

Our result is consistent with that experimentally found for the diffusion of silicon addimer along the dimer row of a strained silicon (100)-(1×2) surface [7] By the use of

STM, the rate of diffusion of a silicon dimer along the substrate dimer rows on silicon (100)-(1×2) was found to be relatively insensitive to tensile strain.

However, this insensitivity of the silylene diffusion barrier toward strain is contrary to that found for silicon ad-atom [2]. In the molecular dynamics work mentioned above, the authors predicted that by applying tensile strain in the direction perpendicular to the dimer row, there is a possible significant increase in the diffusion rate along the dimer row. This difference may have significant implications for the morphology of strained silicon growth.

Thus, while the diffusion rate of silicon ad-atoms in solid-source growth is expected to be strain-dependent, the diffusion rate of silylene in gas-source growth is not, as evident from our results. For instance, in the growth of silicon-germanium films, the effect of strain introduced by the presence of germanium will affect the silicon ad-atom diffusion, but is not expected to affect the diffusion of the silylene species present in gas-source growth.

The effect of strain on the surface diffusion of hydrogen is more pronounced. In figure 7.2, it is apparent that the diffusion barrier does not have a linear dependence to the amount of strain applied, in contrary to that found for strained metallic (100) surfaces [3, 4]. In particular, when the lattice strain remains below ~1.3%, the variation in the diffusion barrier is very gradual and is in fact close to the error-limit of our calculations. However, when the lattice is strained beyond ~1.3%, the increase becomes more pronounced. The investigation is done up to a lattice strain of ~4% which corresponds to that induced by a germanium bulk.

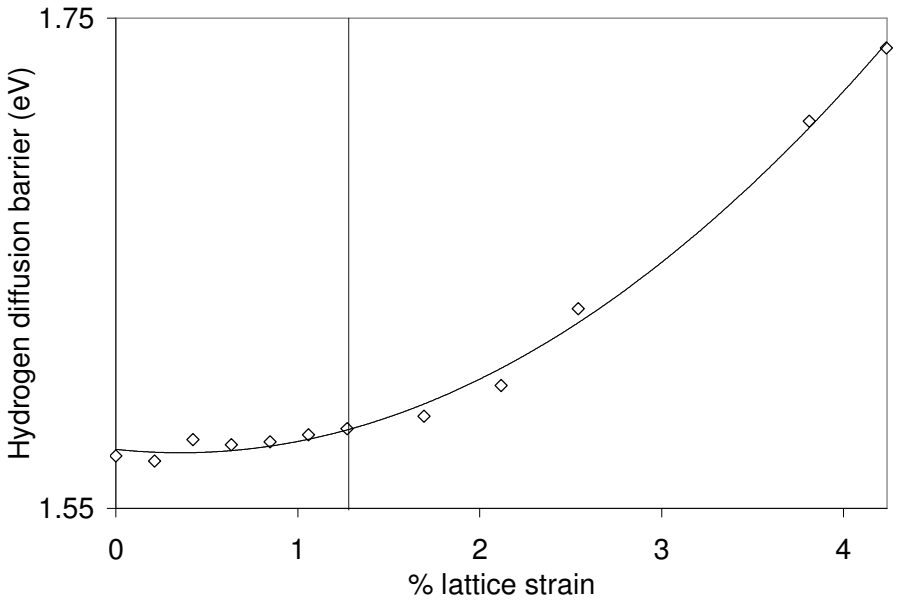

Figure 7.2: Plot of hydrogen diffusion energy barrier versus % of lattice strained applied. Dotted lines joining the data points are trend-lines added to guide the eye. Vertical dotted line denotes the transition point (at ~1.3% lattice strain) for gradual and drastic change in hydrogen diffusion energy barrier.

We can understand the stark difference in the influence of strain on hydrogen surface diffusion below and beyond ~1.3% strain by studying the surface parameters and the relative energetics of the initial adsorption site of the hydrogen before diffusion and the final adsorption site of the hydrogen after diffusion.

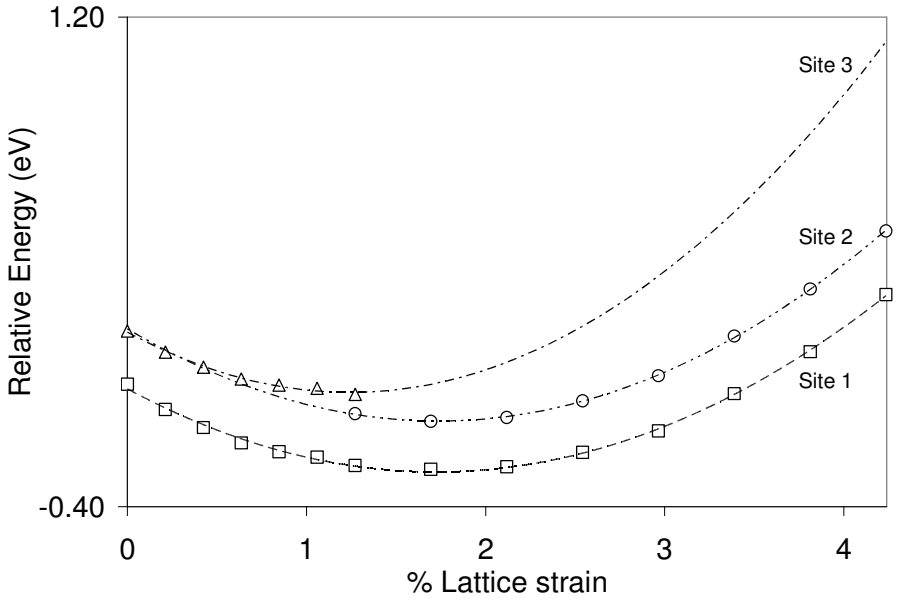

Figure 7.3: Plot of relative energy versus % of lattice strain applied for site 1(□),site 2(O) and site 3(Δ). The sites are defined in Figure 7.4. Dotted lines joining the data points are trend-lines added to guide the eye. Below ~1.3% lattice strain, the higher energy hydrogen can only take on position illustrated by site 3. At ~1.3% lattice strain, hydrogen can take on positions illustrated by either site 2 or site 3 with site 3 at a relatively higher energy. Beyond ~1.3 % lattice strain, position illustrated by site 3 does not exist anymore. This is a point beyond which hydrogen becomes unable to pin the buckling of neighbouring dimers.

Figure 7.3 shows a plot of the relative energies of the initial and final positions of hydrogen over a range of applied lattice strain. As we can see, the relative energy of the two states deviates when a lattice strain of beyond ~1.3% is applied. The higher energy state seems to be able to take on two configurations at the point where the deviation is observed. A closer investigation of the structures revealed that there are indeed two higher energy level adsorption sites for the hydrogen. This is illustrated in figure 7.4.

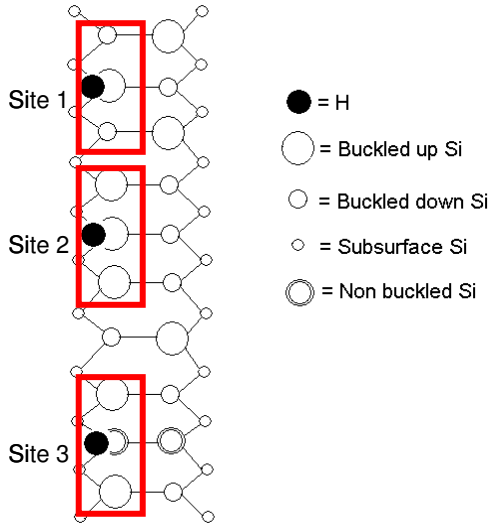

Figure 7.4: An illustration of the different adsorption sites of hydrogen. Corresponding to figure 7.3, site 1 is the lowest energy state while site 2 and 3 is the higher energy state.

Sites 2 and 3 in figure 4 refer to the two high-energy adsorption sites for the hydrogen. From the figure, we can see the action of two competing effects – the effect of inter-dimer interaction along the same row versus the effect of bonding of ad-atoms to dimer. Dimers in the same row like to be alternately buckled. The electronic charges are concentrated around the buckled "up" atom while the buckled down atom is deprived of charges. When an ad-atom tries to form a bond to an atom in the dimer, it would cause the atom to buckle "up" due to a change in hybridization from sp2 to sp3. When a hydrogen atom tries to form a bond to the buckled "up" silicon atom in the dimer, some of the charges on that silicon atom is shifted to the other silicon atom in the same dimer. This results in the reduction in the dimer buckling angle but does not flip the buckling. In this case, there is no conflict in the two effects – the neighboring dimers are still buckled alternately. This is illustrated as the bonding of hydrogen to site 1 as shown in figure 4. When the hydrogen now tries to form a bond to the silicon that is buckled "down", let

this silicon atom be called “A”, some of the electronic charges from the buckled “up” atom, would be transferred to the silicon atom “A” causing it to want to buckle “up”. However, due to the pinning effect of the adjacent dimer, wanting alternate buckling, the dimer becomes unbuckled instead. This gives rise to bonding site 3. However, when strain is applied isotropically to the slab, inter-dimer distance is increased. This increase in inter-dimer distance reduces the buckling-pinning effect of neighboring dimers, hence the configuration shown in site 2 becomes favored.

Up to ~1.3% lattice strain, the increase in the barrier can be considered negligible. This amount of strain at the transition point corresponds to that induced by ~30% germanium content in the silicon substrate (assuming Vergard’s law applies). On the other hand, the variation in the hydrogen surface diffusion barrier corresponding to a maximum of ~4% lattice strain is 0.15 eV. It should also be noted that the overall increase in the diffusion barrier is ~10% corresponding to the 4% increase in strain. It is in about the same order as that noted by Roland and Gilmer [1] about the silicon ad-atom on a tensile strained silicon surface.

When hydrogen diffuse on a germanium-doped silicon surface, the diffusion barrier is affected by both the chemical effect of the germanium present and the lattice strained induced by the germanium. This section attempts to decouple the effects of these two factors have on the hydrogen surface diffusion barrier.

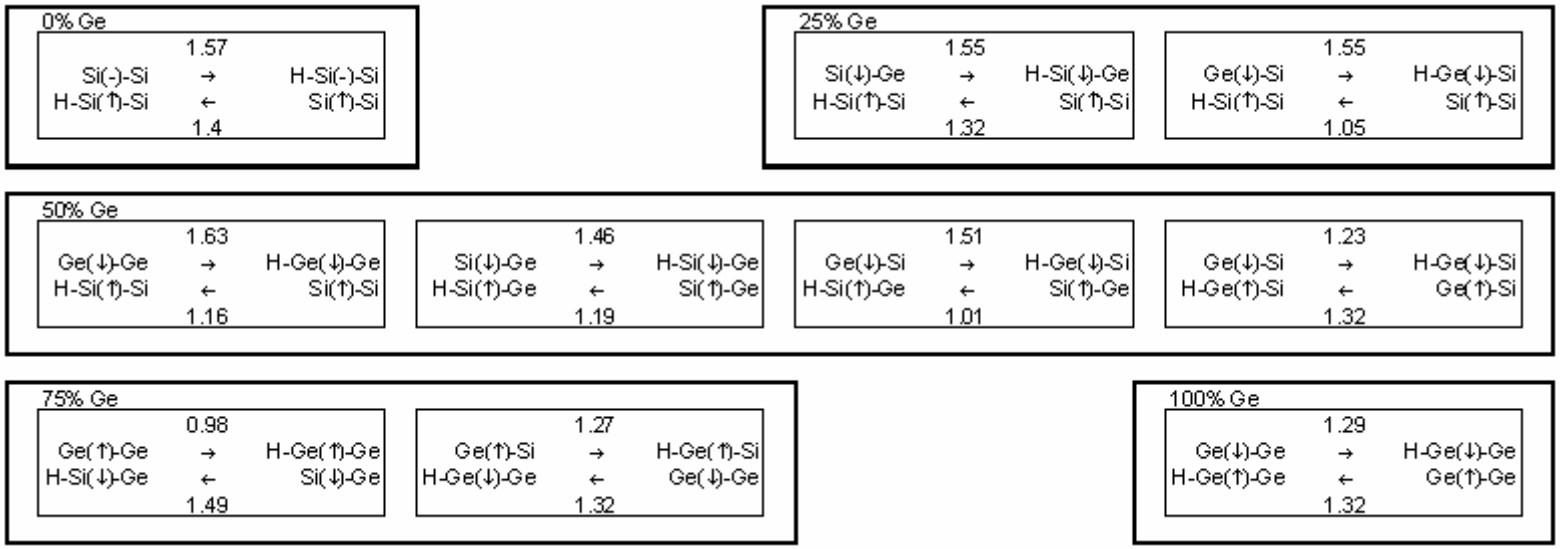

Figure 7.5: An illustration of the energy barrier for hydrogen to surmount for each forward and reversed motion for 2 hydrogen adsorbed sites. x% Ge indicates the amount of germanium incorporated in to the surface of the slab. Arrows "→" and "←" indicate forward motion and backward motion respectively. Energy values indicated above the arrows are the energy barrier for hydrogen to surmount for that particular motion.

Figure 7.5 is an illustration of the energy barrier for hydrogen to surmount for each forward and reversed motion. For example, for the surface with no germanium denoted by "0% Ge", the motion from a buckled up Si to a flat Si dimer requires 1.57eV, while the reverse takes up only 1.4eV. For each value of germanium content, a value of Avg_Max_Ediff is calculated by averaging the greatest value of the diffusion barrier at that germanium content. For instance, at 25% germanium content, the Avg_Max_Ediff is calculated by (1.55 + 1.55)/2 = 1.55. The values of Avg_Max_Ediff for 0%, 25%, 50%, 75%, 100% germanium content is 1.57eV, 1.55 eV, 1.48eV, 1.41eV, 1.32eV respectively. These diffusion barriers values are plotted in figure 7.6 and compared against the effect of strain applied.

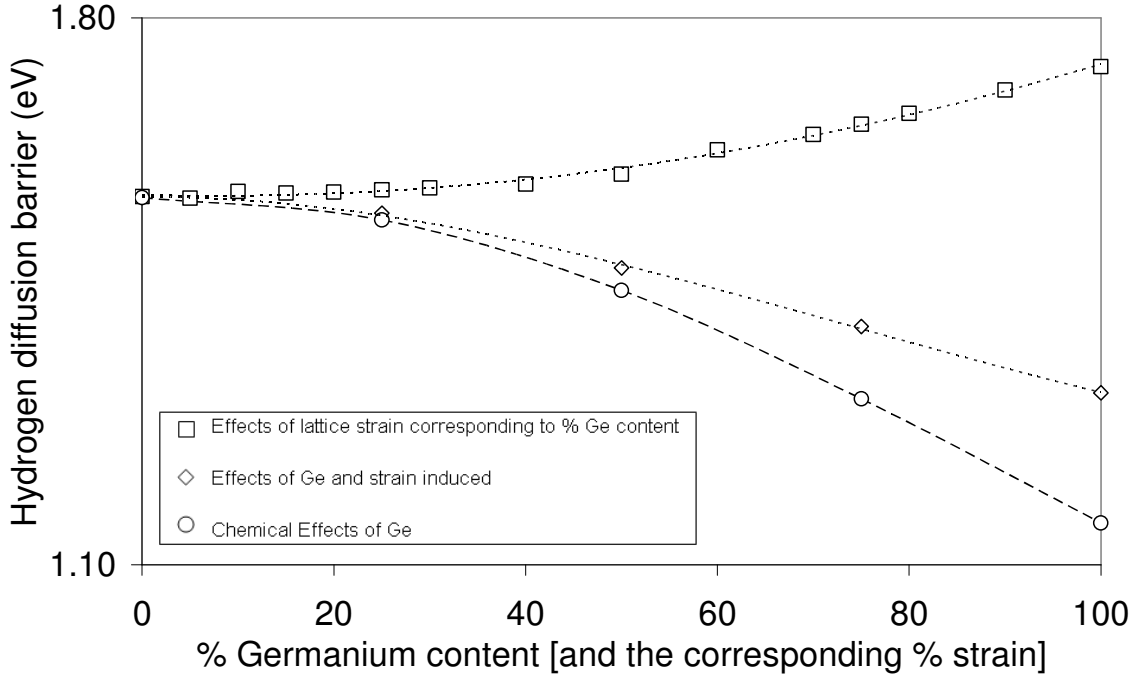

Figure 7.6: Plot of hydrogen diffusion energy barrier versus % germanium content and the corresponding strain induced. Dotted lines joining the data points are trend-lines added to guide the eye. (O) Chemical effects of germanium, (◊) Combined effects of germanium and strain, and (□) Effects of lattice strain corresponding to the % of germanium incorporated are plotted on the same graph.

It can be seen that lattice strain and germanium content affects the diffusion barrier in an opposing trend. Applied lattice strain increases the diffusion barrier of hydrogen while increasing germanium content in the surface reduces the diffusion barrier.

We can think of the germanium having both strain and chemical effects. Thus, by subtracting off the effect of strain, the decoupled chemical effect of Ge is obtained and plotted within the same figure. This plot is obtained by the assumption that the chemical effect of Ge and the effect of strain on H diffusion is a linear summation. Hence, we can see that while strain increases the H diffusion barrier, the chemical effect of Ge reduces the H diffusion barrier to a greater extend such that the combined effect of the two is a net decrease.

These opposing effects can be rationalized. The effect of strain increases the (dimer-to dimer) distance a hydrogen atom has to cross in order to diffuse. Thus, strain has the effect of increasing the barrier for hydrogen diffusion. On the other hand, germanium forms a weaker bond with hydrogen than silicon does, therefore the presence of germanium lowers the barrier for hydrogen to surmount when it comes to moving away from Ge. Thus, on average, the diffusion barrier drops as more Ge is incorporated in the surface.

7.3 Conclusion

In conclusion, we have investigated the surface diffusion kinetics of silylene and hydrogen on strained surface. Our results show while strain has negligible effect on the surface diffusion of silylene, it does increase the barrier for hydrogen to diffuse. For a 4% lattice tensile strain the silylene experienced a 0.02eV difference in the diffusion barrier while the hydrogen diffusion barrier is inceased by 0.15eV. For hydrogen surface diffusion kinetics, our calculations showed that the effects of strain induced by Germanium incorporation can be decoupled from the chemical effects of Germanium atom itself since the change induced is opposite in action.

8 Final Conclusions and Recommendations

8.1 Overview of conclusions

This final chapter of the thesis aims to sum up the main conclusions that have been gathered over the course of this study as well as make recommendations for possible future work.

In essence, we've looked at several surface processes occurring on the surface of pure, strained silicon(100)-2×1 as well as silicon-germanium during the growth of silicon by gas-source-molecular-beam-epitaxy (GSMBE). These surface processes include, the initial decomposition process of the silyl species arising from silane and disilane, where the adsorption energetics and the decomposition kinetics of the silyl species [1], and the surface diffusion process of the decomposition products [*2*] has been studied thoroughly.

From our data, we have attempted to address several puzzles pertaining to the growth of silicon by GSMBE using silane and disilane as precursors. Puzzle number (1): Why is the on-dimer silylene species not observed during STM observation [3, 4] of the surface even when it is energetically more favourable than the intra-row species when they are standing alone? [5-8]. Puzzle number (2): Does the silyl decomposition product have any intrinsic mobility since STM did not observe any correlation in the position of the hydrogen and the silylene species? [4]. Puzzle number (3): How did the intra-row silylene species move on the surface of silicon? And finally puzzle number (4): How did the presence of germanium on the silicon surface affect the surface process during GSMBE?

There are two commonly proposed and accepted adsorption sites for the silylene species that arise from the decomposition of the silyl species – the on-dimer site and the intra-row site, with the on-dimer site being energetically more stable than the intra-row site when they are standing alone on the silicon surface [5-8]. Our calculations have shown that the on-dimer species, besides being able to diffuse faster than an intra-row species (with a diffusion barrier of 0.88eV), it also stands in the way of the only path by which a stand-alone intra-row species could diffuse [2]. However, STM observation of the surface process during GSMBE found no on-dimer species on the surface [3, 4]. We attempt to understand this puzzle from three angles. Firstly, the relative stability of the species in the presence of co-adsorbed hydrogen ad-atom. In agreement with the majority of existing theoretical studies reported in the literatures, the intra-row species is energetically favoured over the on-dimer species by ~0.15eV when they are co-adsorbed with a hydrogen ad-atom. This is indeed the surface condition during growth by GSMBE where hydrogen is present on the surface together with the silylene species. Other than being favoured by adsorption energetics, the intra-row species is also kinetically favoured during silyl decomposition. The decomposition of the silyl species to the intra-row silylene and hydrogen requires ~0.22eV less activation energy than the path that leads to an on-dimer silylene species. Finally, we can understand why the on-dimer species is not observed from surface mobility point of view. After the intra-row silylene species is preferentially formed on the silicon surface during silyl decomposition, it does not move to an on-dimer site because there exists no direct path between the two silylene configurations. The only path that links the two configurations (via an intermediate) is intercepted by a lower energy path that leads to another intra-row silylene species that

straddles on the other two silicon atoms of the same two dimers. Thus from the above discussion, we would be able to understand why the on-dimer species is not observed on the surface.

The STM work studying the surface processes during growth also observed that the silyl decomposition products, particularly the hydrogen ad-atoms and the silylene species, do not have correlated positions [4]. Thus, it has been proposed that these decomposition products may have intrinsic mobility. Our study of the silyl decomposition process revealed that this is likely to be true. From the partition of forces between the decomposition products, it can be observed that the products of the decomposition acquire a considerable amount of frustrated translational energy from the decomposition process. We can safely conclude that the decomposition products are indeed translationally hot and the hydrogen ad-atom is approximately 0.5eV more energetic than the average thermal energy.

For growth to occur, the decomposed species are expected to be able to move from one position to another via a diffusion process. However, we found that the most energetically and kinetically favored intra-row configuration is not able to diffuse along the dimer row to another intra-row site in the absence of co-adsorbed hydrogen. The question of how the intra-row species diffuse on the silicon surface can therefore be understood as a hydrogen-assisted diffusion process. In the presence of a co-adsorbed hydrogen ad-atom, the intra-row species is now able to diffuse, but with a barrier of 1.3eV. This implies that the rate for the intra-row species to diffuse will only becomes appreciable ($k = 1\ s^{-1}$) at temperatures around 500K assuming an attempt frequency of about $10^{13}\ s^{-1}$. It is however interesting to note that the diffusion of the hydrogen and

silylene species could be interdependent processes. In the figure below, dimer rows (i) and (ii) illustrate the relative energy of each structure as adsorption takes place, and the activation energy as diffusion occurs. Dimer row (i) represents the diffusion kinetics and energetics as hydrogen diffuses on a dimer row with an intra-row silylene species co-adsorbed. Dimer row (ii) represents the diffusion kinetics and energetics as an intra-row silylene species diffuses on a dimer row with a hydrogen co-adsorbed.

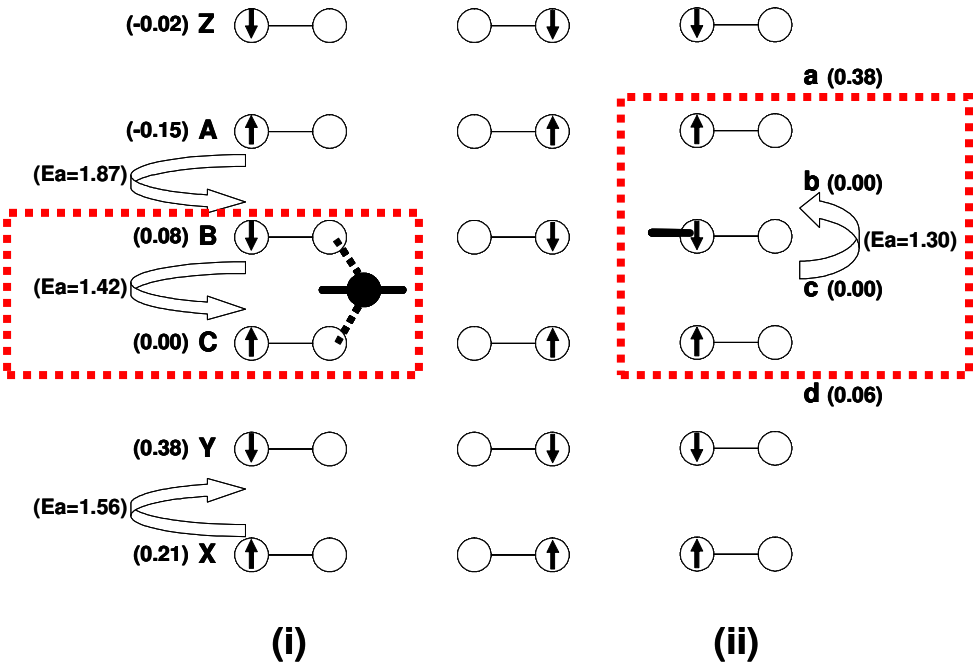

Figure 8.1: An illustration of the diffusion barrier for silylene and hydrogen to move on the silicon (100)-(2×1) surface.

Table 8.1: A summary of the diffusion barrier corresponding to figure 8.1

Diffusing Species	Starting Structure	Ending Structure	Diffusion Activation
H	A	B	1.87
	B	A	1.64
	B	C	1.42
	C	B	1.50
	Y	X	1.39
	X	Y	1.56
SiH_2	B	c	1.30
	C	b	1.30

As we can see, the energetically most stable position for the hydrogen species is “A” while that for the silylene species is “b” and “c”. On the other hand, we can see that on a co-adsorbed surface, the activation energy required for the hydrogen to move in between 2 dimers straddled by the silylene species is much lower than that required for the hydrogen to move away from the siylene. Since the silylene diffusion process is hydrogen assisted, we can propose the following scenario to occur: first, the hydrogen assists the intra-row silylene species to diffuse, e.g. from position b to position c. Then, hydrogen will be encouraged to move from position B to position C. This will go on as a coupled motion due to favorable kinetics.

Finally, our results also help us to understand how the surfaces processes are affected by the presence of germanium and the lattice strain induced on the surface. We have investigated the surface diffusion kinetics of silylene and hydrogen on strained surfaces. Our results show that while strain has a negligible effect on the surface diffusion of silylene, it does increase the barrier for hydrogen to diffuse. For a 4% lattice tensile strain, the silylene experienced a 0.02eV difference in the diffusion barrier while the hydrogen diffusion barrier is increased by 0.15eV. For hydrogen surface diffusion kinetics, our calculations showed that the effects of the strain induced by Germanium incorporation can be decoupled from the chemical effects of Germanium atom itself since the change induced is opposite in sign.

8.2 Recommendations for future work

In view of the intensive study of the surface processes during GSMBE, I have realized the importance for us to understand the interdependence of these processes. Even though, in theoretical point of view, we can study each processes in isolation and hence pin point actual influences of each surface parameters on each process, we must understand that in reality, these processes are happening in conjunction with each other and is highly interdependent. For instance, the diffusion mechanism of surface growth precursors such as the hydrogen ad-atom and the silylene species and the desorption mechanism of hydrogen and the germanium segregation on silicon-germanium substrate. Future work, making use of Monte-Carlo or molecular dynamics simulations can be devoted to achieve an understanding of the interdependence of these individual processes.

Bibliography

Chapter 1

1 G. E. Moore, Electronics 38, 8 (1965)

2 P. Weiss, Science News 165, 136 (2004)

3 M. Bowrey, and J. H. Purnell, *Proceedings of the Royal Society of London. Series A, Mathematical and Physical Sciences*, 321, 341 (1971)

4 J. H. Purnell and R. Walsh, *Proceedings of the Royal Society of London. Series A, Mathematical and Physical Sciences*, 293, 561 (1966)

5 H. C. Abbink, R. M. Broudy and G. P. McCarthy, J. Appl. Phys. 39, 4673 (1968)

6 M. Shimbo, J. Nishizawa and T. Terasaki J. Crystal Growth 23, 267 (1974)

7 T. Sakaurai and H. D. Hagstrum, Phys. Rev. B 12, 5349 (1975)

8 T. Sakaurai and H. D. Hagstrum, Phys. Rev. B 14, 1593 (1976)

9 K. C. Pandey, T. Sakaurai and H. D. Hagstrum, Phys. Rev. Lett. 35, 1728 (1975)

10 J. A. Applebaum, H. D. Hagstrum, D. R. Hamann and T. Sakaurai, Surf. Sci. 58, 479 (1976)

11 Y. J. Chabal, E. E. Chaban, and S. B. Christman, J. Electron Spectrosc. Relat. Phenom. 29, 35 (1983)

12 Y. J. Chabal, Phys. Rev. Lett. 50, 1850 (1983)

13 Y. J. Chabal, G. S. Higashi, and S. B. Christman, Phys. Rev. B 28, 4472 (1983)

14 Y. J. Chabal and K. Raghavachari, Phys. Rev. Lett. 53, 282 (1984)

15 Y. J. Chabal and K. Raghavachari, Phys. Rev. Lett. 54, 1055 (1985)

16 B. von Roedern, L. Ley, and M. Cardona, Phys. Rev. Lett. 39, 1576 (1977)

17 S. M. Gates, C. M Greenlief, S. K Kulkarni and H. H. Sawin J. Vac. Sci. Technol. A 8, 2965 (1989)

18 S. K. Kulkarni, S. M. Gates, B. A. Scott and H. H. Sawin, Surf. Sci. 239, 13 (1990)

19 S. K. Kulkarni, S. M. Gates, C. M. Greenlief and H. H. Sawin, Surf. Sci. 239, 26 (1990)

20 R. W. Price, E. S. Tok, and J. Zhang, Phys. Rev. B 59, R5292 (1998)

21 R. W. Price, E. S. Tok, and J. Zhang, J. Cryst. Growth 209, 306 (1998)

22 M. Shinohara, M. Niwano, Y. Neo and K. Yokoo, Thin Solid Films 369, 16 (2000)

23 M. Shinohara, M. Niwano, Y. Neo and K. Yokoo, Appl. Surf. Sci. 162-163, 111 (2000)

24 M. Shinohara, A. Seyama, Y. Kimura and M. Niwano, Phys. Rev. B 65, 075319 (2002); 075319 (2002)

25 M. Shinohara, Y. Kimura, M. Saito and M. Niwano, Surf. Sci. 502-503, 96 (2002)

26 H. Noda and T. Urisu, Chem. Phys. Lett. 326, 163 (2000)

27 J. R. Engstrom, D. A. Hansen, M. J. Furjanic and L.-Q. Xia, J. Chem. Phys. 99, 4051 (1993)

28 M. E. Jones, L.-Q. Xia, N. Maity and J. R. Engstrom, Chem. Phys. Lett. 229, 401 (1994)

29 L.-Q. Xia, M. E. Jones, N. Maity and J. R. Engstrom, J. Chem. Phys. 103, 1691 (1995)

30 Y.–Y. Mo, J. Kleiner, M. B. Webb and M. G. Lagally, Surf. Sci. 268, 275 (1992)

31 M. J. Brownikowski, Y. Wang, M. T. McEllistrem, D. Chen and R. J. Hamers, Surf. Sci. 298, 50 (1993)

32 Y. Wang, M. J. Bronikowski, R. J. Hamers, Surf. Sci. 311, 64 (1994)

33 M. Fehrenbacher, J. Spitzmuller, M. Pitter, H. Rauscher, and R. J. Behm, Jpn. J. Appl. Phys. 36, 3804 (1997)

34 J. Spitzmuller, M. Fehrenbacher, H. Rauscher, and R. J. Behm, Surf. Sci. 377-379, 1001 (1997)

35 J. Spitzmuller, M. Fehrenbacher, H. Rauscher, and R. J. Behm, Phys. Rev. B 63, 041302 (2001)

36 H. Rauscher, Surf. Sci. Reports 42, 207 (2001)

37 D. R. Bowler and C. M. Goringe, Surf. Sci. 360, L489 (1996)

38 J. H. G. Owen, D. R. Bowler, C. M. Goringe, K. Miki and G. A. D. Briggs, Surf. Sci. 382, L678 (1997)

39 J. H. G. Owen, K. Miki, D. R. Bowler, C. M. Goringe, I. Goldfarb and G. A. D. Briggs, Surf. Sci. 394, 79 (1997)

40 J. H. G. Owen, K. Miki, D. R. Bowler, C. M. Goringe, I. Goldfarb, G. A. D. Briggs, Surf. Sci. 394, 91 (1997)

41 I. Goldfarb, J. H. G. Owen, P. T. Hayden, D. R. Bowler, K. Miki and G. A. D. Briggs, Surf. Sci. 394, 105 (1997)

42 L. Masson and F. Thibaudau, Surf. Sci. 504, 191 (2002)

43 F. Hirose and H. Sakamoto, Appl. Surf. Sci. 135, 293 (1998)

44 F. Hirose and H. Sakamoto, J. Vac. Sci. Technol. B 16, 3364 (1998)

45 P. M. Agrawal, D. L. Thompson and L. M. Raff, Surf. Sci. 195, 283 (1988)

46 P. M. Agrawal, D. L. Thompson and L. M. Raff, J. Chem. Phys. 91, 5021 (1989)

47 G. Brocks and P. J. Kelly, R. Car, Phy. Rev. Lett. 66, 1729 (1990)

48 G. Brocks and P. J. Kelly, R. Car, Surf. Sci. 269/270, 860 (1992)

49 J. Nara, T. Sasaki and T. Ohno, Phys. Rev. Lett. 79, 4421 (1997)

50 S. Jeong and A. Oshiyama, Phys. Rev. Lett. 79, 4425 (1997)

51 S. Jeong and A. Oshiyama, Phys. Rev. B 58, 12958 (1998)

52 J. Spitzmuller, M. Fehrenbacher, M. Pitter, H. Rauscher, and R. J. Behm, Phys. Rev. B 55, 4659 (1997)

53 S. Hong and M. Y. Chou, Phys. Rev. B 58, R13363 (1998)

54 A. R. Brown and D. J. Doren, J. Chem. Phys. 109, 2442 (1998)

55 A. R. Brown and D. J. Doren, J. Chem. Phys. 110, 2643 (1998)

56 D. Srivastava and B. J. Garrison, J. Chem. Phys. 95, 6885 (1991)

57 Z. Zhang and H. Metiu, Surf. Sci. 245, 353 (1991)

58 Y.-T. Lu, Z. Zhang and H. Metiu, Surf. Sci. 257, 199 (1991)

59 S. Ramalingam, P. Mahalingam, E. S. Aydil and D. Maroudas, J. Appl. Phys. 86, 5497(1999)

60 S. Ramalingam, D. Maroudas and E. S. Aydil, J. Appl. Phys. 86, 2872(1999)

61 S. P. Walch, Shyam Ramalingam, Eray S. Aydil and Dimitrios Maroudas, Chem. Phys. Lett. 329, 304 (2000)

62 J. S. Lin and Y. T. Kuo, Thin Solid Films 370, 192 (2000)

63 J. S. Lin, Y. T. Kuo, M.-H. Lee and J. C. Chen, J. of Molecular Structure (Theochem) 496, 163 (2000)

64 J. K. Kang and C. B. Musgrave, Phys. Rev. B 64, 245330 (2001)

65 D. Lubben, R. Tsu, T. R. Bramblett and J. E. Greene, J. Vac. Sci. Technol. A 9, 3003 (1991)

66 C. M Greenlief, S. M. Gates and P. A. Holbert, J. Vac. Sci. Technol. A 7, 1845 (1988)

67 C. M Greenlief, S. M. Gates and P. A. Holbert J. Vac. Sci. Technol. A 7, 1845 (1988)

Chapter 2

1 D. Haneman, Phys. Rev. 121, 1093 (1961)

2 J. C. Phillips, Surf. Sci. 40, 459 (1973)

3 W. A. Harrison, Surf. Sci. 55, 1 (1976)

4 T. D. Poppendieck, T. C. Ngoc and M. B. Webb, Surf. Sci. 75, 287 (1978)

5 R. M. Tromp, R. J. Hamers and J. E. Demuth, Phys. Rev. Lett. 55, 1303 (1985)

6 R. A. Wolkow, Phys. Rev. Lett. 68, 2636 (1992)

7 Z. Zhu, N. Shima and M. Tsukada, Phys. Rev. B 40, 11868 (1989)

8 D. J. Chadi, Phys. Rev. Lett. 43, 43 (1979)

9 M. Rohlfing, P. Krüger, J. Pollmann, Phys. Rev. B 52, 13753 (1995)

10 R. Englman, *The Jahn-Teller Effect in Molecules and Crystals* (Wiley, New York, 1972)

11 P. C. Weakliem, G. W. Smith, and E. A. Carter, Surf. Sci 232, L219 (1990)

12 H. J. W. Zandvliet, B. S. Swartzentruber, W. Wulfhekel, B. J. Hattink, and B. Poelsema, Phys. Rev. B 57, R6803 (1998)

13 L. Pattey, E. L. Bullock, T. Abukawa, S. Kono and L. S. O. Johansson, Phys. Rev. Lett. 75, 2538 (1995)

14 S. J. Jenkins and G. P. Srivastava, J. Phys.: Condens. Matter 8, 6641 (1996)

15 S. J. Jenkins and G. P. Srivastava, Surf. Sci. 377-379, 887 (1997)

16 R. H. Miwa, Surf. Sci. 418, 55 (1998)

17 M. Sasaki, T. Abukawa, H. W. Yeom, M. Yamada, S. Suzuki, S. Sato, S. Kono, Appl. Surf. Sci. 82-83, 387 (1994)

18 Y.-W. Mo, D. E. Savage, B. S. Swartzentruber, and M. G. Lagally, Phys. Rev. Lett. 65, 1020 (1990)

19 E. Rudkevich, Feng Liu, D. E. Savage, T. F. Kuech, L. McCaughan, and M. G. Lagally, Phys. Rev. Lett. 81, 3467 (1998)

20 S. Jeong and A. Oshiyama, Surf. Sci. 436, L666 (1999)

21 S. S. Iyer, J. C. Tsang, M. W. Copel, P. R. Pukite, and R. M. Tromp, Appl. Phys. Lett. 54, 219 (1988)

22 M. Copel and R. M. Tromp, Appl. Phys. Lett. 58, 2648 (1991)

23 D. A. Grützmacher, T. O. Sedgwick, A. Powell, M. Tejwani, S. S. Iyer, J. Cotte, and F. Cardone, Appl. Phys. Lett. 63, 2531 (1993)

24 D. E. Jesson, S. J. Pennycook and J.-M. Baribeau, Phys. Rev. Lett. 66, 750 (1991)

25 J. Nara, T. Sasaki, and T. Ohno, Phys. Rev. Lett. 79, 4421 (1997)

26 R. Butz and S. Kampers, Thin Solid Films 222, 104 (1992)

27 S. Zaima, K. Sato, T. Kitani, T. Matsuyama, H. Ikeda and Y. Yasuda, J. Cryst. Growth 150, 944 (1994)

28 K. Nakagawa, A. Nishida, Y. Kimura and T. Shimada, J. Cryst. Growth 150, 939 (1994)

29 P. Krüger and J. Pollmann, Phys. Rev. Lett. 72, 1130 (1994)

30 J.-H. Cho and M-. H. Kang, Phys. Rev. B 49, 13670 (1994)

31 J.-H. Cho, S. Jeong, and M.-H. Kang, Phys. Rev. B 50, 17139 (1994)

32 S. C. A. Gay and G. P. Srivastava, Phys. Rev. B 60, 1488 (1999)

33 S. Tang and A. J. Freeman, Phys. Rev. B 50, 10941 (1994)

34 H. Oyanagi, K. Sakamoto, R. Shioda, and Y. Kuwahara, Phys. Rev. B. 52, 5824 (1995)

35 E. Fontes, J. R. Patel and F. Comin, Phys. Rev. Lett. 70, 2790 (1993)

36 Z.-Y. Lu, F. Liu, C.-Z. Wang, X. R. Qin, B. S. Swartzentruber, M. G. Lagally, and K.-M. Ho, Phys. Rev. Lett. 85, 5603 (2000)

37 X. Chen, D. K. Saldin, E. L. Bullock, L. Patthey, L. S. O. Johansson, J. Tani, T. Abukawa, and S. Kono, Phys. Rev. B 55, R7319 (1997)

38 J. D[illegible]browski and M. Scheffler, Appl. Surf. Sci. 56-58, 15 (1992)

39 E. S. Tok, S. W. Ong and H. C. Kang, J. Chem. Phys. 120, 5424 (2004)

40 Z.-Y. Lu, C. Z. Wang and K. M. Ho, Surf. Sci. 506, L282 (2002)

41 R. J. Hamers and Y. Wang, Chem. Rev. 96, 1261 (1996)

42 S. Jeong and A. Oshiyama, Phys. Rev. Lett. 79, 4425 (1997)

43 S. Jeong and A. Oshiyama, Phys. Rev. B 58, 12958 (1998)

44 P. Zhou, J. Cheng, S. Z. Sun, C. F. Schaus, C. Hains, D. R. Myers, and G. A. Vawter, Appl. Phys. Lett. 59, 2648 (1991)

45 G. Ohta, S. Fukatsu, Y. Ebuchi, T. Hattori, N. Usami, and Y. Shiraki, Appl. Phys. Lett. 65, 2975 (1994)

46 S. Zaima and Y. Yasuda, J Cryst. Growth 163, 105 (1996)

47 H. Kim, N. Taylor, J. R. Abelson, and J. E. Greene, J. Appl. Phys. 82, 6062 (1997)

48 M. L. Wise, B. G. Koehler, P. Gupta, P. A. Coon and S. M. George, Surf. Sci. 258, 166 (1991)

49 U. Höfer, L. Li, and T. F. Heinz, Phys. Rev. B 45, 9485 (1992)

50 K. Sinniah, M. G. Sherman, L. B. Lewis, W. H. Weinberg, J. T. Yates, Jr., and K. C. Janda., J. Chem. Phys. 92, 5700 (1990)

51 K. Sinniah, M. G. Sherman, B. Lisa, W. H. Weinberg, J. T. Yates, Jr., and K. C. Janda, Phys. Rev. Lett. 62, 567 (1990)

52 M. P. D'Evelyn, Y. L. Yang and L. F. Sutcu, J. Chem. Phys. 96, 852 (1992)

53 H. Nakazawa, M. Suemitsu, and N. Miyamoto, Surf. Sci. 465, 177 (2000)

54 E. S. Tok and H. C. Kang, J. Chem. Phys. 115, 6550 (2001)

55 J. J. Boland, Phys. Rev. Lett. 67, 1539 (1991)

56 J. J. Boland, J. Vac. Sci. Technol. A 10, 2458 (1992)

57 S. M. Gates, R. R. Kunz, and C. M. Greenlief, Surf. Sci. 207, 364 (1989)

58 C. M. Greenlief, S. M. Gates, and P. A. Holbert, J. Vac. Sci. Technol. A 7, 1845 (1989)

59 C. C. Cheng and J. T. Yates, Jr., Phys. Rev. B 43, 4041 (1991)

60 T. Angot and P. Louis, Phys. Rev. B 60, 5938 (1999)

61 M. C. Flowers, N. B. H. Jonathan, Y. Liu and A. Morris, J. Chem. Phys. 99, 7038 (1993)

62 M. P. D'Evelyn, S. M. Cohen, E. Rouchouze, and Y. L. Yang, J. Chem. Phys. 98, 3560 (1993)

63 D-. S. Lin and R-. P. Chen, Phys. Rev. B 60, R8461 (1999)

64 L. B. Lewis, J. Segall, and K. C. Janda, J. Chem. Phys. 102 , 7222 (1995)

65 J. Y. Lee, J. Y. Maeng, A. Kim, Y. E. Cho, and S. Kim, J. Chem. Phys. 118, 1929 (2003)

66 J. M. Fernández, L. Hart, X. M. Zhang, M. H. Xie, J. Zhang and B. A. Joyce, J. Cryst. Growth 164, 241 (1996)

67 B. S. Meyerson, K. J. Uram, and F. K. LeGoues, Appl. Phys. Lett. 53, 2555 (1988)

68 B. M. H. Ning and J. E. Crowell, Appl. Phys. Lett 60, 2914 (1992)

69 T. Angot and R. Chelly, Surf. Sci. 402-404, 52 (1998)

70 S. M. Gates, C. M. Greenlief, and D. B. Beach, J. Chem. Phys. 93, 7493 (1990)

71 M. A. Mendicino and E. G. Seebauer, J. Electrochem. Soc. 140, 1786 (1993)

72 S. M. Gates, C. M. Greenlief, D. B. Beach, and P. A. Holbert, J. Chem. Phys. 92, 3144 (1990)

73 S. M. Gates, C. M. Greenlief, S. K. Kulkarni, and H. H. Sawin, J. Vac. Sci. Technol. A 8, 2965 (1990)

74 S. M. Gates and S. K. Kulkarni, Appl. Phys. Lett. 58, 2963 (1991)

75 S. M. Gates and S. K. Kulkarni, Appl. Phys. Lett. 60, 53 (1992)

76 S. M. Gates, J. Cryst. Growth 120, 269 (1992)

77 V. N. Kruchinin, S. M. Repinsky, and A. A. Shklyaev, Surf. Sci. 275, 433 (1992)

78 M. E. Jones, L.-Q. Xia, N. Maity, and J. R. Engstrom, Chem. Phys. Lett. 229, 401 (1994)

79 L.-Q. Xia, M. E. Jones, N. Maity, and J. R. Engstrom, J. Vac. Sci. Technol. A 13, 2651 (1995)

80 S. M. Gates, C. M. Greenlief, D. B. Beach and P. A. Holbert, J. Chem. Physics 92, 3144 (1990)

81 S. M. Gates, and C. M. Chiang, Chem. Phys. Lett. 184, 448 (1991)

82 A. Robinson Brown, and D. J. Doren, J. Chem. Phys. 110, 2643 (1999)

83 F. Hirose, M. Suemitsu, and N. Miyamoto, Appl. Surf. Sci. 60/61, 592 (1992)

84 F. Hirose, M. Suemitsu, and N. Miyamoto, J. Appl. Phys. 70, 5380 (1991)

85 M. Suemitsu, K.-J. Kim, H. Nakazawa, and N. Miyamoto, Appl. Surf. Sci. 107, 81 (1996)

86 K.-J. Kim, M. Suemitsu, M. Yamanaka, and N. Miyamoto, Appl. Phys. Lett. 62, 3461 (1993)

87 H. Nakazawa, M. Suemitsu and N. Miyamoto, Jpn. J. Appl. Phys. 36, L703 (1997)

88 J. R. Engstrom, L.-Q. Xia, M. J. Furjanic, and D. A. Hansen, Appl. Phys. Lett. 63, 1821 (1993)

89 N. Maity, L.-Q. Xia, and J. R. Engstrom, Appl. Phys. Lett. 66, 1909 (1995)

90 J. R. Engstrom, D. A. Hansen, M. J. Furjanic, and L.-Q. Xia J. Chem. Phys. 99, 4051 (1993)

91 L.-Q. Xia and J. R. Engstrom, J. Chem. Phys. 101, 5329 (1994)

92 L.-Q. Xia, M. E. Jones, N. Maity, and J. R. Engstrom, J. Chem. Phys. 103, 1691 (1995)

93 F. Bozso and Ph. Avouris, Phys. Rev. B 38, 3943 (1988)

94 D.–S. Lin, T. Miller, T.–C. Chiang, R. Tsu and J. E. Greene, Phys. Rev. B 48, 11846 (1993)

95 A. C. Dillon, M. B. Robinson and S. M. George, Surf. Sci. 295, L998 (1993)

96 Y. Wang, M. J. Bronikowski and R. J. Hamers, Surf. Sci. 311, 64 (1994)

97 M. J. Bronikowski, Y. Wang, M. T. McEllistrem, D. Chen, and R. J. Hamers, Surf. Sci 298, 50 (1993)

98 Y. M. Wu, J. Baker, P. Hamilton and R. M. Nix, Surf. Sci. 295, 133 (1993)

99 J. J. Boland, Phys. Rev. B 44, 1383 (1991)

100 Y. Suda, D. Lubben, T. Motooka, and J. E. Greene, J. Vac. Sci. Technol. B 7, 1171 (1989)

101 Y. Suda, D. Lubben, T. Motooka, and J. E. Greene, J. Vac. Sci. Technol. A 8, 61 (1990)

102 D. Lubben, R. Tsu, T. R. Bramblett, and J. E. Greene, J. Vac. Sci. Technol. A 9, 3003 (1991)

103 Y. Ohshita, F. Uesugi and I. Nishiyama, J. Cryst. Growth 115, 551 (1991)

104 S. Butzke , K. Werner , J. Trommel , S. Radelaar and P. Balk, Thin Solid Film 228, 27 (1993)

105 W. L. M. Weerts, M. H. J. M. de Croon, and G. B. Marin, Surf. Sci. 367, 321 (1996)

106 J. M. Jasinski and S. M. Gates, Acc. Chem. Res. 24, 9 (1991)

107 Y. M. Wu and R. M. Nix, Surf. Sci. 306, 59 (1994)

108 M. Shinohara, Y. Kimura, M. Saito and M. Niwano, Surf. Sci. 502-503, 96 (2002)

109 D. R. Bowler and C. M. Goringe, Surf. Sci. 360, L489 (1996)

110 S. Hong and M. Y. Chou, Phys. Rev. B 58, 13363 (1998)

111 N. Takeuchi, Surf. Sci. 529, 274 (2003)

112 J. Spitzmüller, M. Fehrenbacher, M. Pitter, H. Rauscher, and R. J. Behm, Phys. Rev. B 55, 4659 (1997)

113 S. M. Gates, C. M. Greenlief, and D. B. Beach, J. Chem. Phys. 93, 7439 (1990)

114 K. W. Kolasinski, S. F. Shane, and R. N. Zare J. Chem. Phys. 95, 5482 (1991)

115 K. W. Kolasinski, S. F. Shane, and R. N. Zare, J. Chem. Phys. 96, 3995 (1992)

116 S. F. Shane, K. W. Kolasinski, and R. N. Zare, J. Chem Phys. 97, 1520 (1992)

117 S. F. Shane, K. W. Kolasinski, and R. N. Zare, J. Chem. Phys. 97, 3704 (1992)

118 H. Noda, and T. Urisu, Chem. Phys. Lett. 326, 163 (2000)

119 P. Nachtigall, K. D. Jordan, and C. Sosa, J. Chem. Phys. 101, 8073 (1994)

120 D.–S. Lin, E. S. Hirschorn, and T.–C. Chiang, R. Tsu, D. Lubben, and J. E. Greene, Phys. Rev. B 45, 3494 (1992)

121 J. H. G. Owen, K. Miki, D. R. Bowler, C. M. Goringe, I. Goldfarb and G. A. D. Briggs, Surf. Sci. 394, 79 (1997)

122 J. Spitzmuller, M. Fehrenbacher, H. Rauscher, and R. J. Behm, Phys. Rev. B 63, 041302 (2001)

123 D. R. Bowler, Wolfson College, A theoretical investigation of gas source growth of the Si(001) surface, D. Phil Thesis, Trinity 1997

124 Y.-W. Mo, J. Kleiner, M. B. Webb and M. G. Lagally, Surf. Sci. 268, 275 (1992)

125 J. E. Vasek, Z. Zhang, C. T. Salling, and M. G. Lagally, Phys. Rev. B 51, 17207 (1995)

126 Q.-M. Zhang, C. Roland, P. Boguslawski, and J. Bernholc, Phys. Rev. Lett. 75, 101 (1995)

127 G. Brocks, P. J. Kelly and R. Car, Surf. Sci. 269/270, 860 (1992)

128 D. Srivastava and B. J. Garrison, J. Chem. Phys. 95, 6885 (1991)

129 Y.-T. Lu, Z. Zhang and H. Metiu, Surf. Sci. 257, 199 (1991)

130 G. Brocks, P. J. Kelly and R. Car, Phys. Rev. Lett. 66, 1729 (1991)

131 M. Copel and R. M. Tromp, Phys. Rev. Lett. 71, 1236 (1994)

132 C. Roland and G. H. Gilmer, Phys. Rev. B 46, 134281 (1992)

133 H. Spjut and D. A. Faux, Surf. Sci. 306, 233 (1994)

134 H. Brune, K. Bromann, H. Röder, K. Kern, J. Jacobsen, P. Stoltze, K. Jacobsen and J. No/rskov, Phys. Rev. B 52, R14380 (1995)

135 M. Schroeder and D. E. Wolf, Surf. Sci. 375, 129 (1997)

136 T. Hoshino, M. Hata and M. Tsuda, Surf. Sci. 481, 205 (2001)

137 A. van de. Walle, M. Asta and P. W. Voorhees, Phys. Rev. B 67, 041308 (R) (2003)

138 E. Zoethout, O. Gürlü, H. J. W. Zandvliet and B. Poelsema, Surf. Sci. 452, 247 (2000)

Chapter 3

1 P. Hohenberg and W. Kohn, Phys. Rev.136, B864 (1964)

2 W. Kohn and L. J. Sham, Phys. Rev 140, A1133 (1965)

3 R. G. Parr and W. Yang, *Density-Functional Theory of Atoms and Molecules*, Oxford University Press (1989)

4 D. M. Ceperley and, B. J. Alder, Phys. Rev. Lett., 45 466 (1980)

5 A. D. Becke, Phys. Rev. A 38, 3098 (1988)

6 J. P. Perdew, Phys. Rev. B 33, 8822 (1986)

7 A. D. Becke, J. Chem. Phys. 84, 4524 (1986)

8 D. J. Lacks, R. G. Gordon, Phys. Rev. A 47, 4681 (1993)

9 J. P. Perdew, K. Burke, M. Ernzerhof, Phys. Rev. Lett., 77, 3865 (1996), Erratum: Phys. Rev. Lett., 78, 1396 (1997)

10 C. Lee, W. Yang, R. G. Parr, Phys. Rev. B 37, 785 (1988)

11 J. P. Perdew, in Electronic Structure of Solids '91, edited by P. Ziesche and H. Eschrig (Akademie Verlag, Berlin, 1991), p11

12 J. P. Perdew, J. A. Chevary, S. H. Vosko, K. A. Jackson, M. R. Pederson, D. J. Singh, and C. Fiolhais, Phys. Rev. B. 46, 6671 (1992)

13 J. P. Perdew, J. A. Chevary, S. H. Vosko, K. A. Jackson, M. R. Pederson, D. J. Singh, and C. Fiolhais, Phys. Rev. B. 48, 4978E (1993)

14 A. D. Becke, J. Chem. Phys. 96, 2155 (1992)

15 E. I. Proynov, E. Ruiz, A. Vela, and D. R. Salahub, Int. J. Quantum Chem. S29, 61 (1995)

16 B. Hammer, K. W. Jacobsen, and J. K. Nørskov, Phys. Rev. Lett. 70, 3971 (1993)

17 B. Hammer and M. Scheffler, Phys. Rev. Lett. 74, 3487 (1995)

18 D. R. Hamann, Phys. Rev. Lett. 76, 660 (1996)

19 P. H. T. Philipsen, G. te Velde, and E. J. Baerends, Chem. Phys. Lett. 226, 583 (1994)

20 M. Levy, Int. J. Quantum Chem. S23, 617 (1989)

Chapter 4

1 M. C. Payne and J. Joannopoulous, Rev. Mod. Phys. 64, 1045 (1992)

2 J. P. Perdew, K. Burke and M. Ernzehof, Phys. Rev. Lett. 77, 3865 (1996)

3 D. M. Bylander and L. Kleinman, Phys. Rev. B 41, 907 (1990)

4 G. B. Ramstad and P. J. Kelly, Phys. Rev. B 51, 14504 (1995)

Chapter 5

1 K. Werner, S. Butzke, S. Radelaar and P. Balk, J. Cryst. Growth 136, 322 (1994)

2 D. R. Bowler and C. M. Goringe, Surf. Sci. 360, L489 (1996)

3 S. Hong and M.Y. Chou, Phys. Rev. B 58, R13363 (1998)

4 M. Çakmak and G.P. Srivastava, Phys. Rev. B 61, 10216 (2000)

5 N. Takeuchi, Surf. Sci. 529, 274 (2003)

6 Y. Wang, M.J. Bronikowski, R.J. Hamers, Surf. Sci. 311, 64 (1994)

7 M. J. Bronikowski, Y. Wang, M. T. McEllistrem, D. Chen and R. J. Hamers, Surf. Sci. 298, 50 (1993)

8 S. M. Gates, C. M. Greenlief, D. B. Beach, and P. A. Holbert, J. Chem. Phys. 92, 3144 (1990)

9 S. M. Gates, C. M. Greenlief, and D. B. Beach, J. Chem. Phys. 93, 7493 (1990)

10 S. M. Gates and C. M. Greenlief, S. K. Kulkarni and H. H. Sawin, J. Vac. Sci. Tech. A 8, 2965 (1990)

11 C. M. Greenlief, S. M. Gates and P. A. Holbert, J. Vac. Sci. Tech. A 7, 1845 (1989)

12 S. M. Gates, Surf. Sci. 195, 307 (1988)

13 F. Bozso and Ph. Avouris, Phys. Rev. B 38, 3943 (1988)

14 R. Imbihl, J. E. Demuth, S. M. Gates, and B. A. Scott, Phys. Rev. B 39, 5222 (1989)

15 S. K. Kulkarni, S. M. Gates, B. A. Scott and H. H. Sawin, Surf. Sci. 239, 13 (1990)

16 S. K. Kulkarni, S. M. Gates, C. M. Greenlief and H. H. Sawin, Surf. Sci. 239, 26 (1990)

17 R. J. Hamers and Y. Wang, Chem. Rev. 96, 1261 (1996)

18 Y. Tsukidate and M. Suemitsu, Jpn. J. Appl. Phys. 40, 5206 (2001)

19 J. H. G. Owen, K. Miki, D. R. Bowler, C. M. Goringe, I. Goldfarb, G. A. D. Briggs, Surf. Sci. 394, 79 (1997)

20 X. L. Zhou and J. M. White, Appl. Surf. Sci. 35, 52 (1988)

21 K. M. Ogle, J. R. Creighton, S. Akhter, and J. M. White, Surf. Sci. 169, 246 (1986)

22 J. K. Kang and C. B. Musgrave, Phys. Rev. B 64, 245330 (2001)

23 R. D. Smardon and G. P. Srivastava, J. Chem. Phys. 123, 174703 (2005)

24 M. C. Payne and J. Joannopoulous, Rev. Mod. Phys. 64, 1045 (1992)

25 J. P. Perdew, K. Burke and M. Ernzerhof, Phys. Rev. Lett. 77, 3865 (1996)

26 D. M. Bylander, L. Kleinman, Phys. Rev. B 41, 907 (1990)

Chapter 6

1 G. E. Moore, Electronics 38, 8 (1965)

2 S. M. Gates, C. M. Greenlief, and D. B. Beach, J. Chem. Phys. 93, 7493 (1990)

3 S. M. Gates and S. K. Kulkarni, Appl. Phys. Lett. 58, 2963 (1991)

4 S. M. Gates, J. of Crystal Growth 120, 269 (1992)

5 D.-S. Lin, E. S. Hirschorn, T.-C. Chiang, R. Tsu, D. Lubben, and J. E. Greene, Phys. Rev. B 45, 3494 (1992)

6 Y.-W. Mo, J. Kleiner, M. B. Webb and M. G. Lagally, Surf. Sci. 268, 275 (1992)

7 F. Bozso and Ph. Avouris, Phys. Rev. B 38, 3943 (1988)

8 S. M. Gates and C. M. Chiang, Chem. Phys. Lett. 184, 448 (1991)

9 A. C. Dillon, M. B. Robinson and S. M. George, Surf. Sci. 295, L998 (1993)

10 Y. Wang, M. J. Bronikowski, R. J. Hamers, Surf. Sci. 311, 64 (1994)

11 M. J. Bronikowski, Y. Wang, M. T. McEllistrem, D. Chen, and R. J. Hamers, Surf. Sci. 298, 50 (1993)

12 D.-S. Lin, T. Miller, T.-C. Chiang, R. Tsu, J. E. Green, Phys. Rev. B 48, 11846 (1993)

13 Y. M. Wu, J. Baker, P. Hamilton and R. M. Nix, Surf. Sci. 295, 133 (1993)

14 J. J. Boland, Phys. Rev. B 44, 1383 (1991)

15 Y. Suda, D. Lubben, T. Motooka, and J. E. Greene, J. Vac. Sci. Technol. B 7, 1171 (1989)

16 Y. Suda, D. Lubben, T. Motooka, and J. E. Greene, J. Vac. Sci. Technol. A 8, 61 (1990)

17 S. M. Gates, C. M. Greenlief, D. B. Beach and P. A. Holbert, J. Chem. Phys. 92, 3144 (1990)

18 S. M. Gates, C. M. Greenlief, S. K. Kulkarni and H. H. Sawin, J. Vac. Sci. Technol. A 8, 2965 (1990)

19 J. H. G. Owen, K. Miki, D. R. Bowler, C. M. Goringe, I. Goldfarb and G. A. D. Briggs Surf. Sci. 394, 79 (1997)

20 M. Fehrenbacher, J. Spitzmuller, M. Pitter, H. Rauscher, and R. J. Behm, Jpn. J. Appl. Phys. 36, 3804 (1997)

21 J. Spitzmuller, M. Fehrenbacher, H. Rauscher, and R. J. Behm, Phys. Rev. B 63 041302 (2001)

22 D. R. Bowler, Wolfson College, D. Phil Thesis, Trinity 1997, A theoretical investigation of gas source growth of the Si(001) surface

23 J. E. Vasek, Z. Zhang, C. T. Salling, and M. G. Lagally, Phys. Rev. B 51, 17207 (1995)

24 S. Jeong and A. Oshiyama, Phys. Rev. B 58, 12958 (1998)

25 S. Jeong and A. Oshiyama, Phys. Rev. Lett. 79, 4425 (1997)

26 J. Nara, T. Sasaki, and T. Ohno, Phys. Rev. Lett. 79, 4421 (1997)

27 Q.-M. Zhang, C. Roland, P. Boguslawski, and J. Bernholc, Phys. Rev. Lett. 75, 101 (1995)

28 G. Brocks, P. J. Kelly and R. Car, Surface Science 269/270, 860 (1992)

29 D. Srivastava and B. J. Garrison, J. Chem. Phys. 95, 6885 (1991)

30 Yan-Ten Lu, Zhenyu Zhang and Horia Metiu, Surf. Sci. 257, 199 (1991)

31 G. Brocks, P. J. Kelly and R. Car, Phys. Rev. Lett. 66, 1729 (1991)

32 M. Copel and R. M. Tromp, Phys. Rev. Lett. 71, 1236 (1994)

33 M. C. Payne and J. Joannopoulous, Rev. Mod. Phys. 64, 1045 (1992)

34 J. P. Perdew, K. Burke and M. Ernzehof, Phys. Rev. Lett. 77, 3865 (1996)

35 D. M. Bylander, L. Kleinman, Phys. Rev. B 41, 907 (1990)

36 D. Chen and J. J. Boland, Phys. Rev. B 65, 165336 (2002)

37 R. J. Hamers, U. K. Köhler and J. E. Demuth, J. Vac. Sci. Technol. A 8, 195 (1990)

Chapter 7

1. C. Roland and George H. Gilmer, Phys. Rev. B 46, 134281(1992)

2. H. Spjut and D. A. Faux, Surf. Sci. 306, 233 (1994)

3. H. Brune, K. Bromann, H. Röder, K. Kern, J. Jacobsen, P. Stoltze, K. Jacobsen and J. No/rskov, Phys. Rev. B 52, R14380 (1995)

4. M. Schroeder and D. E. Wolf, Surf. Sci. 375, 129 (1997)

5. T. Hoshino, M. Hata and M. Tsuda, Surf. Sci. 481, 205 (2001)

6. A. van de. Walle, M. Asta and P. W. Voorhees, Phys. Rev. B 67, 041308 (R) (2003)

7. E. Zoethout, O. Gürlü, H. J. W. Zandvliet and B. Poelsema, Surf. Sci. 452, 247 (2000)

8. M. C. Payne and J. Joannopoulous, Rev. Mod. Phys. 64, 1045 (1992)

9. J. P. Perdew, K. Burke and M. Ernzerhof, Phys. Rev. Lett. 77, 3865 (1996)

10. D. M. Bylander, L. Kleinman, Phys. Rev. B 41, 907 (1990)

Chapter 8

1. F. C. H. Lim, E. S. Tok and H. C. Kang, Phys. Rev. B 74, 205333 (2006)

2. F. C. H. Lim, E. S. Tok and H. C. Kang, to be submitted (Surface diffusion of a silylene species on silicon (100))

3. Y. Wang, M. J. Bronikowski, R. J. Hamers, Surf. Sci. 311, 64 (1994)

4. M. J. Bronikowski, Y. Wang, M. T. McEllistrem, D. Chen and R. J. Hamers, Surf. Sci. 298, 50 (1993)

5. G. D. Bowler and C. M. Goringe, Surf. Sci. 360, L489 (1996)

6. S. Hong and M. Y. Chou, Phys. Rev. B 58, R13363 (1998)

7. M. Çakmak and G. P. Srivastava, Phys. Rev. B 61, 10216 (2000)

8. N. Takeuchi, Surf. Sci. 529, 274 (2003)